

Electronic Theses and Dissertations, 2004-2019

2010

Application Of Antenna Synthesis And Digital Signal Processing Techniques For Active Millimeter-wave Imaging Systems

Wilson Ariel Caba
University of Central Florida

 Part of the [Electromagnetics and Photonics Commons](#), and the [Optics Commons](#)
Find similar works at: <https://stars.library.ucf.edu/etd>
University of Central Florida Libraries <http://library.ucf.edu>

This Doctoral Dissertation (Open Access) is brought to you for free and open access by STARS. It has been accepted for inclusion in Electronic Theses and Dissertations, 2004-2019 by an authorized administrator of STARS. For more information, please contact STARS@ucf.edu.

STARS Citation

Caba, Wilson Ariel, "Application Of Antenna Synthesis And Digital Signal Processing Techniques For Active Millimeter-wave Imaging Systems" (2010). *Electronic Theses and Dissertations, 2004-2019*. 1600.
<https://stars.library.ucf.edu/etd/1600>

APPLICATION OF ANTENNA SYNTHESIS AND DIGITAL SIGNAL PROCESSING
TECHNIQUES FOR ACTIVE MILLIMETER-WAVE IMAGING SYSTEMS

by
WILSON ARIEL CABA
B.S. Pontificia Universidad Católica Madre y Maestra, 2002
M.S. University of Central Florida, 2008

A dissertation submitted in partial fulfillment of the requirements
for the degree of Doctor of Philosophy
in the College of Optics and Photonics: CREOL & FPCE
at the University of Central Florida
Orlando, Florida

Fall 2010

Major Professor: Glenn Boreman

© 2010 Wilson A. Caba

ABSTRACT

Millimeter-wave imaging has gathered attention in recent years for its ability to penetrate clothing, thin layers of soils, and certain construction materials. However, image quality remains a challenge that needs to be addressed. One way of improving image quality is by increasing the dimensions of the collecting aperture. A sparse array can be used to synthesize a larger aperture with a limited set of relatively small detectors.

In this research we design, build, and test a test-bed having an active source at 94 GHz and an array of coherent detectors, mounted on arms that extend radially on a rotary table. Using this test bed a circular area with a maximum diameter of 900 mm can be scanned. The signal is down-converted using heterodyne receivers with digital in-phase and quadrature detection. Signal correlation is performed using the digitized data, which is stored for post-processing, electronic focusing, and image reconstruction.

Near-field imaging using interferometric reconstructions is achieved using electronic focusing. Imaging tests show the ability of the system to generate imagery of concealed and unconcealed objects at distances between 400 and 700 mm. A study of the effects of redundant and non-redundant configurations on image quality for 4 common detector configurations is presented. In this document we show that an active sparse-aperture imaging system using digital correlators is a viable way to generate millimeter-wave images.

To those whose love and support have shown me what the important things in life are.

ACKNOWLEDGMENTS

This work would not have been completed without the help and support of many people, and I would like to thank:

Dr. Glenn Boreman, for his patience, guidance and support throughout the time of my graduate studies at UCF. His knowledge and wisdom have been an inspiration academically and personally. De todo corazón, muchas gracias.

Northrop Grumman Corporation, for providing the funding for this research. I express my gratitude to Dr. David Muh and Dan Dillery.

Dr. Guifang Li, for his valuable comments and suggestions given by during the last months of this work. Also Dr. Javier Alda and Dr. José López, whose vast knowledge and love for science and teaching served as an inspiration.

My advising Committee: Dr. Aristide Dogariu, Dr. James Harvey, and Dr. Wasfy Mikhael.

The members of the Infrared Systems Lab: Peter Krenz, Todd Du Bosq, Dave Shelton, Larry Schneider, Jeff Tharp, Jeff Bean, Jeff Darchangel, Brian Monacelli, Brian Slovick, Lauren Rich, James Ginn, Sam Wadsworth, Chris Middlebrook, Charles Middleton, Joe Schelanko, Alex Dillard, Lou Florence, Tasneem Mandviwala, Sid Pandey, and Ismael Quijano. These are people that in one way or another provided insight, friendship, guidance, and fun times.

The CREOL staff members and other fellow graduate students. Dave Haefner, Tatiana Arriarán, Gail Drabzuck, Rachel Franzetta, and John Broky.

My friends at Catholic Campus Ministry and Most Precious Blood Catholic Church, for giving me an inspiration to grow personally and spiritually. Thanks for all the fun and for the opportunity to play music with you.

Raúl and Fifi Rodríguez, for giving me a helping hand when I first moved to the United States from the Dominican Republic. My home away from home.

My parents, Olga and Blas. Thank you for your sacrifice, love and good example. Being far from home has made me appreciate you more every day. Mami, Papi, gracias por su ejemplo de amor y sacrificio, por siempre procurar darnos aquello que ustedes no tuvieron. Blasito, Olgui, gracias por su cariño y ayuda incondicional. Gracias por su ejemplo de hombre y mujer cristianos.

My beautiful fiancée, my best friend, Pam, for putting up with me during the last couple of years of my graduate studies. My constant support during all the ups and downs. Thank you for always brightening up my day.

God, for giving meaning to it all.

TABLE OF CONTENTS

LIST OF FIGURES	xii
LIST OF TABLES	xvi
LIST OF ABBREVIATIONS AND ACRONYMS	xvii
CHAPTER 1: INTRODUCTION.....	1
1.1. Technical description	2
1.1.1. Atmospheric transmission.....	2
1.1.2. Passive vs. active imaging	4
1.1.3. Imaging architectures.....	7
1.1.3.1. Field of View (FOV) scanners	7
1.1.3.2. Staring or Focal Plane Arrays	9
1.1.3.3. Pupil Plane Imagers	9
1.2. Resolution of imaging systems	10
1.3. Aperture Synthesis	11
1.3.1. Digital Correlation	14
1.3.2. All-electronic aperture synthesis imaging	15
CHAPTER 2: MULTISPECTRAL, MMW SUBSURFACE AND THROUGH-BARRIER IMAGING.....	16
2.1. Landmine detection methods	16
2.1.1. Electromagnetic detectors	16
2.1.1.1. Metal Detectors	16

2.1.1.2. Ground Penetrating Radars	17
2.1.1.3. Electrical Impedance Tomography	18
2.1.1.4. X-Ray Backscattering	18
2.1.1.5. Infrared Systems	19
2.1.2. Acoustic/Seismic Systems	20
2.1.3. Explosives Detection	20
2.1.3.1. Explosive Vapor Detection	21
2.1.3.2. Bulk Explosive Detection	22
2.2. MMW Raster-Scan Imaging	23
2.2.1. Experimental Setup	23
2.2.2. Time-Domain Reflectometry	25
2.2.2.1. Principles of operation: Bandpass mode	26
2.2.2.2. Imaging setup	27
2.2.3. Other imaging tests	29
2.2.3.1. Buried cable imaging	30
2.2.3.2. Imaging through walls	33
2.2.3.3. Imaging at increased distances	35
2.3. Discussion	36
CHAPTER 3: FOUNDATIONS OF APERTURE SYNTHESIS	38
3.1. The two-element interferometer	39
3.1.1. The incident radiation	40
3.1.1.1. The fringe pattern function	41

3.1.1.2. One-dimensional antenna synthesis	42
3.1.2. Response of the receiving system to the incident radiation	44
3.1.2.1. Interferometer response as a convolution	45
3.2. Convolution theorem and spatial frequency.....	46
3.3. Two-dimensional synthesis	47
3.4. Effects of coherence	49
3.5. Numerical focusing	52
3.5.1. Near-field and far-field measurements	52
3.5.2. Phase front correction	54
CHAPTER 4: SPARSE APERTURE MILLIMETER-WAVE IMAGING SYSTEM	56
4.1. Active source.....	56
4.2. Scanning	57
4.3. Coherent detection using digital methods	61
4.4. Automation.....	63
CHAPTER 5: DIGITAL COHERENT DETECTION	66
5.1. Current methods for phase measurement	66
5.2. Proposed method	69
5.2.1. Phase detection using phase difference of harmonic component	69
5.2.2. Phase detection using digital I/Q demodulation	70
5.3. Experimental validation	72
5.3.1. Results and comparison with theoretical values	73
CHAPTER 6: IMAGING TESTS	75

6.1. Experimental Methods	75
6.1.1. Performance metrics	75
6.1.2. One-dimensional reconstructions.....	76
6.1.2.1. Point-sources.....	77
6.1.2.2. Extended targets.....	81
6.1.3. Two-dimensional reconstructions	83
6.1.3.1. Metallic ring reconstruction	84
6.1.3.2. Other targets.....	88
6.1.3.3. Concealed targets imaging.....	89
6.2. Discussion and conclusions.....	91
CHAPTER 7: STUDIES ON MINIMALLY REDUNDANT ARRAYS.....	93
7.1. Effects of redundancy in the selected configurations.....	94
7.2. Spatial frequency distribution of known array configurations.....	96
7.3. Simulations and experimental validation	101
7.3.1. Nine-element circular configuration	102
7.3.2. Nine-element cross configuration	104
7.3.3. Golay-9 configuration	107
7.3.4. Nine-element star configuration	109
7.4. Conclusions from the study.....	110
CHAPTER 8: CONCLUSIONS AND FUTURE WORK.....	113
8.1. Conclusions	113
8.2. Future Work	114

8.2.1. Component simplification.....	115
8.2.2. Miniaturization and hardware improvements	115
8.2.3. Other studies	116
APPENDIX A: TEST BED USER’S MANUAL	117
A.1. Motion control and Data Acquisition.....	118
6. Initialize port for communication with rotary stage	118
A.2. Signal Processing	120
APPENDIX B: SOFTWARE SCRIPTS	121
B.1. LabVIEW scripts.....	122
Needed Add-ons (LabVIEW):	123
MATLAB Scripts	123
Needed Add-ons (MATLAB):	123
REFERENCES.....	125

LIST OF FIGURES

Figure 1-1. Atmospheric attenuation in air, rain, and fog [3].	4
Figure 1-2. Spectral photon radiance vs. wavelength for blackbodies at 300 K	6
Figure 1-3. Scan format for single detector.	7
Figure 1-4. Performance of a large aperture can be replicated with smaller components using aperture synthesis principles.	13
Figure 2-1. Picture of the multispectral active mmW imaging system and its components. Inset: raster-scan path.	25
Figure 2-2. Imaging setup for the seeing through walls tests. Monostatic configuration.....	28
Figure 2-3. Comparison of imaging through drywall with and without use of time-domain analysis to eliminate barrier bounce.	29
Figure 2-4. Monostatic configuration for subsurface and through-barrier imaging using TDR. .	30
Figure 2-5. Cables buried at a depth of 10 mm.....	31
Figure 2-6. Cables buried at a depth of 25 mm.....	32
Figure 2-7. Cables buried at a depth of 35 mm.....	32
Figure 2-8. Results of imaging through drywall, ceramic tile, plywood and hardboard.	35
Figure 2-9. Comparison of image quality for 25 and 300 mm standoff distance for the active mmW imaging system.	36
Figure 3-1. Geometry of a two-element interferometer.....	41
Figure 3-2. Antenna radiation pattern and intensity profile of source.	45
Figure 3-3. The (l,m) plane and the unit circle.	48
Figure 3-4. Geometry of a distant coherent source and observation points P_1 and P_2	50

Figure 3-5. Plane waves travelling from the plane $z = 0$ to the plane $z = z_I$.	53
Figure 3-6. Spherical phase front and a tangential plane.	54
Figure 4-1. Stepper motor control schematic.	59
Figure 4-2. Electrical and mechanical components of test bed. Circular plate and 6 linear translation arms (top view)	60
Figure 4-3. Test bed mounted on programmable rotary stage. Cantilever arm offsets place detectors on the same plane.	61
Figure 4-4. Schematic diagram of analog down conversion stage.	62
Figure 4-5. Scanning algorithm flowchart.	64
Figure 4-6. Image reconstruction flowchart.	65
Figure 5-1. Conventional quadrature receiver model.	67
Figure 5-2. Geometry for experimental validation.	73
Figure 5-3. Phase difference measurements at three different values of \mathbf{h} . The “Harmonic component” and “Digital I/Q” methods are compared to the theoretical values.	74
Figure 6-1. Schematic for the experimental setup.	77
Figure 6-2. Amplitude and phase of theoretical and measured field distributions generated by a point source located 430 mm from the test bed.	78
Figure 6-3. Reconstruction of point source using focusing algorithm and signal correlation.	79
Figure 6-4. Reconstruction of point source without use of focusing algorithm.	80
Figure 6-5. Metallic ring used for the extended target reconstructions. Outer diameter: 126 mm, inner diameter: 84 mm.	82

Figure 6-6. Distribution of measured points for the one-dimensional reconstruction of metallic ring target.	82
Figure 6-7. Orthogonal one-dimensional reconstructions of ring target.....	83
Figure 6-8. Field plot (left) and reconstruction (right) of metallic ring using a 4-arm configuration.	84
Figure 6-9. Field plot (left) and reconstruction (right) of metallic ring using an 8-arm configuration.	85
Figure 6-10. Field plot (left) and reconstruction (right) of metallic ring using a 12-arm configuration.	86
Figure 6-11. Field plot (left) and reconstruction (right) of metallic ring using a 24-arm configuration.	86
Figure 6-12. Field plot (left) and reconstruction (right) of metallic ring using a full scan.....	87
Figure 6-13. Level with plastic casing and its dimensions.	88
Figure 6-14. Field map (left) and reconstruction (right) using for imaging of targets without circular symmetry. See Figure 6-13.....	89
Figure 6-15. Image of a hand saw inside cardboard envelope. Focus between 0 mm and 460 mm.	90
Figure 6-16. Image of a hand saw inside a cardboard envelope. Focus between 460 mm and 900 mm.	90
Figure 7-1. Golay-9 distribution and its autocorrelation.	97
Figure 7-2. Star configuration and its autocorrelation.	98
Figure 7-3. Circular configuration and its autocorrelation.	99

Figure 7-4. Cross configuration and its autocorrelation.	100
Figure 7-5. Calculated and measured reconstructions of a point source using a 9-element circular configuration.	103
Figure 7-6. Measured and calculated cross-sections of squared amplitude. Reconstruction of a point source using a 9-element circular configuration.....	104
Figure 7-7. Calculated and measured reconstructions of a point source using a 9-element cross configuration.	105
Figure 7-8. Measured and calculated cross-sections of squared amplitude. Reconstruction of a point source using a 9-element cross configuration.....	106
Figure 7-9. Calculated and measured reconstructions of a point source using a Golay-9 configuration.	107
Figure 7-10. Measured and calculated cross-sections of squared amplitude. Reconstruction of a point source using a Golay-9 configuration.....	108
Figure 7-11. Calculated and measured reconstructions of a point source using a 9-element star configuration.	109
Figure 7-12. Measured and calculated cross-sections of squared amplitude. Reconstruction of a point source using a 9-element star configuration.	110

LIST OF TABLES

Table 2-1. Construction materials used for the through-wall imaging studies and their description.....	34
Table 6-1. Digitizer parameters for reconstruction experiments	77
Table 7-1. Normalized coordinates for Golay-9 configuration.	96
Table 7-2. Normalized coordinates for star configuration.....	98
Table 7-3. Normalized coordinates for circular configuration.	99
Table 7-4. Normalized coordinates of cross configuration.....	100

LIST OF ABBREVIATIONS AND ACRONYMS

A	antenna radiation pattern function
BED	bulk explosive detection
$corr_n$	number of physical correlators
D	diameter of collecting aperture
DC	direct current. Also “zero frequency”
D_{exit}	exit pupil diameter
DFT	discrete Fourier transform
D_{int}	length of the baseline
ED	explosives detection
EIT	electrical impedance tomography
EMI	electromagnetic induction
EVD	explosive vapors detection
f	focal length
F	fringe pattern
F_B	bandwidth function
FOV	field of view
FPA	focal plane array
FPGA	field-programmable gate array
F_U	Fourier transform of complex field distribution U
FWHM	full width at half maximum
G	interferometer response function
GPR	ground penetration radar

HDPE	high density Polyethylene
i	imaginary unit =
I	angular intensity distribution function
IDFT	inverse discrete Fourier Transform
IED	improvised explosive devices
IR	infrared
k	wave number
K	Kelvin
l	direction cosine perpendicular to m
m	direction cosine perpendicular to l
mmW	millimeter wave
MS	mega sample
NA	not available/not applicable
n_d	number of detectors
NM	neutron methods
NQR	nuclear quadrapole resonance
PC	principal component
PCA	principal component analysis
P_d	probability of detection
PISLR	peak-to-integrated-sidelobe-ratio
PSF	point spread function
q	radius of minimum spot size
\vec{r}	Fourier transform of correlator output
R	correlator output function

RF	radio frequency
rms	root mean square
S	distance defining the far field
SNR	signal-to-noise
TDR	Time-domain reflectometry
TNT	trinitrotoluene
\mathbf{U}	complex field distribution
u	spatial frequency perpendicular to v
v	spatial frequency perpendicular to u
\vec{V}	visibility function
V_M	fringe visibility
VNA	vector network analyzer
z	distance from object to imager
δ	minimum resolvable separation
δ	delta function
θ	angle of elevation
λ	wavelength
ν	frequency of radiation
τ_g	geometric delay
Φ	Phase deviation

CHAPTER 1: INTRODUCTION

Imaging systems have been investigated and developed for hundreds of years. But since the principles of the capture of electromagnetic radiation have been known, the need of extending the ranges where those cameras work has existed. The discovery of infrared radiation by Herschel in 1800, and, later, the discovery of X-rays by Röntgen in 1895, provided an expansion of the region of the electromagnetic spectrum that could be used for imaging. Numerous advantages derived from the ability of capturing radiation outside the visible: from military (night vision) to medical (x-ray radiography) to even entertainment and arts (infrared photography).

Other regions of the spectrum were also shown to be able to provide an image. Radiation that falls within the region of the spectrum with wavelengths between 0.1 and 1 cm ($1\text{mm} < \lambda < 10\text{mm}$) is called millimeter wave. Imaging in this region has gathered attention over the last decades for its ability to generate pictures even through media that is opaque in the visible and infrared. It has been proven to penetrate certain construction materials, thin layers of soils, clothing, dust and clouds. Because of its low atmospheric attenuation, imaging using millimeter waves is most suitable for astronomy and military observations. Current and possible future applications include airport security scanning for drug and concealed weapon detection, subsurface imaging, marine navigation in fog, imaging devices for collision avoidance in fog, Earth observations, and radio astronomy, among others.

However, long wavelength imagers still face important challenge, and that is angular resolution. Angular resolution in optical systems is directly proportional to the wavelength of radiation. The wavelength of infrared and visible radiation is in the order of microns (10^{-7} to 10^{-6} m), which means that the theoretical resolution of images using millimeter-waves worsens by three orders of magnitude, when other system parameters are kept the same.

Several techniques have been studied to overcome this challenge. In the following sections, we describe their technical characteristics and methods to improve image quality.

1.1. Technical description

In our discussion of the performance of a system designed for near range sensing, we analyze the three physical parameters that have the largest impact on the imaging device. First, we look at the effect of atmospheric transmission of radiation. Though the goal of this research is close range detection and identification of hidden threats, an analysis for remote sensing is also included as an extra feature that could be exploited in future applications. Second, we discuss passive and active illumination and, finally, a short analysis of the differences between focal plane arrays (FPA) and pupil plane scanners.

1.1.1. Atmospheric transmission

Propagation through the atmosphere attenuates millimeter-waves. Attenuation over this frequency range is generated by the absorption lines of oxygen and water vapor. Besides water

vapor and oxygen, other gasses attenuate radiation in the microwave spectrum, such as O_3 , SO_2 , NO_2 , and N_2O . However, their concentrations at sea level are so small that their contribution is negligible. Water vapor has spectral absorption lines at 22.2 GHz and 183 GHz, whereas oxygen presents a large number of lines distributed along the 50 – 70 GHz (known as the oxygen complex) and an extra line at 118.75 GHz. Molecule collisions cause broadening of the oxygen complex lines, making them blend, producing a continuous absorption band around 60 GHz [1]. In the 30 – 300 GHz region of the spectrum there are multiple bands, called windows, where the absorption is minimal, specifically at 35, 94, 140, and 225 GHz. These windows are visible in Figure 1-1, in the section highlighted in green.

As in any optical system, the image resolution is directly proportional to the wavelength of radiation, with shorter wavelengths capable of higher resolution images. The tradeoff between wavelength and resolution, combined with the lower attenuation of longer wavelengths, means that in the design of a through-barrier imager, a compromise must be made between image resolution and penetration. This tradeoff between attenuation and resolution is also valid for radiation propagating through solid media [2].

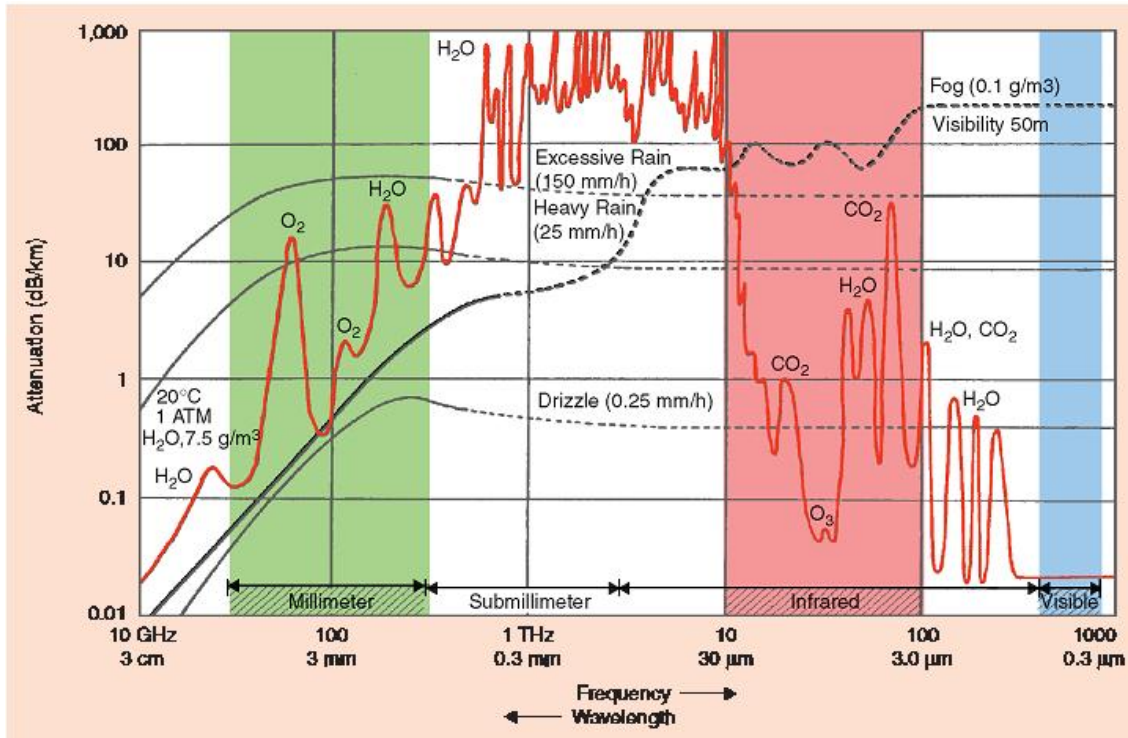


Figure 1-1. Atmospheric attenuation in air, rain, and fog [3].

Compared to the spectral radiance of the extremes of the mmW region, and according to the Rayleigh-Jeans radiation law for objects at room temperature (300 K), more photons are emitted at higher frequencies. However, this higher emission of photons is valid for the imaged scene and the radiation's propagation medium. This radiation emitted by the propagating medium has the effect of reducing the contrast of the image.

1.1.2. Passive vs. active imaging

The effectiveness of any imaging device depends on its ability to capture the radiation emanating from the target scene. Passive and active imagers differ in the way this radiation is generated, with the former taking advantage of the objects thermal emissions, and the latter measures the

reflected radiation of a relatively high power source. The amount of power available in each situation varies greatly and depends on the region of the spectrum to be measured, especially for passive imagers.

The development of a passive mmW imager faces the challenge of detecting the very low power available in this region. Despite the success infrared imagers have had using the passive approach; this cannot be replicated as easily using millimeter waves. Objects at terrestrial temperatures have a spectral radiance curve that peaks around 10 μm , with power continually decreasing for longer wavelengths (see Figure 1-2). For wavelengths in the mmW region, emitted power is 8 orders of magnitude lower, with low power levels being the greatest constraint for detectors. Nevertheless, for military applications, the lack of active elements is a great advantage, as this gives a means for covert detection.

However, passive imagers can increase their effectiveness by measuring radiation reflected from illuminating sources, thus making the objects appear to have a larger contrast compared to their surroundings. Passive scenes can be greatly enhanced by reflecting the “cold sky”. The space temperature is below 100 K, meaning that contrasts of up to 200 K can be achieved. One caveat is that reflective objects must be oriented at specific angles, and non-reflective objects must be blackbody emitters. Another way to illuminate a scene could be by measuring the reflected radiation coming off a heated source. This type of active incoherent illumination has the advantage of providing wideband emissions, but this source could be easily detected by infrared imagers, thus truncating the covertness advantage.

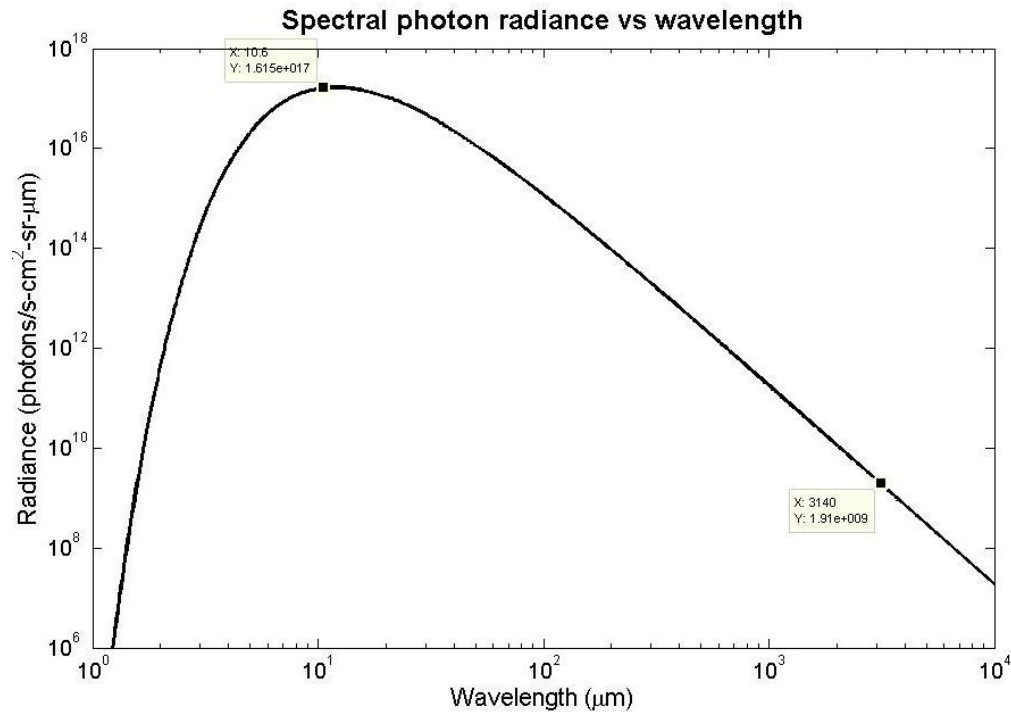


Figure 1-2. Spectral photon radiance vs. wavelength for blackbodies at 300 K

If, on the other hand, the natural illuminating sources are blocked, such as if the target is located indoors or buried, the contrast gets significantly reduced. Active systems can increase the contrast by flooding the scene with artificially generated radiation. This radiation is usually narrowband because it is easier to generate and simplifies the detection process. Active imaging presents the advantage of being able to work under conditions not suitable for passive approaches, increases the contrast in the image, and relieves some of the constraints the detectors have to endure; but comes at the expense of adding extra elements and is more difficult to conceal.

1.1.3. Imaging architectures

This section discusses various techniques for detecting electromagnetic radiation for imaging. Two methods can be used to generate imagery: focal plane or pupil plane scanning. Focal plane scanners measure the flux collected by the aperture at specific points, generating an image by combining these measurements into a single two-dimensional array. Pupil plane imagers, on the other hand, measure the electric field on the collecting aperture and, through Fourier inversion, reconstruct the intensity distribution that produced such fields.

1.1.3.1. Field of View (FOV) scanners

Our discussion of FOV scanners begins with the analysis of the single-detector type. The image is obtained by scanning the vertical and horizontal FOVs of a real aperture, in a raster mode. This type of scanning displaces the detector across one dimension and then repeats this process in the following line, until the full FOV is sampled. See Figure 1-3.

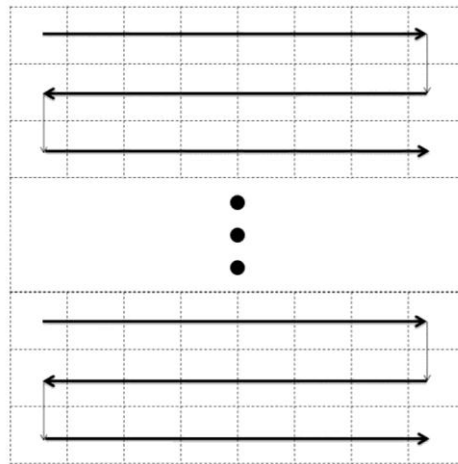


Figure 1-3. Scan format for single detector.

The primary advantage of this approach is the maximization of the system efficiency by minimizing the number of components. An added benefit of using a single detector is the lower cost, weight, and volume that come from performing all the functions of a staring array with a single element. This advantage, however, comes at the expense of sacrificing other important parameters, such as the integration time and the signal-to-noise ratio (SNR); which are intrinsically related; as the SNR increases with longer integration times. Unfortunately, many systems have very demanding frame rates that prevent an arbitrary increase of the dwelling time.

Multiple-detector scanning is the next logical step in our discussion. By increasing the number of detectors from 1 to n_d , the system can capitalize on the advantage of collecting more than a single point at a time. Such arrangements are called parallel or series scanners, depending on whether the translation of the array occurs orthogonally to or along the direction of the array, respectively. The disadvantages of such a system include having more components and, in most cases, higher costs, larger volumes, and more complex systems. On the other hand, and compared to the single-detector case, the advantages are not only reduction of the frame time (by a factor of n_d), but also boosting of the SNR:

$$SNR \propto \sqrt{n_d} \tag{1.1}$$

1.1.3.2. Staring or Focal Plane Arrays

The principle of operation of a staring system is similar to the FOV scanners, with the difference that this class of imager generates imagery by collecting radiation from the whole FOV during the entire frame time. A two-dimensional collection of detectors improves the performance by reducing the amount of noise perceived by the system. The bandwidth of each detector is reduced thanks to the extended dwell times, which in turn reduce the rms noise. Also, just as the single detector scanners, the SNR is proportional to the square root of the number of detectors, as described in equation (1.1).

However, the challenges introduced by the presence of multiple detectors go beyond the physical and mechanical implications of having a large number of elements and their synchronization. Besides the temporal noise sources, the nonuniform nonlinearities between pixels produce a fixed-pattern noise that repeats in every image. This is called the spatial noise, and, in many advanced staring arrays, it is the limiting noise [4, 5].

1.1.3.3. Pupil Plane Imagers

The FOV scanners described in the previous section sample the flux collected from the scene and each detector constitutes a pixel in the final image. If, instead of sampling the focal plane, the detectors sample the pupil plane, then imagery can be generated by simulating the effects of a lens through post processing. Pupil plane imaging requires a more complicated signal treatment and imposes latency in the system, but presents several advantages that are useful for long wavelength imaging.

Pupil plane imagers can take advantage of simpler arrangements that derive from the use of the aperture synthesis principle, which has been used successfully by the radio astronomy community for several decades. The use of a synthesized aperture allows replacing a large real aperture with a thinned array of individual small-aperture antennas that generate imagery by having their signals correlated in pairs. The signals are correlated in the equivalent of a two-element interferometer, the basic part of an aperture synthesis imager.

As opposed to FOV measurements, pupil plane measurements are performed in the spatial frequency domain and depend on the physical separation of the correlated pairs, called the baseline. Finally, a two-dimensional representation of the intensity distribution can be generated by Fourier inversion which has an angular resolution dependent on the longest baseline of the system [6].

1.2. Resolution of imaging systems

An analysis of the angular resolution is included to assess FOV scanners and pupil plane imagers and compare their performance. Independent of the imaging approach, optical systems are limited by specific physical parameters. For this discussion, a circular aperture is used, but similar conclusions can be obtained with any other shape.

The resolution of an optical system depends on the area of the collecting aperture (D), the focal length (f) of the optics involved, and the wavelength of the radiation (λ). Ideally, the image plane should reflect perfectly the object plane, but because of the limits imposed by diffraction, the

minimum resolvable feature has a finite dimension. The radius of the minimum spot size (q) is given in equation (1.2) [7].

$$q \approx 1.22 \frac{f\lambda}{D} \quad (1.2)$$

The consequences of equation (1.2) have an important impact on mmW imagers. With all parameters being the same, the resolution of such systems is three orders of magnitude worse than equivalent visible and IR systems. However, this deficiency can be partially compensated with an increase in the effective collecting aperture. As most practical applications prevent increasing D in the same proportion, mmW imagers do not have the same performance as their visible and IR counterparts. Despite this limiting factor, the advantages and applications mentioned earlier outweigh the drawbacks.

Enlargement of the pupil plane has a positive effect on the minimum resolvable spot size, but provides a new set of challenges. A linear increase in the diameter implies a quadratic increase in area and a cubic increase in volume. In many occasions, this generates a burden that is unacceptable for portable systems. Aperture synthesis can then be used to provide the desired image quality enhancement, while keeping the area, volume, weight, and cost to a minimum.

1.3. Aperture Synthesis

One of the factors that have hindered developing mmW imagers is the large aperture size needed for acceptable imagery. Aperture synthesis techniques have been used in radio astronomy to

overcome this challenge. These techniques can be applied for other regions of the spectrum, specifically millimeter waves. The image resolution of a large aperture mmW system can be achieved with a thinned array of smaller detectors with a maximum separation equal to the diameter of such aperture, as illustrated in Figure 1-4.

Each pair of detectors collects signals which are correlated to obtain a frequency component of the spatial Fourier spectrum. These spatial frequencies are dictated by the distance separating each pair of detectors, called the baseline. An image can be reconstructed by performing a Fourier inversion of the sampled spatial frequencies [8]. Sampling spatial frequencies requires not only coherent detectors, but also transmission lines that preserve the phase throughout within $1/10$ of a wavelength [9]. Signals below 67 GHz can be transmitted through thin coaxial cables, but above this value, rigid waveguides are needed [10]. The use of rigid waveguides presents a significant problem for systems where detectors are not in fixed positions. A number of approaches have been proposed and built to minimize losses and preserve the phase of the signals. These approaches include optical up-conversion and digital heterodyne-down-conversion.

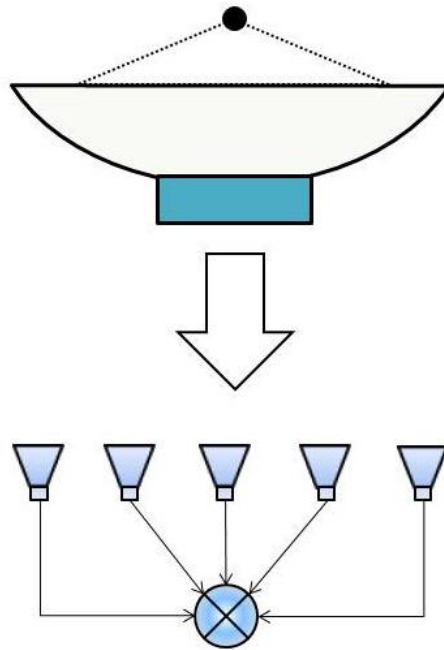


Figure 1-4. Performance of a large aperture can be replicated with smaller components using aperture synthesis principles.

Optical up-conversion relies on electro-optical modulation techniques to convert received mmW radiation into sidebands on an optical carrier. Once mmW signals are converted to optical signals, they can be coupled to optical fibers, which are inexpensive, flexible, and with very low losses. Digital heterodyne-down-conversion takes mmW signals and modulates them onto a carrier with a lower frequency. Signal can then be coupled to coaxial cables, which present the same advantages as the optical fibers. Though in principle both approaches can work with similar performance, each has advantages and disadvantages that would make it more or less suitable for specific situations. In the following subsection digital correlation is discussed, as well as which technique, optical up-conversion or heterodyne-down-conversion, is more suitable for digital processing.

1.3.1. Digital Correlation

The mmW signal of each detector is correlated with the signal of every other detector. The correlated signals are used to build up the visibility function. Correlation in pairs presents the advantage that the number of points in the visibility function grows with the square of the number of detectors, but implies that the physical number of correlators ($corr_n$) grows in the same proportion, as described by equation (1.3).

$$corr_n = \frac{n \cdot (n-1)}{2} \quad (1.3)$$

The principles of passive imaging require that the correlations be performed with signals measured at the same time, as the coherence function is not constant through time. For active systems, however, the coherence function depends on the stability of the source and, therefore, the signals need not be sampled at the same time. Coherence is held constant by the presence of a source. In this case, a system can measure the signals at specific points across a plane in different time slots. If the signals are sampled and stored, correlation can be performed during post processing. The advantages of this approach include the ability to substitute the physical correlators for digital processing, which can minimize the cost, size, and weight of a system. With current digitizer technologies, signal sampling is limited to those with frequencies below 1 GHz, to satisfy the Nyquist theorem. Given this constraint, to take advantage of digital correlation, only heterodyne-down-converted signals can be digitized and stored for proper post processing.

1.3.2. All-electronic aperture synthesis imaging

Based on preliminary work with a multispectral mmW imager for subsurface and through-barrier imaging, we studied the capabilities and limitations of various approaches for mmW imaging. These studies established the foundation for this dissertation and motivated the search for alternatives to overcome the limitations. The research is focused in the design, assembly, and testing of a test-bed consisting of an active source at 94 GHz and a synthesized array of coherent mmW detectors, mounted on arms that extend radially on a rotary table, for effective scanning of a circular area with a maximum diameter of 900 mm. The signal is down-converted using a two-step heterodyne receiver with digital in-phase and quadrature detection. Signal correlation is performed using the digitized data, which is stored for post processing, electronic focusing, and image reconstruction.

This dissertation is organized as follows: Chapter two presents imaging tests through some construction materials typically found in homes and buildings in the United States. Discussion of the results follows all measurements. Chapter three explains the mathematical and physical foundations of aperture synthesis and the principles of their application. Chapter four is a description of the test bed used. Chapter five discusses some novel techniques for digital phase detection. Chapter six describes the experiments validating the theory. In chapter seven, an analysis on the effects of redundancy on image quality is shown. Finally, chapter eight ends this document with conclusions and where the research can be expanded.

CHAPTER 2: MULTISPECTRAL, MMW SUBSURFACE AND THROUGH-BARRIER IMAGING

Despite efforts to clear vast areas of land, there are still more than 100 million active land mines scattered across sixty-eight countries worldwide. These devices, and their long field life, constitute a serious threat by killing or maiming thousands of civilians every month. In other situations, this threat interferes with the use of arable land, hindering economic development and generating social problems.

2.1. Landmine detection methods

Demining can be intended for military or humanitarian purposes. In either case, the finding or destruction rates need to be higher than 80% (99.6% or better for humanitarian purposes). Several sensor technologies are being studied in order to achieve these stringent requirements. The current demining methods can be classified into three major groups: electromagnetic, acoustic/seismic, and explosives detection.

2.1.1. Electromagnetic detectors

2.1.1.1. Metal Detectors

The standard metal detector is the most common electromagnetic method. Metal detectors have been used for demining purposes for decades, and have changed very little since War World II. They work on the principle of electromagnetic induction (EMI). EMI detectors generate a time-varying magnetic field with a transmitter coil, which generates an electric field on any buried metal object. This electric field, in turn, creates an electromagnetic field, which is captured by

the receiver coil and converted to an audible signal. Current technologies allow for very sensitive detectors, meaning that the probability of detection (P_d) is very high, even for mines with relatively small metal content. The downside to this approach is that the false-alarm ratio increases dramatically, as metal detectors do not provide a means for identification. Other cluttering elements are captured by the detector, such as metal cans, bullet casings, shrapnel, and even metal present in rocks, significantly slowing the demining process down [11].

2.1.1.2. Ground Penetrating Radars

Ground Penetrating Radars (GPR) measure the reflection of electromagnetic radiation generated from discontinuities in the dielectric constant of the objects in their field of view. Discontinuities are generated not only by metal/soil, but also by plastic/soil boundaries. This increases the P_d of low metal content targets. As a type of radar, location and ranging is possible with this system, as well as identification of threats, in certain cases.

The tradeoffs of this approach are the depth of penetration and resolution. Longer wavelengths have deeper penetration, but lower resolution, and vice versa. Imaging is possible, but the resolution is usually very low to discriminate items without automatic recognition algorithms. The main advantage, compared to EMI detectors, is improved sensitivity for nonmetallic casings, possibility of location and ranging, and identification of threats. The disadvantages are a result of the increased sensitivity and signal attenuation. With increased sensitivity, the possibility for false alarms also increases as now roots, rocks, and water pockets become sources of clutter. The

presence of moisture, scattering, and other characteristics specific to each situation create signal attenuation.

2.1.1.3. Electrical Impedance Tomography

The Electrical Impedance Tomography (EIT) is based on a two-dimensional array of electrodes located on the ground that use electrical currents to image the conductivity distribution of the medium under investigation. The collected data is then processed and an image is generated based on this information. As both metal and nonmetal mines generate anomalies in the conductivity distribution of the soils, this method can generate data suitable for their detection and location

The advantages of this method are that it can detect and locate both metal and nonmetal mines, and that it works in environments with high levels of moisture. Unfortunately, EIT requires the electrodes to be in direct contact with the soils, which might detonate a mine. It also does not perform as well in excessively dry and nonconductive terrains, such as rocky and desert like terrains.

2.1.1.4. X-Ray Backscattering

Wavelengths of X-Rays are very short compared to regular landmine dimensions. In principle, this could be used to generate high resolution images, but pass-through imaging is a physical impossibility because of the very rapid attenuation of X-Ray radiation in soils. However, backscattered radiation can be used to take advantage of the different mass densities and physical

properties of landmines and their surrounding soils. Advances in X-Ray sources have made it possible to generate compact sources that allow the possibility of even man-portable devices.

Despite the physical capability of X-Ray backscatters to detect buried objects, the advantages do not compensate for the disadvantages. The drawbacks include actual and perceived risks of using X-Rays, relatively low resolution of the images, and, in short, not offering any significant advantage compared to other electromagnetic methods.

2.1.1.5. Infrared Systems

These systems are based on measuring the temperature difference between where the landmines are buried and their surroundings. The temperature difference is generated by the way man-made objects and undisturbed soils and natural elements give off heat. The temperature difference can be due to natural solar radiation or artificially enhanced using infrared lasers and high-power microwave radiation.

The main advantages of this method include the large standoff distances at which the elements can be detected, the systems can be made lightweight, and, when mounted on airborne vehicles, could be effective for the scanning of large areas. Unfortunately, the penetration depth of infrared radiation is not good enough for the detection of buried items, are sensitive to weather, and, because of their dependence on thermal emissions, measurements need to be performed within the ideal time frames during the day.

2.1.2. Acoustic/Seismic Systems

The principle of operation of acoustic systems is similar to the electromagnetic methods, in the sense that the soils are being flooded with waves and their reflection is measured to determine where anomalies occur. Acoustic methods distinguish themselves from electromagnetic methods in that the former measures mechanical differences between the soils and the landmines and the latter measures electrical differences. In a typical acoustic system setup, an off-the-shelf loudspeaker generates sound waves that are directed toward the ground. Some of this radiation penetrates the soils, and the mechanical differences between the targets and the medium creates reflections that are captured by a set of specialized detectors. Among the detectors used for this purpose we count Doppler vibrometers, radars, ultrasonic devices and microphones.

The main disadvantages of acoustic/seismic systems are their shallow penetration (it is difficult to find mines buried deeper than one mine diameter) and the difficulty on measuring the displacements created by the vibrations (approximately 1 μm), which make the process very slow. However, improvements are being made, especially with the use of multiple detectors: increasing the number of detectors by a factor of N increases the speed also by a factor of N .

2.1.3. Explosives Detection

Other approaches that do not involve the presence, emission, or absorption of mechanical and electromagnetic waves have also been tried for the detection of buried threats. These methods rely on the finding of explosives, instead of highlighting the casings containing them. As such, Explosives Detection (ED) has the advantage of only focusing on the desired chemicals while

being immune to the typical false alarms that plague acoustic and electromagnetic approaches. Because ED methods do not rely on optics principles, they are only briefly mentioned to complete the analysis of landmine detection techniques.

2.1.3.1. Explosive Vapor Detection

Explosive Vapor Detection (EVD) operates on the principle that, nearly always, buried threats will leak explosives or chemical derivatives into their surroundings. Typically, about 95% of the leaked chemicals will adsorb into the soil, while the remaining 5% will travel away in the form of vapors. The main challenge consists in detecting the extremely low concentrations (in the order of 10^{-15} grams per milliliter) and the weather effects on the way the vapors travel.

Vapors are detected using either biological or chemical methods. Biological methods rely on the training of living beings to react to the presence of the vapors. Hundreds of trained dogs, thanks to their keen sense of smell, have been used in Afghanistan for landmine detection with a 95% detection rate under favorable conditions. Other studies have tried to develop techniques using rats and bees, where these have been trained to associate the desired chemicals with food. Finally, a strain of bacteria that fluoresces in the presence of TNT was engineered by researchers during the 1990's. In principle, bacteria would be sprayed over the desired area, possibly using airborne vehicles, and allowed to glow for several hours. Later a team would survey looking for the presence of fluorescent bacteria.

Chemical methods try to emulate the sense of smell, where the response of special receptors is measured when exposed to certain chemicals. Fluorescent polymers that react to the presence of explosive vapors have been investigated. When vapors containing explosives get in contact with the polymers, the polymers' fluorescence temporarily decreases. This reduction in emission is captured by an optical amplification device, which translate these variations to electric signals.

2.1.3.2. Bulk Explosive Detection

Just as with the EVD technique, Bulk Explosive Detection (BED) aims at detecting the actual threat, as opposed to the casings containing them. Two methods take advantage of the nuclear reactions of bulk explosives for their detection: Nuclear Quadrapole Resonance (NQR) and Neutron Methods (NM).

NQR is a radio frequency (RF) technique where a transmitter coil induces an electromagnetic pulse on the soil being probed. This RF pulse is tuned to a resonance frequency of the nuclei of the expected explosives, and a receiver coil then measures the generated fields. NQR is similar to EM detectors in the sense that both illuminate the target with a signal and measure its response, but differs in the cause of this response. This method is not affected by the presence of clutter, but by the SNR, which increases with the square root of the interrogation time and linearly with the mass of the explosives. A success rate as high as desired can be achieved if enough time is given. Interrogation times of about 0.5 to 3 minutes achieve a P_d of 0.99 and false-alarm ratios better than 0.05.

Finally, NM rely on probing the soil with and measuring the return of neutrons. Differences in the returning neutrons can be used to determine the chemical composition of the medium under investigation. To this day, NM have limited applications, with only thermal neutron analysis in use on the field. Only one technique, neutron moderation, has the potential for man-portable systems. Overall, NM lag in usability compared to the detectors described in this chapter.

2.2. MMW Raster-Scan Imaging

The use of active mmW imaging for landmine detection provides several advantages with respect to other EM detectors, acoustic systems, and explosive detectors. The high rate of false alarms of metal detectors; the relatively low resolution of GPRs, X-Ray backscatter imagers, and acoustic systems; the high risks involved with Electrical Impedance Tomography; and the time constraints and weather limitations of infrared imaging; minimize their viability for effective detection and identification. Explosive detection techniques are still in their development phases and provide reduced capabilities for deployable systems [11-13]. A multispectral 90 – 140 GHz mmW imaging system operating capable of subsurface imaging was developed for landmine detection by Du Bosq et. al. Principal Component Analysis (PCA) was used for dimensionality reduction and image enhancement.

2.2.1. Experimental Setup

The raster scan imaging system uses an Anritsu vector network analyzer (VNA) operating from 90 GHz to 140 GHz. Horn antennas with 16 degree radiation patterns provide an interface between the VNA and free space. Radiation is focused using HDPE lenses, in both the

transmitter and receiver arms. Samples under observation are mounted on a computer controlled translational platform. The platform covers a maximum area of $200\text{ mm} \times 200\text{ mm}$ with a maximum displacement velocity of 50 mm . An ECCOSORB CV broadband mmW anechoic foam was placed behind the sample to reduce reflections from the optical table. The setup is configured to work in bistatic (Figure 2-1) or monostatic (Figure 2-2) configuration.

Buried samples were placed inside a $20.3 \times 20.3 \times 9.5\text{ cm}$ with a raster-scan pattern for the images presented was 29×29 points, with a 5 mm separation between points, unless otherwise specified. Each point was sampled using 51 different frequencies between 90 and 140 GHz , with 1 GHz steps.

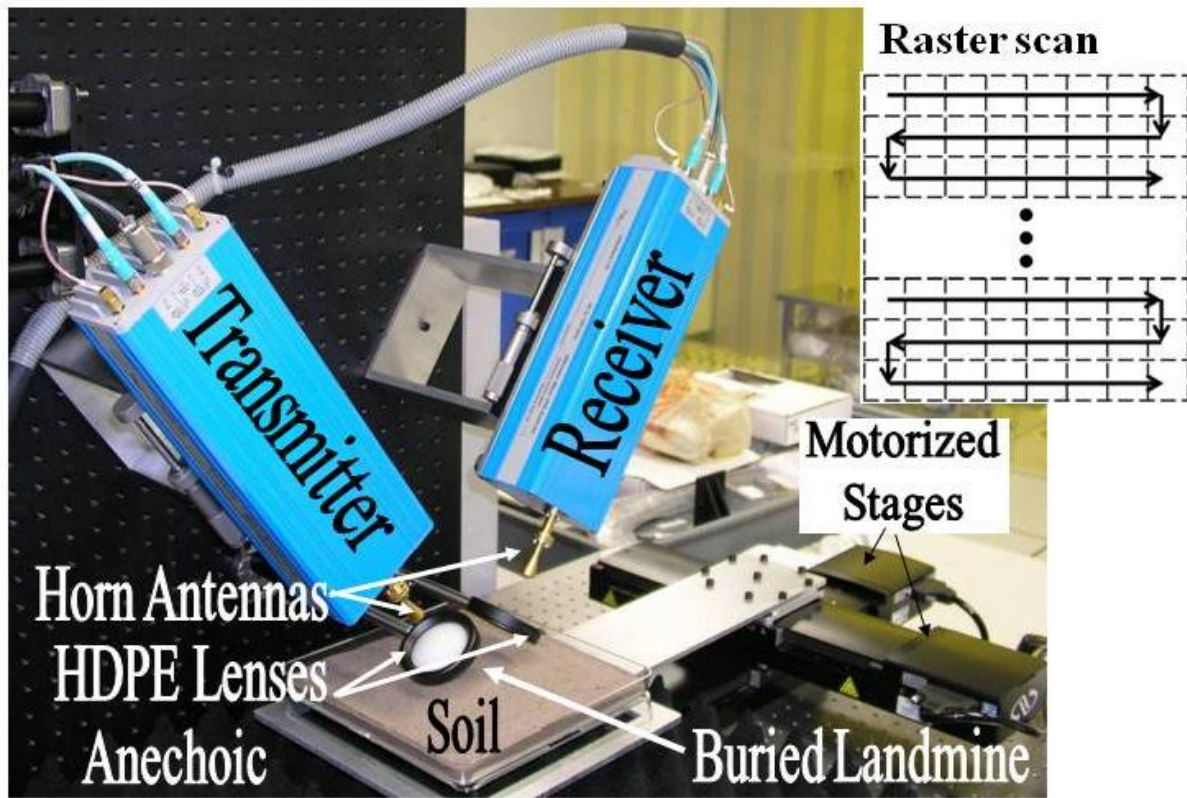


Figure 2-1. Picture of the multispectral active mmW imaging system and its components. Inset: raster-scan path.

2.2.2. Time-Domain Reflectometry

In an active imaging system, the magnitude of the intensity of each pixel is given by the sum of the reflections of all the elements between the source and detector. Isolation of these reflections increases the SNR and, therefore, image quality. Time-domain reflectometry (TDR) analysis was explored to assess its effectiveness for the reduction of barrier bounce.

Time-domain reflectometry has been used in electrical instrumentation to measure the characteristics of transmission lines. It detects the presence, type, and location of a discontinuity

by measuring the complex reflection of a transmitted pulse and the time delay of such reflection. This technique can be translated to free-space radiation, if we look at the experimental setup, as an infinite transmission line with impedance discontinuities in between. Each of these discontinuities can be isolated from the rest and only focus on the desired ones. Once the boundaries are identified, the time-domain signals are apodized so the undesired reflections are removed. A time-domain signal can be reconstructed from frequency-domain measurements performing a discrete inverse Fourier transform.

2.2.2.1. Principles of operation: Bandpass mode

There are two main modes of operation for VNA time-domain analysis: lowpass and bandpass mode. Bandpass mode is the most suitable for mmW (90 – 140 GHz) imaging because, as opposed to lowpass mode, it does not require measuring spectral response starting at 0 Hz (DC).

To generate the signal in time domain, the measured point's frequencies are shifted down so they are centered at zero, with the lower half falling on the negative side. Taking this array of frequencies, an IDFT is performed. To compensate for the initial shifting, the result of the IDFT is multiplied by a complex factor that is a function of the original frequency shift. This means that the computed time domain response is complex. In this case, the magnitudes of these computed values are displayed.

In any case, the limiting parameters for time-domain analysis are the resolution and the alias-free range. The resolution depends on the bandwidth of the measurement. A 90 – 140 GHz bandwidth

ensures approximately 3 mm resolution. This means the targets only need to be located farther than this distance to be distinguishable from the interface.

A consequence of the periodic nature of discrete sampling is aliasing. To have an alias free range (given in units of time or, if multiplied by the speed of the radiation, in units of length) long enough to be able to reach the target, the frequency step in the VNA must be set to 0.5 GHz, which, for a bandwidth of 50 GHz, translates to measurements having 101 frequencies. Image frames obtained with each frequency are fed to the PCA code already written, modified to take into account the different number of frames.

2.2.2.2. Imaging setup

TDR is based on the measurement of reflected signals propagating across a medium, and, therefore, requires the setup to be operated in monostatic configuration, as shown in Figure 2-2. The translation of the target is as described in section 2.2.1 and the VNA is set according to the description in section 2.2.2.1.

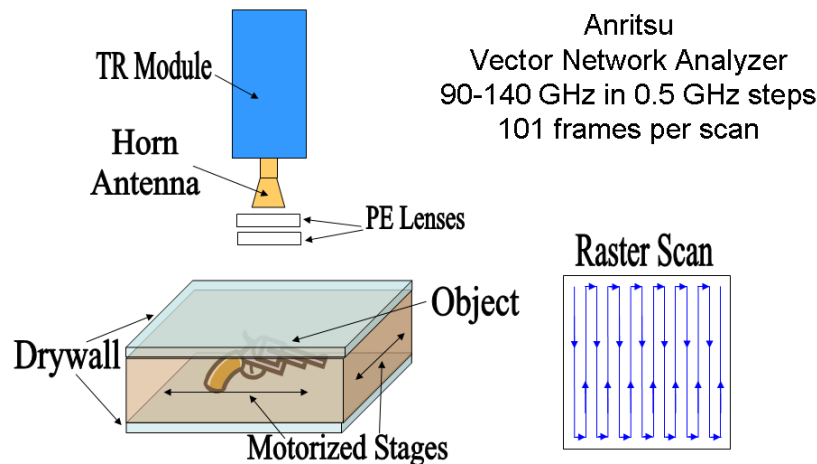


Figure 2-2. Imaging setup for the seeing through walls tests. Monostatic configuration.

The first experiment consisted in repeating one of the previous tests for comparison and assessment of the image quality with and without elimination of the barrier bounce. Figure 2-3 shows the comparison of the image of a target situated behind a 12.7 mm thick drywall sheet. The upper half of Figure 2-3 shows the images obtained without using TDR. The target is still visible in the mean value of the principal component and in the standard deviation of the higher components. In the remaining four images, the noise level is too high to determine with confidence the presence of an object. The lower half shows the results when TDR is used to eliminate the first bounce. All six frames can be used to determine with confidence the presence of a target. The boost in SNR is significant, especially in the image obtained from the standard deviation of the higher components. In the case of this metallic target, the boost also produces spreading of high reflection points due to saturation.

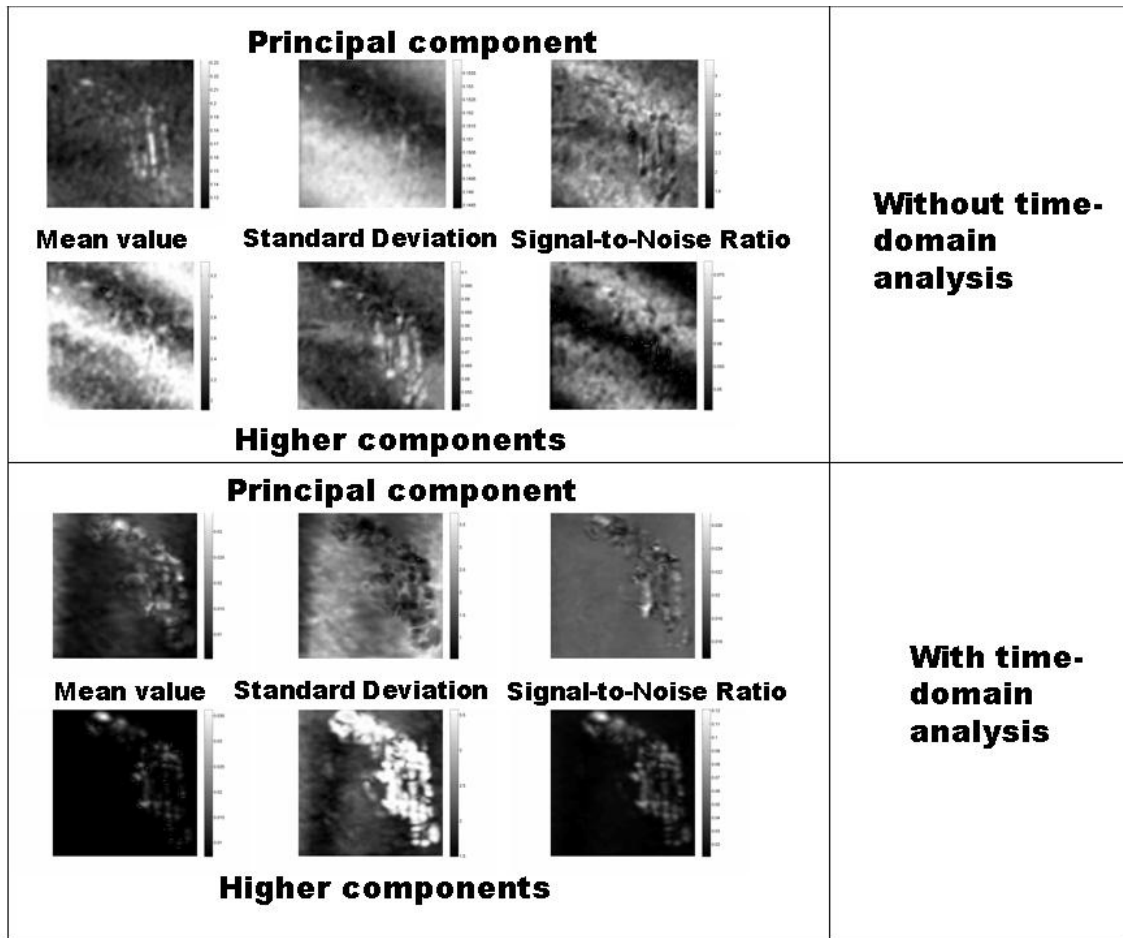


Figure 2-3. Comparison of imaging through drywall with and without use of time-domain analysis to eliminate barrier bounce.

2.2.3. Other imaging tests

Multiple experiments were conducted with the active mmW imaging system to test its limits and capabilities, including subsurface and through-barrier tests. The subsurface tests were focused on the ability to image electrical cables with thicknesses below the theoretical resolution limit of the system. The motivation for these experiments is to aid in the detection of buried improvised explosive devices (IED), which may be linked to controls or other explosives through electrical cabling.

2.2.3.1. Buried cable imaging

The raster-scan imaging system was set to obtain 101 frames per scan, with a frequency span of 90 to 140 GHz and 0.5 GHz step size. The scanning area was selected to be 140 mm × 140 mm with 2 mm step size, for 71 × 71 pixels per frame. The elements to image were a gauge 18 stranded audio cable, gauge 24 extension cable, and a three conductors gauge 22 electrical cable. All the cables were enclosed with a plastic insulation external cover. The soil type selected was sand, and the buried depths were chosen to be 10, 25, and 35 mm. Figure 2-4 shows the experimental setup.

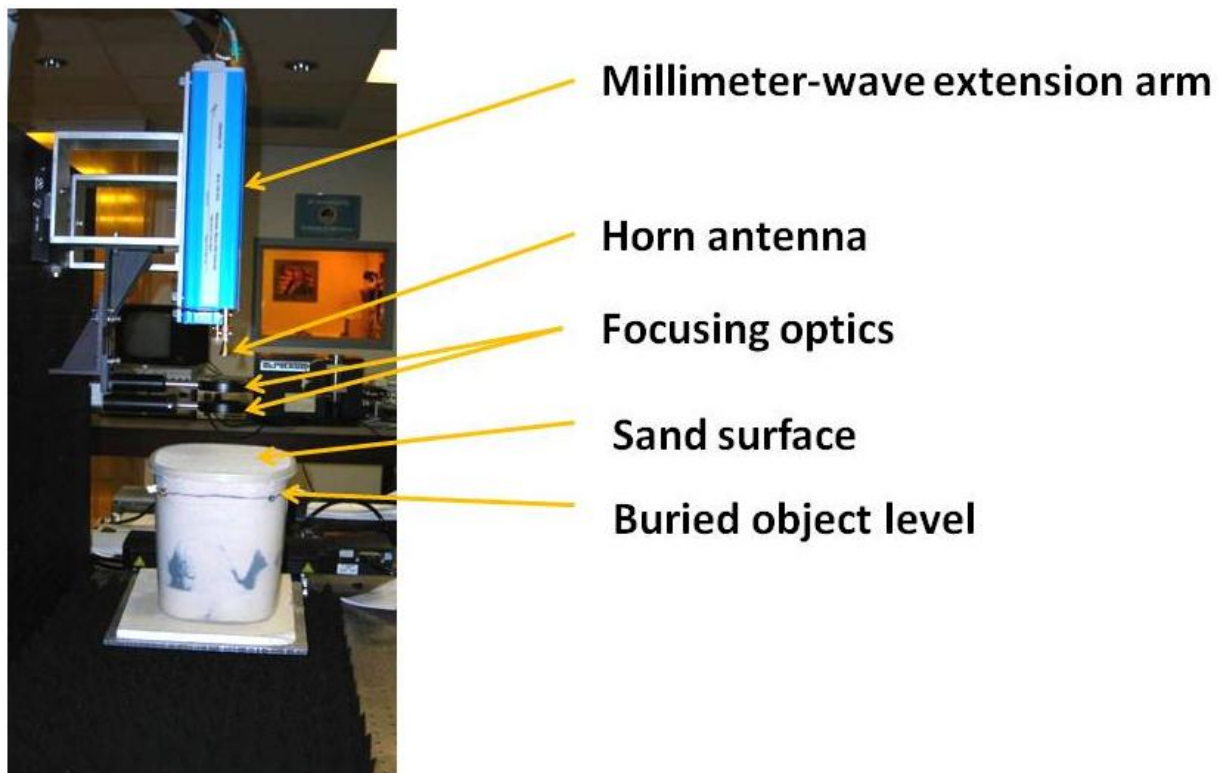


Figure 2-4. Monostatic configuration for subsurface and through-barrier imaging using TDR.

The highest resolution was achieved for a buried depth of 25 mm (Figure 2-5). The reason for the perceived decreased resolution in the shallowest depth is a side effect of the apodization process: the width of the window function was large enough to partially eliminate the reflection coming from the cables. The highest contrast was achieved at 25 mm of depth, as the window function was able to isolate the ground from the target (Figure 2-6). Finally, at a depth of 35 mm, the signal starts getting attenuated because of the path travelled in the sand (Figure 2-7), thus decreasing the contrast of the resulting image.

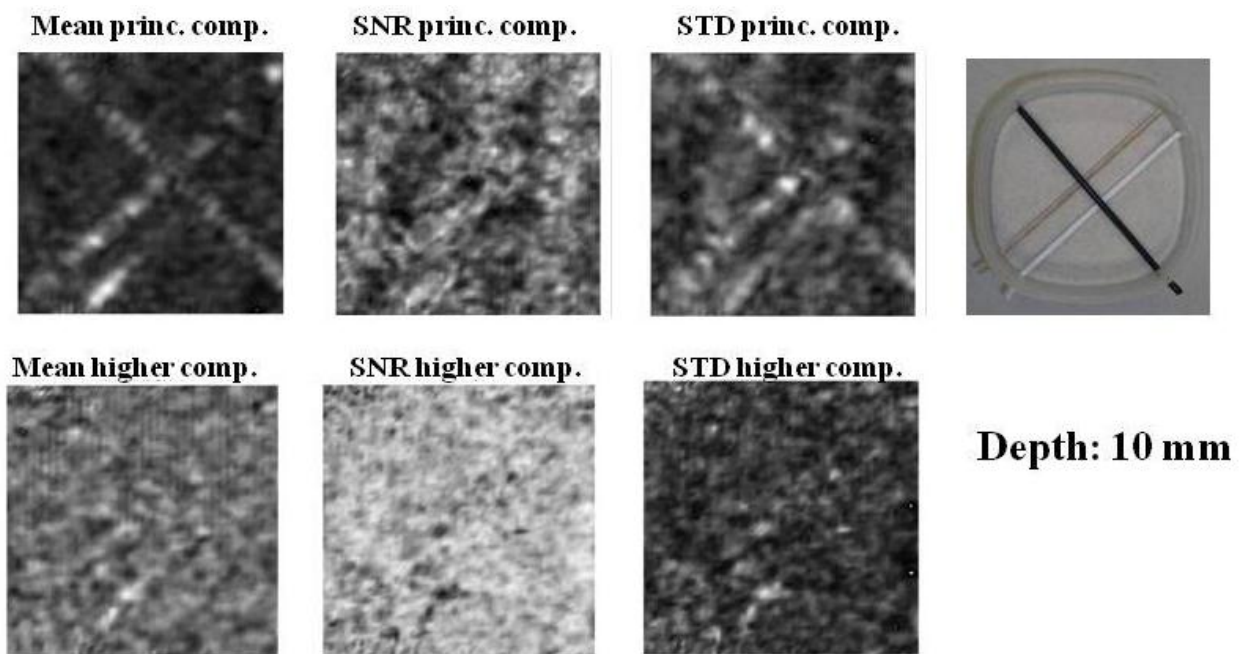


Figure 2-5. Cables buried at a depth of 10 mm.

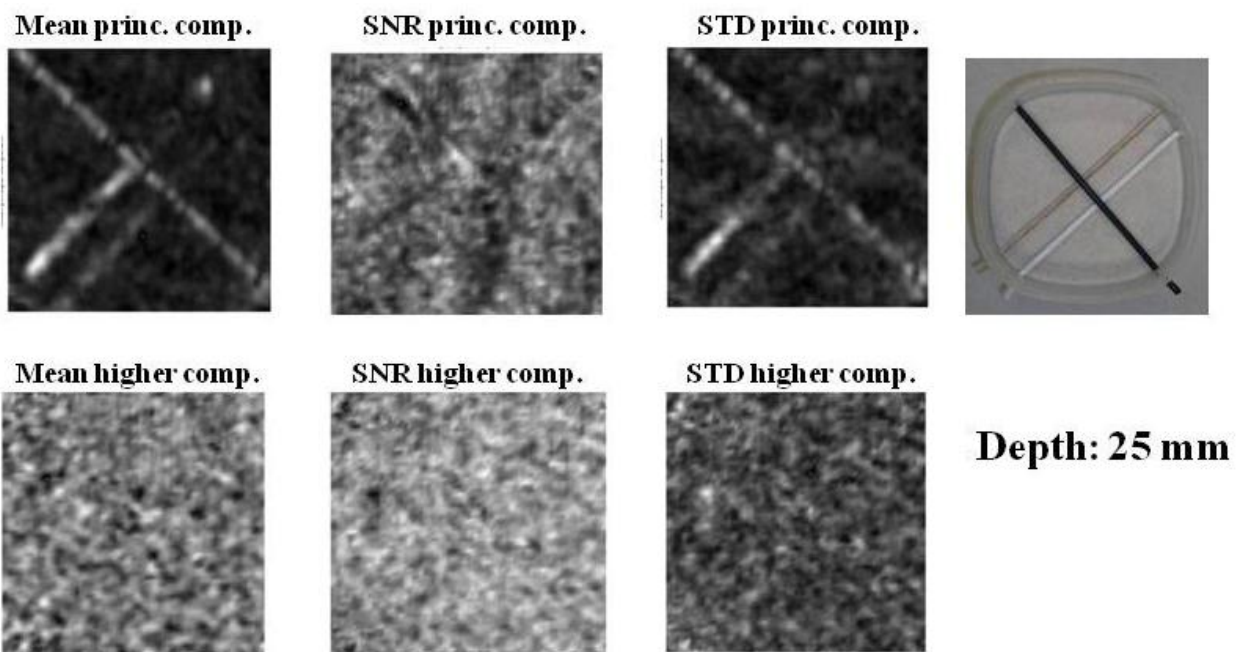


Figure 2-6. Cables buried at a depth of 25 mm.

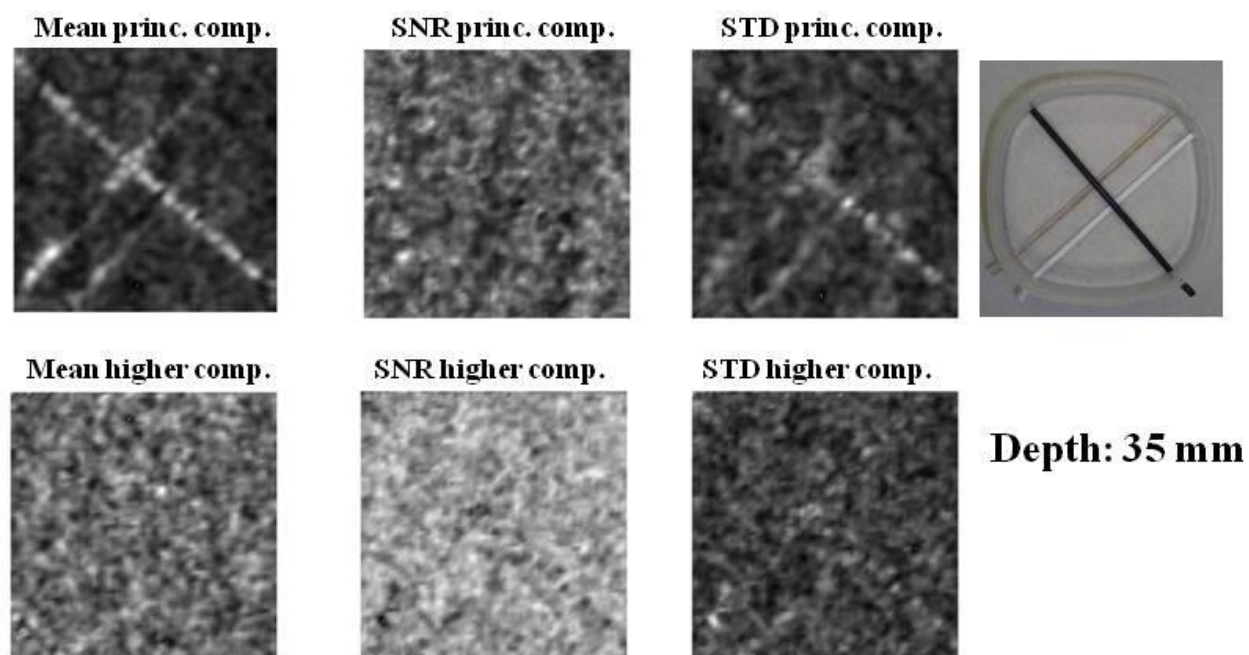


Figure 2-7. Cables buried at a depth of 35 mm.

2.2.3.2. Imaging through walls

Through-wall imaging can provide enhanced situation awareness in civilian and military scenarios. A through-wall imager can assist the process of information gathering and decision-making about the potential threats hidden behind walls or doors. The need for high penetration depth through construction materials requires that this type of imaging be performed using microwaves or longer wavelengths [14]. Millimeter waves, however, can still provide enough penetration through certain construction materials, which would provide significantly higher resolution compared to microwaves. Law-enforcement agents can take advantage of a through-wall imager for the detection and identification of weapons or drugs hidden behind closed doors. Relief efforts in case of man-made or natural disasters can also benefit of the increased awareness of objects behind common obscurants.

In this set of experiments, imaging through drywall, tiles, plywood, and hardboard was tested. The monostatic configuration was selected with a frequency span ranging from 90 to 140 GHz in 0.5 GHz steps for a total of 101 frames. TDR was used to reduce the reflection generated by the barrier. Principal component analysis was used to reduce the images from 101 frames to one frame, with the target situated at the focus. Table 2-1 describes the materials tested. Figure 2-8 shows the materials and the barriers through which the images were taken. In all cases, except for the image through drywall, TDR was used to enhance the images.

As the purpose of these experiments was only to determine the feasibility of imaging through the mentioned barriers, out of the set of six images generated using the principal components analysis, only what we considered the best image for each case is presented.

Table 2-1. Construction materials used for the through-wall imaging studies and their description.

Material	Description
Drywall	Layer of gypsum plaster cased in between two thick layers of paper.
Tiles	Ceramic with a hard glaze finish.
Plywood	Type of manufactured wood made of thin veneers or plies of softwood or hardwood. Used in substitution of regular wood for floors, walls, and roofs in house constructions.
Hardboard	Type of composite or man-made wood made of exploded wood fibers that have been highly compressed. Very homogeneous and with no grain.

In all cases, it is possible to detect and identify the target, as shown in Figure 2-8. The upper section shows imaging through a single layer of drywall. Because of the effects shown in Figure 2-3, this image was obtained without using TDR. Imaging through a single layer of tile is affected by the presence of a raised pattern on the back of the barrier. Compared to the other materials, imaging through plywood allows a clearer picture due to the decreased thickness and lower density. The image obtained through hardboard can be seen at the bottom of Figure 2-8. The rough side of the hardboard (not pictured) makes the optical path experimented by the waves to be nonuniform which translate to the image as noise.

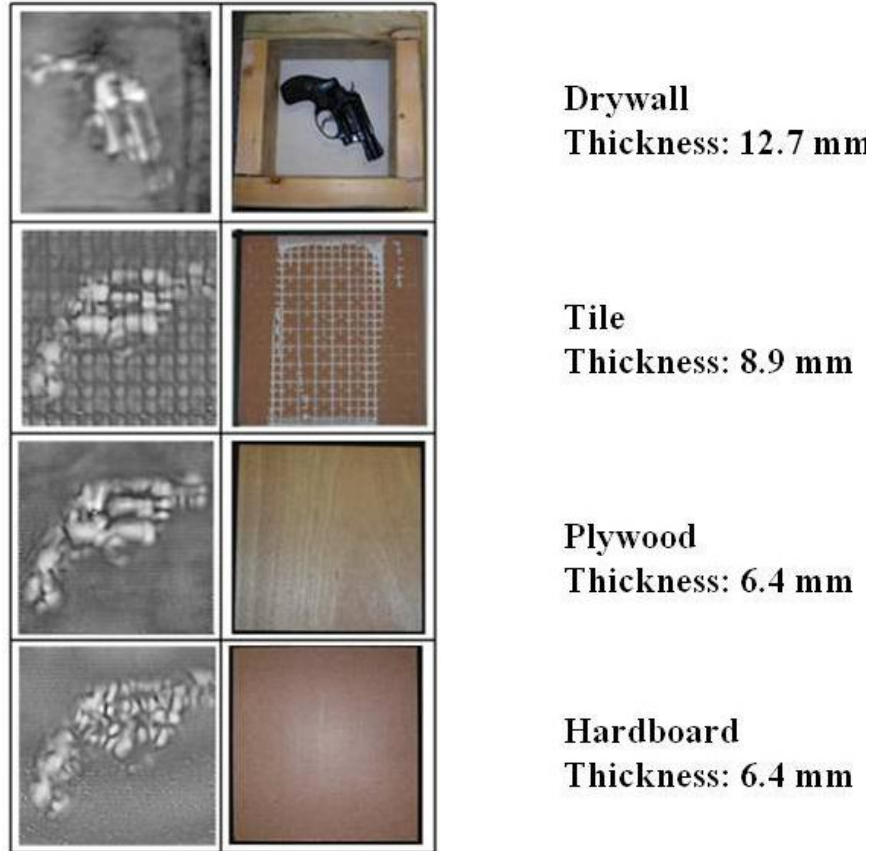


Figure 2-8. Results of imaging through drywall, ceramic tile, plywood and hardboard.

2.2.3.3. Imaging at increased distances

The process of imaging objects not situated immediately behind a barrier present a bigger challenge. According to the Rayleigh criterion of resolution, the minimum resolvable separation δ between two points depends on the wavelength of radiation λ , and the distance z between the object and the exit pupil D_{exit} :

$$\delta = \frac{\lambda \cdot z}{D_{exit}} \quad (2.1)$$

Taking the object from 100 mm to 300 mm from the exit pupil increases δ by a factor of 3, with visible effects on image quality. Figure 2-9 shows the same target at different standoff distances. At 300 mm, the object can be detected, but the small features are lost.

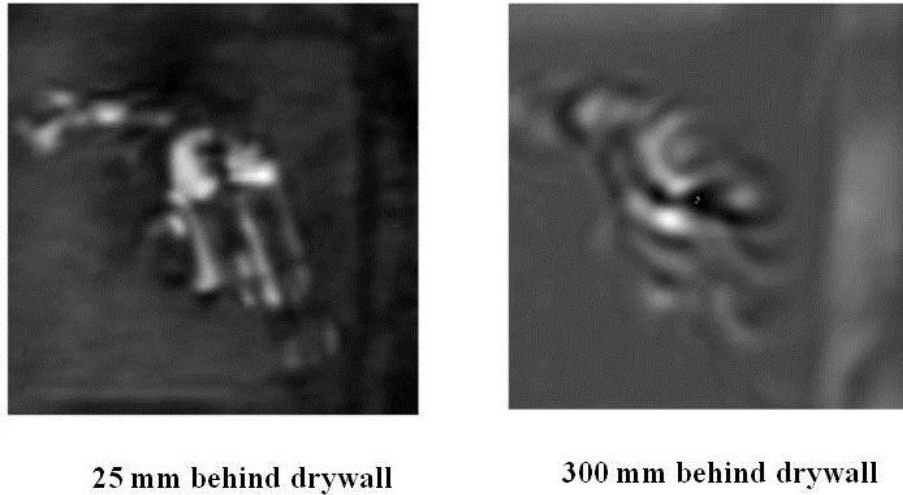


Figure 2-9. Comparison of image quality for 25 and 300 mm standoff distance for the active mmW imaging system.

2.3. Discussion

In this chapter we discussed various methods for subsurface detection of explosives. The advantages and disadvantages of each were weighed and concluded that active mmW scanning is the most suitable method for a high probability of detection of metallic and nonmetallic landmines. Time-domain reflectometry was used to apodize, through signal processing, the reflection from the barrier. We found that the SNR of the reflected signals increased, but that it

affects the minimum resolvable resolution as a consequence of signal saturation. Overall, TDR is a useful technique that can be used when the return signal is very low.

The raster-scan active mmW imaging system was built for the detection of buried landmines, but it was found to be capable of imaging different buried objects and through barriers besides soils. Electrical cables with thicknesses smaller than the theoretical diffraction limit were detected at different depths.

Motivated by the need to increase awareness of potentially threatening situations, we conducted studies to assess the suitability of millimeter-wave imaging for the identification and detection of objects behind four commonly used construction materials. The results show that a metallic target immediately behind drywall, a ceramic tile, plywood, and hardboard was detected and identified. Increasing the distance between the object and the imaging system increases the size of the minimum resolvable separation between two points, which translates to lower image quality.

Finally, we showed the limitations of a fixed-aperture raster-scan imager for relatively long standoff distances (at least 300 mm). The following chapter discusses how aperture synthesis techniques allow high image quality and increased standoff distances.

CHAPTER 3: FOUNDATIONS OF APERTURE SYNTHESIS

Aperture synthesis is the process through which a large aperture is effectively replicated using a thinned array of detectors with smaller area and volume. Aperture synthesis departs from traditional imaging techniques where an increase in image resolution comes at the expense of bulkier, larger, and heavier systems.

Interferometric techniques in astronomy are based on the early works of Michelson and Pease, who were able to achieve angular resolutions capable of measuring the diameters of some of the nearer and larger stars. Beams of light falling on the apertures are combined in a telescope where interference fringes are observed according to the separation of the apertures and the separation of the sources. If the angular width of the sources is small compared with the adjacent peaks in the fringe pattern, then the sources are said not to be resolved. If, on the other hand, the angular separation of the sources is comparable to the spacing, then the fringes will be formed by a superposition of images from a series of points. In that case, the fringe amplitude decreases. The measure of the amplitude of the fringes is called the fringe visibility, V_M , and is given by equation (3.1)

$$V_M = \frac{\text{intensity of maxima} - \text{intensity of minima}}{\text{intensity of maxima} + \text{intensity of minima}} \quad (3.1)$$

This parameter, V_M , is important because the fringe visibility is proportional to the modulus of the Fourier transform of the intensity distribution. Every point of the visibility function is an independent frequency component [8].

Interferometric techniques are independent of wavelength, making aperture synthesis techniques useful for RF, microwave, and mmW imaging. Observation of faint distant celestial bodies was difficult in the visible, mostly because of atmospheric turbulence. Furthermore, analysis of RF radiation provides information that cannot be detected by optical telescopes. By the mid-twentieth century, several successful attempts had been completed where two-element radio interferometers were used for the observation of stars. By the 1970s, very long baseline interferometers (VLBI) were making measurements with detectors thousands of kilometers apart and taking advantage of the rotation of the Earth to multiply by several orders of magnitude the maximum baselines that had been obtained a few decades earlier.

3.1. The two-element interferometer

The basic component of a synthesized aperture is a two-element interferometer [15]. It can be proven that the correlation of the signals impinging on the apertures provides a frequency component of the spatial Fourier spectrum. To extract any useful information of the properties of the incident radiation, it is necessary to understand the properties of the radiation itself and those of the receiving system.

3.1.1. The incident radiation

The electric fields to be measured are a function time and the direction of arrival. Because interferometry was originally intended for astronomy, this section of the chapter considers only sources in the far field. Intensity distributions at a distance with the same order of magnitude as the collecting aperture are discussed in later sections of this chapter. As a consequence, it is understood that radiation comes in the form of plane waves. The basic configuration of a two-element interferometer is shown in Figure 3-1. In its simplest form, it consists of two antennas (or apertures), transmission lines, a correlator, and an integrator. Also included, is the geometry of radiation coming from an angle θ with respect to the normal to the plane of observation, and with detectors separated a distance D_{int} , also called the baseline. The fields impinging on the detectors are represented by:

$$\begin{aligned} E_1(t) &= A \cdot \sin(2\pi\nu t) \\ E_2(t) &= B \cdot \sin(2\pi\nu(t - \tau_g)) \end{aligned} \tag{3.2}$$

Where E_1 and E_2 are the fields seen by detectors 1 and 2, respectively, ν is the frequency of radiation and τ_g is the geometric path difference between both signals. As this is the case of plane wave radiation, the magnitudes A and B have the same value and can, therefore, be omitted from the analysis.

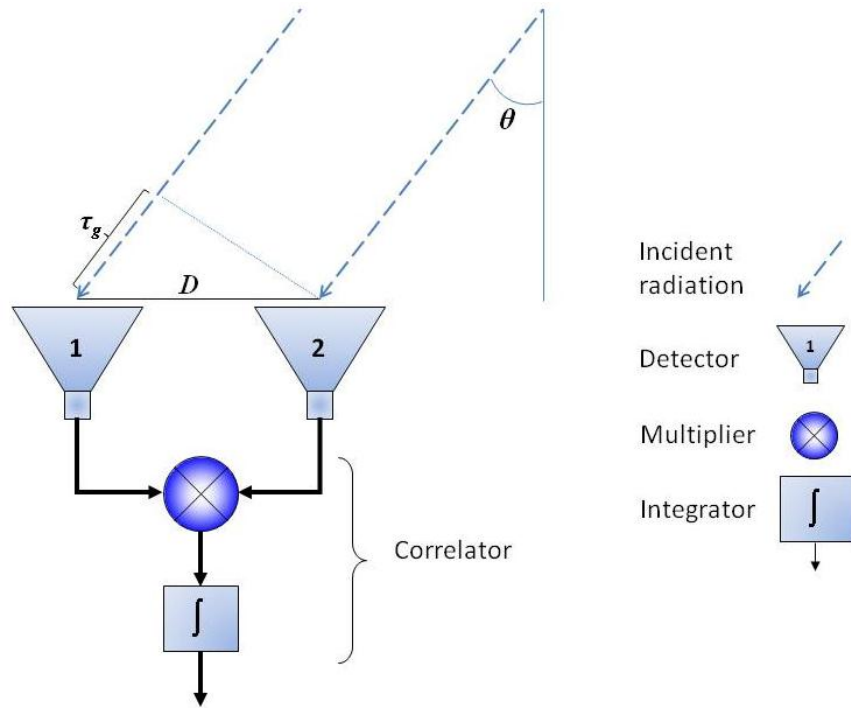


Figure 3-1. Geometry of a two-element interferometer.

3.1.1.1. The fringe pattern function

The result of correlating E_1 and E_2 , that is, multiplication and time integration, is called the fringe pattern. The fringe pattern F is a function that describes the amplitude of the correlation of the signals and depends on the angular position of the source. The fringe pattern is defined by equation (3.3) below:

$$F = 2 \sin(2\pi\nu t) \cdot \sin(2\pi\nu(t - \tau_g)) \quad (3.3)$$

The added factor of two is a constant included to simplify calculations and does not affect the shape of F . After some mathematical manipulation, F can be represented as the difference of one slowly varying cosine function dependent on the path differences and the frequency of radiation, and a cosine function with twice the radiation frequency and a phase term, as seen in equation (3.4).

$$F = \cos(2\pi\nu\tau_g) - \cos(4\pi\nu t - 2\pi\nu\tau_g) \quad (3.4)$$

Under usual circumstances, the higher frequency component is filtered out either by electronic components, filters or simple time averaging and can be omitted. Given that $\nu = c/\lambda$ and that $\tau_g = D_{int} \cdot \sin(\theta)$, the fringe pattern can be represented as a function of the incoming signals direction of arrival:

$$F = \cos(2\pi\nu\tau_g) = \cos\left(2\pi \frac{D_{int}}{\lambda} \cdot l\right) \quad (3.5)$$

Where $l = \sin(\theta)$ is the term used to represent the direction of the incoming radiation.

3.1.1.2. One-dimensional antenna synthesis

The information obtained from the correlated beams is contained in the phase delay term τ_g ; therefore, by individually controlling the phase delay of the antennas, multiple detectors can

track a source at any angular location. To track a source at an angle θ_o implies defining the phase difference between each detector as zero for radiation coming from this direction. In other words, the geometric delay τ_g and the instrumental delay τ_i are set to be equal. In mathematical form, a zero phase delay can be expressed as: $\tau = \tau_{g|\theta=\theta_o} - \tau_i = 0$, where $\tau_{g|\theta=\theta_o} = (D_{\text{int}}/c) \cdot \sin(\theta_o)$. For a source with angular width equal to $2\Delta\theta$, where $\Delta\theta$ is small enough to allow small angle approximation, the fringe response term for radiation coming from the direction $\theta_o - \Delta\theta$ is given by:

$$\cos(2\pi\nu_o\tau) = \cos\left\{2\pi\nu_o\left[\frac{D_{\text{int}}}{c}\sin(\theta_o - \Delta\theta) - \tau_i\right]\right\} \quad (3.6)$$

Equation (3.6) can further be simplified to:

$$F(l_o) = \cos(2\pi\nu_o\tau) = \cos(2\pi ul_o) \quad (3.7)$$

Where $l_o = \sin(\Delta\theta_o)$ and

$$u = \frac{D_{\text{int}} \cos(\theta_o)}{\lambda} \quad (3.8)$$

The term u is the projection of the baseline onto a plane normal to the direction of the source. This quantity is interpreted as spatial frequency and is measured in units of cycles per radian. Hence, the fringe pattern for a source at an angle θ , is dependent on u .

3.1.2. Response of the receiving system to the incident radiation

To obtain the fringe pattern function, we must analyze other parameters of the receiving system that affect F . These parameters are the bandwidth passband function and the radiation pattern of the antennas. The bandwidth function, $F_B(\nu)$, describes the response of the interferometer as a function of frequency. For the case of a source with constant amplitude across the spectrum, the bandwidth function modifies the fringe pattern by a factor equal to the Fourier transform of F_B [8] [15], that is:

$$F = \cos(2\pi\nu\tau) \cdot \mathbb{F}\{F_B(\nu)\} \quad (3.9)$$

Where $\mathbb{F}\{F_B(\nu)\}$ represents the Fourier transform of $F_B(\nu)$. The modulating function $F_B(\nu)$ is usually an undesired effect and its envelope effect is solved by measuring at its peak value. For the case of monochromatic or quasi-monochromatic sources, the bandwidth function can be replaced by a constant.

3.1.2.1. Interferometer response as a convolution

Next in the description of the response of the interferometer is the effect of the antennas that constitute the observing apertures. The output power of a single antenna is a function of its radiation pattern, $A(\theta)$, and the intensity distribution $I(\theta')$. See equation (3.10). θ is measured with respect to the center of the radiation pattern, and θ' with respect to the nominal position of the source (see Figure 3-2).

$$P(\theta) = \int_{\text{source}} A(\theta - \theta') I(\theta') d\theta' \quad (3.10)$$

Equation (3.10) is the cross-correlation of the radiation pattern and the intensity distribution.

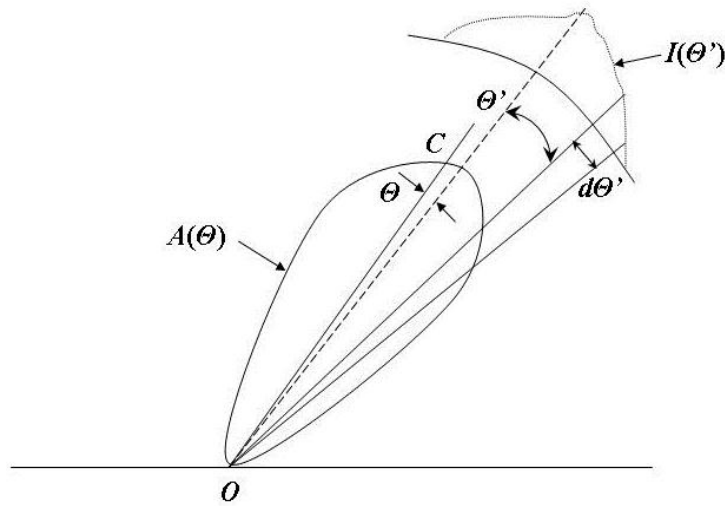


Figure 3-2. Antenna radiation pattern and intensity profile of source.

In the same way, the interferometer can be considered as a system with an output equal to $G(l')$, where $G(l')$ includes the product of the fringe pattern ($\cos(2\pi ul')$), the bandwidth function

$(F_B(l'))$, and the antenna pattern $(A(l'))$. Thus, the response of the interferometer to an intensity distribution $I_I(l')$ can be obtained by performing the cross-correlation of $I_I(l')$ and $G(l')$, as

$$R(l) = \int_{source} \underbrace{\cos(2\pi u(l-l')) \cdot A(l') \cdot F_B(l')}_{G(l-l')} \cdot I_I(l') \cdot dl' \quad (3.11)$$

This can also be expressed as:

$$R(l) = \cos(2\pi ul) * [A(l) \cdot F_B(l) \cdot I_I(l)] \quad (3.12)$$

Where the asterisk symbol (*) represents the convolution operation. The antenna pattern and bandwidth functions are constant factors depending only on the system's characteristics. In this case, equation (3.12) is proportional to:

$$R(l) = \cos(2\pi ul) * I_I(l) \quad (3.13)$$

3.2. Convolution theorem and spatial frequency

Convolution can be treated as a multiplication of the Fourier transforms of the convolved functions, thus equation (3.13) leads to:

$$\vec{r}(u) = \frac{1}{2} [\delta(u - u_o) + \delta(u + u_o)] \cdot \vec{V}(u) \quad (3.14)$$

Where $\vec{r}(u) \rightleftharpoons R(l)$ and $\vec{V}(u) \rightleftharpoons I_1(l)$ are Fourier transform pairs. $\vec{V}(u)$ is also called the *visibility* function. Simplifying equation (3.14) we obtain:

$$\vec{r}(u) = \frac{1}{2} \left[\vec{V}(-u_o) \cdot \delta(u + u_o) + \vec{V}(u_o) \cdot \delta(u - u_o) \right] \quad (3.15)$$

Equation (3.15) means that the interferometer acts as a filter that responds only to spatial frequencies $\pm u_o$, therefore, an approximation of the original intensity distribution can be reconstructed if enough spatial frequencies are measured.

3.3. Two-dimensional synthesis

The synthesis of a source in two dimensions requires sampling the spatial frequency spectrum in two dimensions. As in the case of one-dimensional synthesis, there is no measurement of the range of the source and only the direction of the incoming radiation can be determined. This direction is given by the term l . In two-dimensional measurements, a second quantity must be included, namely m , thus any point in the plane of observation is given by the two direction cosines (l, m) . The spatial frequency associated with the direction cosine m is defined as v , and is obtained using the same principles as the frequency u , associated to the direction cosine l . Thus, the analog to the (l, m) plane in the frequency domain is the (u, v) plane.

The maximum field of view for detectors is a full hemisphere; however, the reconstructed image is not an exact replica of the source, but its projection onto a unit circle. Each point inside this unit circle contains the values of the direction cosines (l,m) that point to a specific direction in space. Figure 3-3 shows the representation of the (l,m) plane and the projection of an extended source onto the unit circle.

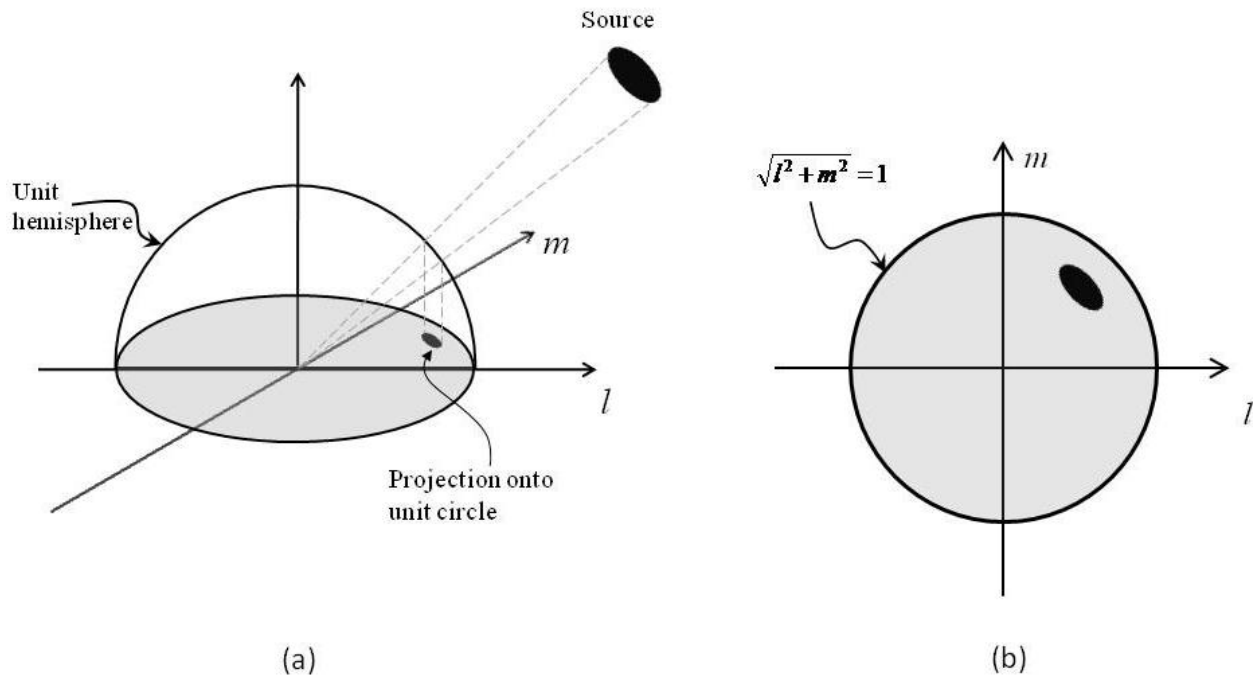


Figure 3-3. The (l,m) plane and the unit circle.

For points close to the center of the (l,m) , the reconstructed image is proportional to the mapped source. However, points mapped in direction cosine space present increased distortions as l and m approach unity. This can be corrected by projecting such points onto a plane parallel to the plane of observation.

3.4. Effects of coherence

The spatial coherence of the intensity distribution affects the relationships derived to obtain spatial frequencies. Although different in the way the principles work, both fully coherent and fully incoherent sources can be resolved with similar arrangements of antenna spacings for a given angular size [8, 16, 17]. Understanding of coherent and incoherent cases is important for the different applications where aperture synthesis can be applied. Passive sources are considered spatially incoherent, whereas in a system with active monochromatic illumination the targets are scatterers strongly correlated with each other, as each point reacts to the same source. Thompson et. al. describe the equations for the coherent case by visualizing the intensity distribution as an aperture illuminated with fully coherent radiation. Figure 3-4 describes the geometry of a source, or aperture illuminated with a coherent source, and two observation points P_1 and P_2 .

The aperture plane (X,Y) is considered to be in the far field and R_1 and R_2 are the distances from the source, located in direction (l,m) , and P_1 and P_2 , respectively. In this exercise, P_2 is defined as the reference point where the maximum strength occurs and is located at the origin of coordinates of the (x,y) plane. The distance between the (X,Y) plane and the (x,y) plane is large enough that, except for the phase terms, R_1 and R_2 can be approximated to R . The source is illuminated by an electromagnetic field with amplitude $\varepsilon(l,m,t)$. The path difference $R_2 - R_1$ is given by $lx + my$ and can be calculated using triangulation. Under these assumptions, the field at P_1 is given by:

$$E_1(l, m, t) = \frac{e^{-j2\pi\nu(t-R/c)}}{R} \varepsilon\left(l, m, t - \frac{R}{c}\right) e^{-j2\pi\nu \frac{(lx+ym)}{c}} \quad (3.16)$$

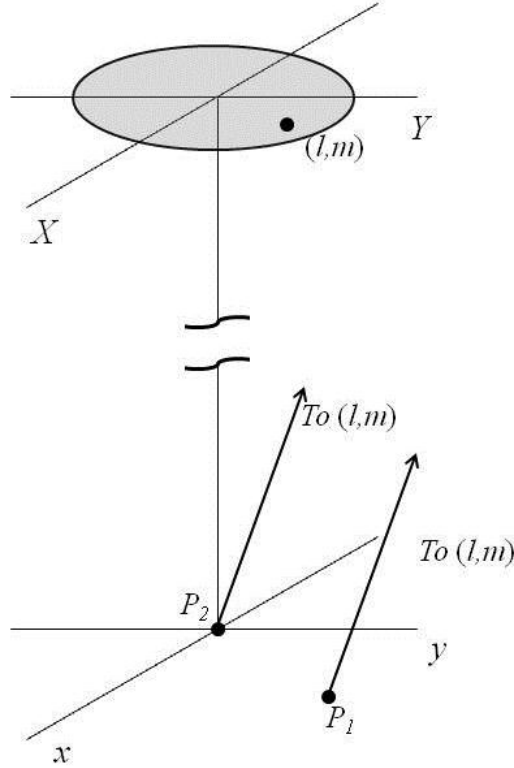


Figure 3-4. Geometry of a distant coherent source and observation points P_1 and P_2 .

The total field at the observation point P_1 can be obtained integrating over the whole aperture, as per equation (3.17). The area element ds is proportional to $dl \cdot dm$ and the term outside the integral is an envelope accounting for the variation in amplitude and phase due to propagation from the source.

$$E(x, y) = \frac{e^{-j2\pi\nu(t-R/c)}}{R} \int_{\text{aperture}} \varepsilon\left(l, m, t - \frac{R}{c}\right) e^{-j2\pi[(x/\lambda)l + (y/\lambda)m]} ds \quad (3.17)$$

Expressing the time dependent functions $E(x,y)$ and $\varepsilon(l,m,t)$ with their rms values, denoted by \overline{E} and $\overline{\varepsilon}$, respectively, leads to equation (3.18):

$$\overline{E}(x,y) \propto \iint_{\text{aperture}} \overline{\varepsilon}(l,m) e^{-j2\pi\left[\left(\frac{x}{\lambda}\right)l + \left(\frac{y}{\lambda}\right)m\right]} \cdot dl \cdot dm \quad (3.18)$$

The propagation factor has been omitted and a proportionality sign, instead of an equality sign, is used. Equation (3.18) was obtained under the assumption that radiation is only being emitted from the aperture; therefore, the integration limits can be expanded to $\pm\infty$ and the equation is equivalent to a Fourier transform. This Fourier transform relationship between the field distribution $E(x,y)$ plane and the electromagnetic field amplitude $\varepsilon(l,m,t)$ is analogous to the van Cittert-Zernike theorem. The van Cittert-Zernike theorem states that the mutual coherence function, which is equivalent to the visibility function, is equal to the Fourier transform of the intensity distribution, that is:

$$\Gamma(u,v,0) = \iint_{\text{source}} I(l,m) e^{-j2\pi(ul+vm)} dl \cdot dm \quad (3.19)$$

Though equations (3.18) and (3.19) are analogous and arrive to similar conclusions, it is important to emphasize that both describe different situations. Equation (3.18) describes the case of a source with full spatial coherence, whereas in equation (3.19) all the points in the source are uncorrelated with each other.

3.5. Numerical focusing

Digital post processing allows calculations that are not possible with real-time imaging. Among these advantages we count the optical concept of focusing. Focusing is needed as the image reconstruction algorithm analyzed in the earlier sections of this chapter is limited to far field objects. Focusing is a critical issue as the purpose of this research is to image items that are at a distance comparable in size to the collecting aperture.

3.5.1. Near-field and far-field measurements

The first item we look into the focusing sub-section is the difference between near-field and far-field radiation. Far-field radiation can be approximated as a plane wave, that is, waves have the same amplitude throughout the plane of observation, and the same phase in a plane perpendicular to the direction of the incoming radiation. For a synthesized aperture that uses Fourier inversion for image reconstruction, the radiation received must be a plane wave. Far fields and near fields are defined in terms of the ratios of the diameter of the collecting aperture D and the wavelength of the radiation. In a given system, the distance S that is considered to be in the far field is given by equation (3.16) [18]:

$$S = \frac{D^2}{4\lambda} \quad (3.20)$$

For the designed test bed, with a maximum collecting aperture of 900 mm, and wavelength of radiation $\lambda = 3$ mm, the far field is approximately 67 m. This distance is prohibitive given the available resources; therefore, a modified image reconstruction algorithm must be developed.

If we let $\mathbf{U}(x,y;0)$ be a field distribution at $z = 0$; and $\mathbf{U}(x,y;z_1)$ be the field distribution at $z = z_1$; then our task consists on computing $\mathbf{U}(x,y;0)$ after measuring $\mathbf{U}(x,y;z_1)$. For sources in the far field and very close to the optical axis, imaging using aperture synthesis is straightforward:

$$F_{\mathbf{U}(x,y;0)}(u,v;0) \approx F_{\mathbf{U}(x',y';z_1)}(u,v;z_1) \quad (3.21)$$

$$\mathbf{U}(x,y;0) = \mathbb{F}^{-1}\{F(u,v;0)\} \approx \mathbb{F}^{-1}\{F(u,v;z_1)\} \quad (3.22)$$

Where $F_{\mathbf{U}(x,y;0)}(u,v;0)$ is the Fourier transform of $\mathbf{U}(x,y;0)$ and \mathbb{F} is the Fourier transform operator. In other words, if fields can be measured across the plane of observation, then the fields that produced them can be reconstructed from the measured ones. This reconstruction is possible as long as the radiation comes from the far field and is close to the optical axis. See Figure 3-5 for an illustration describing the situation.

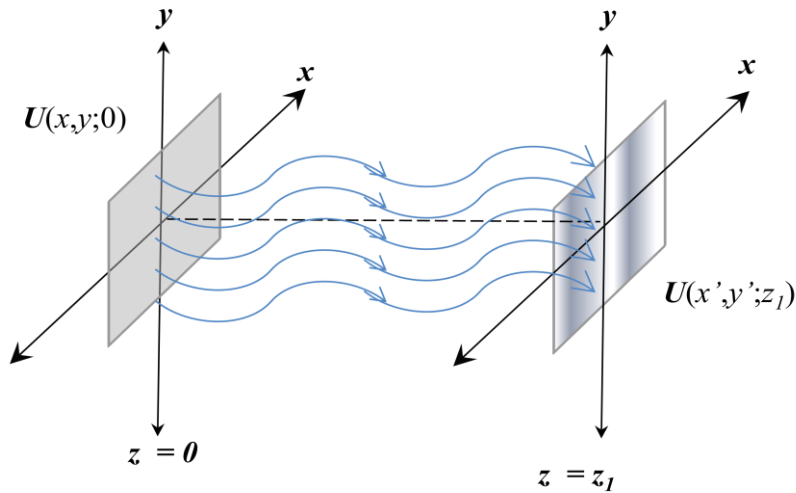


Figure 3-5. Plane waves travelling from the plane $z = 0$ to the plane $z = z_1$.

3.5.2. Phase front correction

When illuminating the targets with an active source, each point can be considered as a scatterer that generates spherical waves from its location, creating, therefore, a spherical phase front. In optics, spherical phase fronts can be made parallel by a process called collimation. Collimation virtually locates the position of the source at infinity. This is usually achieved by placing the source at the focal point of a thin lens. Under these conditions, the thin lens simply acts as a phase corrector [7, 19]. Therefore, the task of obtaining a plane wave can be achieved by determining the distance between the section of a sphere and a tangential plane. See Figure 3-6.

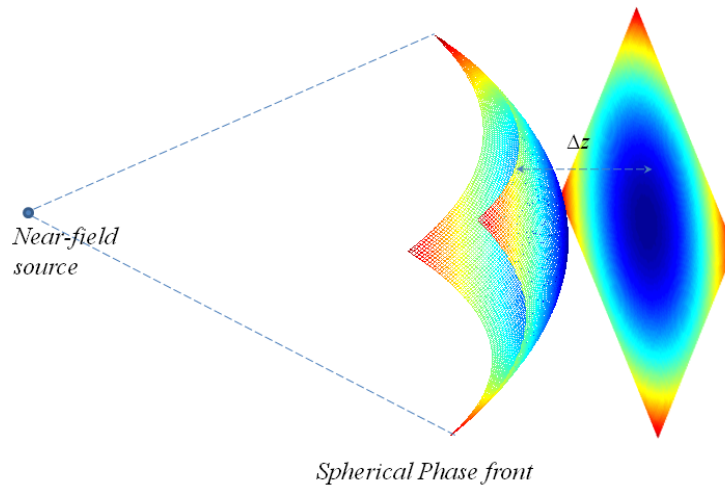


Figure 3-6. Spherical phase front and a tangential plane.

The same approach can be used to correct the measured field distribution $U(x',y';z_I)$ so that it looks like the intensity distribution $U(x',y';z_I)$ is located at infinity. The primed characters refer to the plane of observation.

If the source coordinates are known (x,y,z) for a source located in the x - y plane), the phase difference $\Delta\Phi$, due to an optical path difference Δz , can be added to the spherical phase front so it becomes a plane wave. Common algorithms for image reconstruction can now be used.

This simulated lens, or phase correcting element, can be represented by multiplying the following expression to the measured fields in the $(x',y';z_l)$ plane. If we let $\Delta\Phi(x,y)$ be the amount of phase correction needed in the point (x,y) , then $\Delta\Phi(x,y)$ can be calculated with the expression given in equation (3.4):

$$\Delta\Phi(x', y') = e^{i \cdot k \cdot \Delta z(x', y')} \quad (3.23)$$

Where

$$k = \frac{2\pi}{\lambda} \quad (3.24)$$

$$\Delta z = \sqrt{(x - x')^2 + (y - y')^2 + z^2} - z_l \quad (3.25)$$

And the focal point is located at (x,y,z) . By appropriately choosing (x,y,z) a focus on any point in space could be obtained.

CHAPTER 4: SPARSE APERTURE MILLIMETER-WAVE IMAGING SYSTEM

An active millimeter-wave imaging system for seeing through barriers was designed, built, and tested, based on the principles stated in the first three chapters. Commercial off-the-shelf mechanical and electrical components were preferred for their quick availability and cost effectiveness, compared to custom or developed in-house components. Besides commercial availability of components, full automation and compact size were given a high priority in the design and development of this test bed.

The test bed was designed to achieve the following requirements: provide active illumination, subwavelength accuracy (for mechanical components), capable of coherent detection, and full automation. As such, the system can be envisioned as an assembly of four independent stages, each meeting one of the above-mentioned requirements. Below, we explain and discuss the criteria considered for each block.

4.1. Active source

The frequency of operation is 94 GHz ($\lambda = 3.19$ mm). This frequency was selected to give enough resolution for object identification and enough depth of penetration. Because of the waves' low atmospheric attenuation at 94 GHz, devices operating at this frequency are used in many applications and several manufacturers deliver sources and detectors with short lead times. A Gunn oscillator provides an output of 17 dBm and is fed to a high power amplifier. The high power amplifier operates at a center frequency of 94 GHz. The maximum output of this amplifier

is ~24 dBm (~250 mW). The output of the amplifier is channeled to the center of the platform using a custom-made rigid waveguide. All connections are made using WR-10 waveguides, the industry standard for frequencies between 75 – 110 GHz. A square horn antenna, with 24° beamwidth directs the radiation in the forward direction.

4.2. Scanning

Proper two-dimensional reconstruction of images requires two-dimensional scanning. To achieve scanning with multiple detectors a polar coordinate approach was used. Linearly translating arms were mounted on a rotary stage, with up to 6 arms available for detector displacement. Angular control was achieved using an IntelLiDrives computer-controlled rotary stage with a maximum resolution of 1,080,000 steps per revolution (~5.8 μ rad). Linear motion was achieved using linear actuators with 400 mm longest piston extension. The piston extension of the linear actuators is controlled using a stepper motor with a resolution of 24,000 steps per inch (~945 steps per mm).

The detector location accuracy is given by the angular step size in radians multiplied by the longest arm extension. The longest radial extension of the arms, from the center of the test bed, is 450 mm, including 50 mm offset. In practice, the rotary stage had a margin of error of approximately 300 steps (~1.7 mrad), and the linear actuators had an error of approximately 50 steps (~53 μ m) between measurements. Under these circumstances detectors can be positioned with accuracy better than:

$$300 \text{ steps} \times \left(5.8 \times 10^{-6} \frac{\text{rad}}{\text{steps}} \right) \times 445 \text{ mm} + 0.053 \text{ mm} = 0.829 \text{ mm} \quad (4.1)$$

Thus, better than $\frac{1}{4}$ wavelength accuracy can be attained for all arm extensions shorter than the maximum of 400 mm.

The hardware used for control of the rotary stage is an Xenus ® step controller, interfaced with the computer through a DB-9 serial port in the computer. The linear actuators were controlled using a three step connection: a motion controller card connected to a breakout box, which in turn is connected to a stepper motor driver. The motion controller used was a NI-7330 internal PCI card from National Instruments ®, which generates steps as dictated by the software. Second, a breakout box, the UMI-7760 interfaces the computer and the stepper motor drivers. Finally, Gecko ® GV 203 stepper motor drivers generate the pulses that feed the stepper motor driving the piston extension of the linear actuators. The stepper motor drivers interface the 24 V_{DC} power supply and the breakout box. See Figure 4-1. The physical layout of the electrical and mechanical components is shown in Figure 4-2 (top view) and in Figure 4-3 (side view).

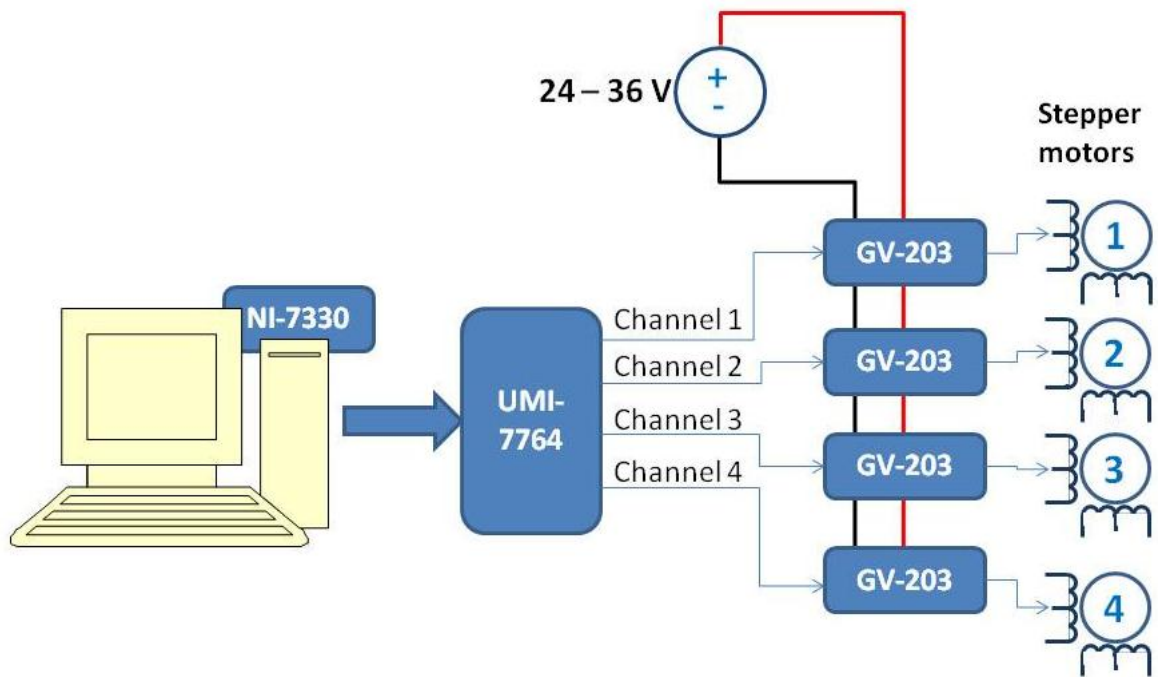


Figure 4-1. Stepper motor control schematic



Figure 4-2. Electrical and mechanical components of test bed. Circular plate and 6 linear translation arms (top view)

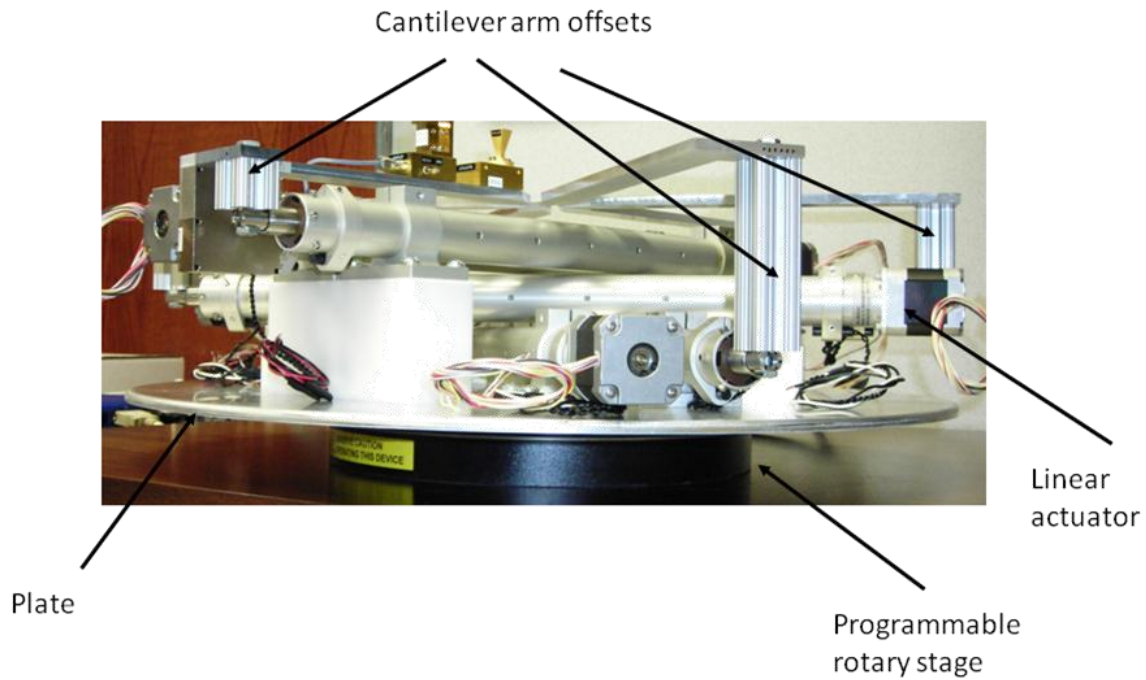


Figure 4-3. Test bed mounted on programmable rotary stage. Cantilever arm offsets place detectors on the same plane.

4.3. Coherent detection using digital methods

The coherent detection stage of the test bed consists of an analog mixing section and a digital processing section. In the analog mixing section, signals are down converted from 94 GHz to 20 MHz. In the digital section, magnitude and phase of the incoming signal are measured with respect to the reference. The analog portion of this system is illustrated in Figure 4-4.

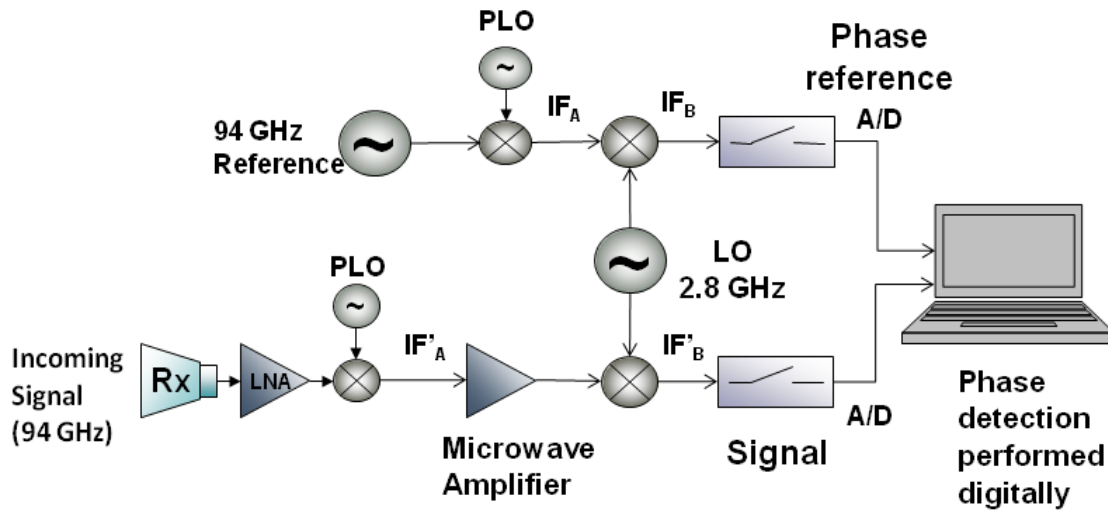


Figure 4-4. Schematic diagram of analog down conversion stage.

The system described by Figure 4-4 comprises the signal and reference branches. The upper part of the diagram is the reference branch. The reference branch consists of a 94 GHz Gunn diode connected to a power splitter. Half the power goes to an amplification stage, providing the signal for the illuminating source (not shown in the diagram). The other half goes to a W-band balanced mixer, where the signal is mixed with a phase locked 91.28 GHz local oscillator (PLO). The balanced mixer's output (IF_A) connector type and cable selection work as a low pass filter, thus making IF_A equal to 2.78 GHz. IF_A is then down converted to a second intermediate frequency of about 20 MHz (IF_B) using a microwave mixer and a second local oscillator operating at 2.8 GHz (LO).

The signal section of the detector follows a similar path. The incoming radiation at 94 GHz is captured by a W-band horn antenna, aligned with the source to avoid cross-polarization. The antenna's output is taken to a 92 – 96 GHz low noise amplifier (LNA) with 15 dB minimum gain

and a 6 dB noise figure. The band limit of the LNA also works as a filter for the incoming signal. A second PLO working at 91.22 GHz down converts the signal to 2.78 GHz (IF'_A). A microwave amplifier boosts IF'_A 15 dB. The output of this second amplifier, IF'_B , is mixed with the LO signal using a microwave frequency mixer. The frequencies of IF'_A and IF'_B are the same as IF_A and IF_B , respectively. Following the down conversion process, the signals IF_B and IF'_B are digitized and the relative phase delays are calculated using digital methods. These methods are explained in chapter 6.

The core of the digital section is a NI-5124 digitizer. The digitizer has two channels, with a maximum vertical resolution of 12 bits at 200 mV_{pp}, and a fastest sampling rate of 200 MS/sec. It is controlled through a graphic user interface written using LabVIEW. Offline computations are performed using MATLAB®.

4.4. Automation

The test bed design allows full automation of scans. Once the input parameters are assigned the system locates the detectors, samples the signals and saves them to the computer. See Figure 4-5 for the flow chart. After finishing the scan, MATLAB ® scripts reconstruct the images from the measured values. A flowchart of the reconstruction algorithm is shown in Figure 4-6.

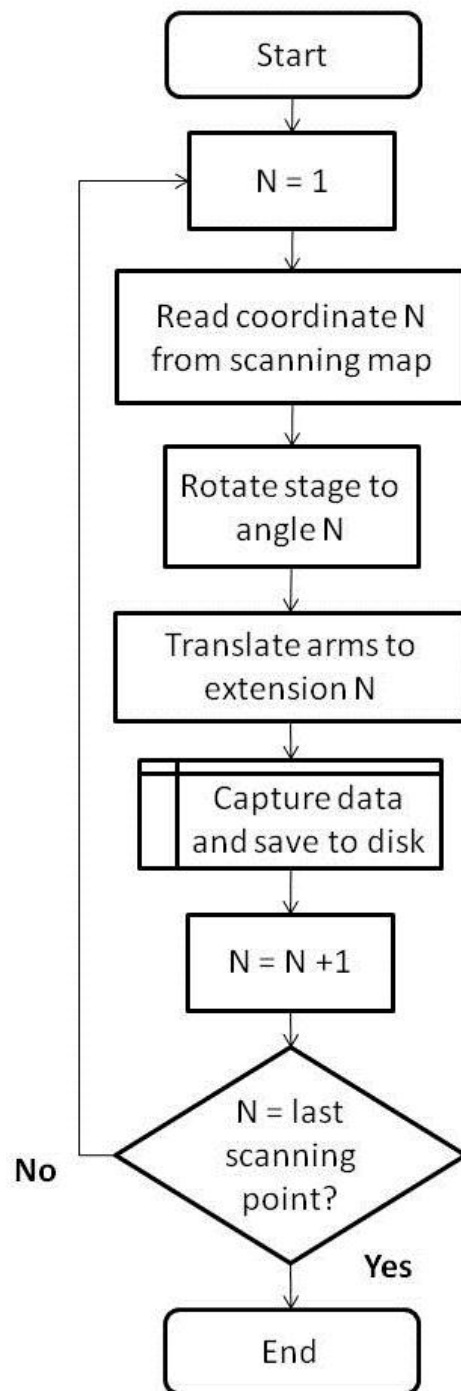


Figure 4-5. Scanning algorithm flowchart

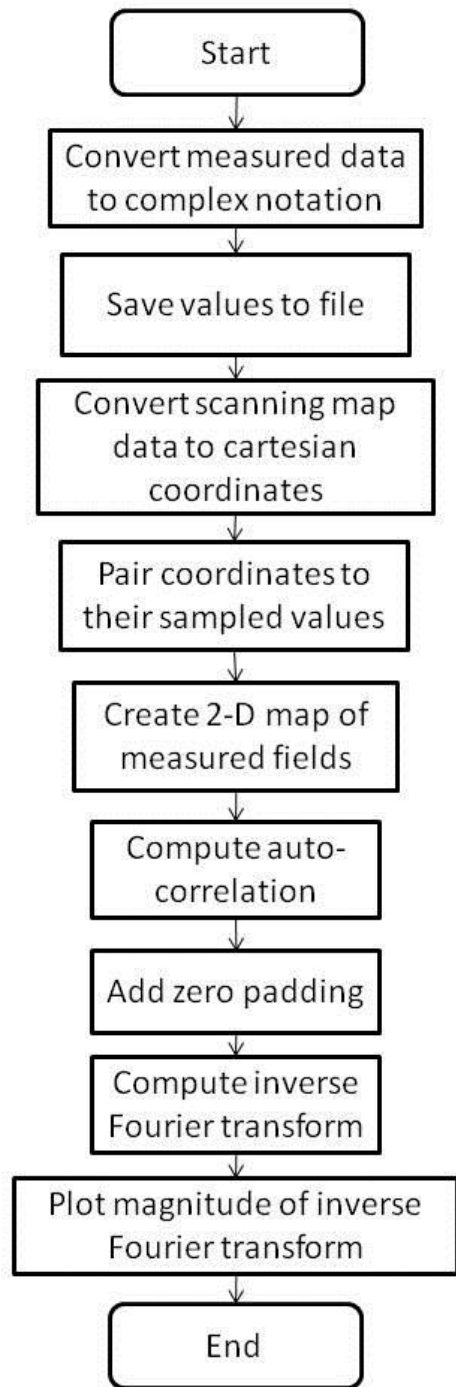


Figure 4-6. Image reconstruction flowchart.

CHAPTER 5: DIGITAL COHERENT DETECTION

The synthesis of an aperture requires coherent detection of the incoming signals. Coherent detection of millimeter waves is achieved by either up or down-conversion of the measured signals. Up-conversion of mmW signals to optical signals is achieved by mixing mmW with an optical laser and coupling this signal to an optical fiber. The phase information is preserved throughout the entirety of the transmission line and each point is at an analogous position in front of a lens. The Fourier transform is performed by this lens [10]. This approach benefits from the speed of processing provided by the lens, but lacks in versatility as the detectors are fixed and only a single configuration is possible. Down-conversion techniques are based on heterodyne detection and rely on transporting the phase information to a lower frequency. Among the advantages of down-conversion are the ease for guiding these waves using coaxial cables and the possibility of digital sampling.

5.1. Current methods for phase measurement

Demodulation for phase measurement can be achieved following one of two possible approaches, namely, using digital or analog demodulators. Analog demodulators are usually the preferred method because of their availability at wide frequency ranges, bandwidths, cost, and speed of operation. The principle of operation of these devices is illustrated in Figure 5-1.

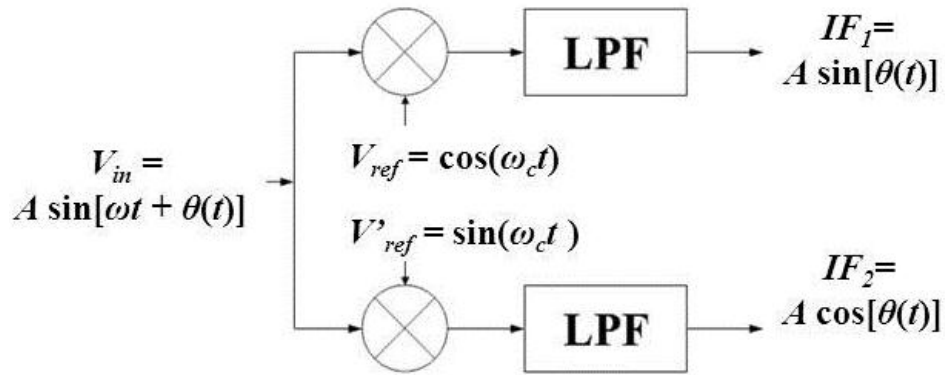


Figure 5-1. Conventional quadrature receiver model.

In this figure,

$$\begin{aligned}
 V_{in} &= A \cdot \sin(\omega_c t + \theta(t)) \\
 V_{ref} &= 2 \cdot \cos(\omega_c t) \\
 V'_{ref} &= 2 \cdot \sin(\omega_c t)
 \end{aligned}
 \tag{5.1}$$

Where A is the amplitude or envelope, ω_c is the center frequency, and $\theta(t)$ is the phase of the incoming signal.

To achieve phase detection, V_{in} is split into two channels. In the top channel, V_{in} is mixed with V_{ref} to produce IF_1 . The high-frequency components of IF_1 are attenuated by a low pass filter LPF₁. The output of LPF₁ is called the I or in-phase channel. In the lower channel, V_{in} is mixed with V'_{ref} to produce IF_2 . Following, LPF₂ filters the high-frequency components of IF_2 . This output is called the Q or quadrature channel. V_{in} can now be represented in complex form:

$$V_{in}(t) = I(t) + j \cdot Q(t) = e^{j\theta(t)} \quad (5.2)$$

where

$$\theta(t) = \arctan\left(\frac{Q(t)}{I(t)}\right) \quad (5.3)$$

Despite the advantages highlighted before, multiple challenges need to be addressed. First, there is the need for splitting V_{in} , which results in losing 3 dB of the incoming signal power, and produces errors due to mismatches. The power attenuation is critical in sensing systems that operate close to the noise level. Second, the imperfections present in analog hardware create additional amplitude mismatches between LPF_1 and LPF_2 , and phase mismatches between V_{ref} and V'_{ref} . Third, the dc signal output is prone to offsets and is most susceptible to $1/f$ noise.

Digital methods found in the literature [20-25] help deal with most of these effects, but are limited by their bandwidth. These methods rely on sampling at a frequency that is an exact multiple of the sampled frequency. They have the advantage of simplicity and accuracy, but are of limited use in applications where ω_c varies greatly, since they show a resolution of 0.5° for a bandwidth of 0.2% of the sampling frequency [22]. Frequency drifts of 0.2%, and larger, are common when sampling signals produced by down-converted millimeter wave sources.

5.2. Proposed method

Our technique addresses these problems by employing an analog stage for down-conversion followed by a digital demodulation. In the first section, the signal is down converted to a frequency band that is possible to sample with current off-the-shelf components. Besides the signal of interest, a reference is down-converted using the same approach. Once these two signals are sampled, phase detection is achieved using one or more of several methods. These studies were developed for the active imaging system described in chapter 4, having quasi-monochromatic radiation. In this work, two approaches are presented.

5.2.1. Phase detection using phase difference of harmonic component

The first method studied subtracts the absolute phases of the reference and the signal of the harmonic with the highest amplitude (away from the DC component). The main advantage from this method comes from measuring high frequency signals (instead of dc), lowering the noise floor at least 30 dB.

Once V_{in} and V_{ref} are sampled, the Fourier transform of each is calculated. If we let $\tilde{V}_{in}(\omega)$ and $\tilde{V}_{ref}(\omega)$ be the Fourier transforms of V_{in} and V_{ref} , respectively, then $\theta(t)$ can be calculated as:

$$\theta(t) = \angle \tilde{V}_{in}(\omega_c) - \angle \tilde{V}_{ref}(\omega_c) \quad (5.4)$$

where \angle represents the phase of the given frequency component. The magnitude A , can be calculated directly from the Fourier transforms.

5.2.2. Phase detection using digital I/Q demodulation

The second studied method emulates analog demodulators using digital equivalents to the needed components. This method is based on the block diagram shown in Figure 5-1. The demodulation process is performed offline after the reference and the signals are sampled and stored. This method is more robust than the previous one, showing less sensitivity to noise, harmonic content or frequency instability, but comes at the expense of higher processing requirements. The main reason driving the need for use of this digital equivalent of analog I/Q demodulators is the elimination of amplitude and phase mismatches. Other benefits include having the exact same performance of filters, the ability to use zero-phase filters, and the measurement performed away from the dc component. Measurements performed at higher frequencies increase the SNR more than 30 dB, by reducing the effect of $1/f$ noise.

The physical components of Figure 5-1 can be substituted by digital equivalents and the power dividers do not need to be translated as the same input signal is used for both mixers. Analog mixers are components that perform multiplication and, therefore, are emulated by multiplication of the arrays containing the sampled incoming and reference signals. A 90° phase delayed version of the reference can be obtained using the quadrature property of a Hilbert transform [26]. By definition, the Hilbert transform is given by:

$$q(t) = H\{p(t)\} = \frac{1}{\pi} \int_{-\infty}^{+\infty} \frac{p(t')}{t-t'} dt' \quad (5.5)$$

Where $H\{p(t)\}$ is the Hilbert transform of $p(t)$ and equation (5.5) is equivalent to the convolution of $p(t)$ and $1/\pi t$. Using the convolution theorem, $Q(\omega)$, the Fourier transform of $q(t)$ is equal to the product of the Fourier transforms of $p(t)$ and $1/\pi t$:

$$\begin{aligned} Q(\omega) &= -i \operatorname{sign}(\omega) \cdot P(\omega) \\ \Rightarrow q(t) &= \mathbb{F}^{-1}\{-i \operatorname{sign}(\omega) \cdot P(\omega)\} \end{aligned} \quad (5.6)$$

The negative imaginary unit in the frequency domain, in equation (5.6) translates to a -90° phase delay in the time domain. Referring to the notation defined in Figure 5-1, the intermediate frequencies 1 and 2 can be calculated as:

$$\begin{aligned} IF_1 &= V_{in} \times V_{ref} \\ IF_2 &= V_{in} \times V'_{ref} \end{aligned} \quad (5.7)$$

And

$$V'_{ref} = -H\{V_{ref}\} \quad (5.8)$$

LPF₁ and LPF₂ can be simulated using any type of digital low pass filter that only lets through the DC component. For these experiments, we found that a second order Butterworth filter with a

cutoff frequency of 0.002 of the sampling frequency produces ripples of less than 1% of the maximum amplitude. Single values of I and Q are calculated by averaging the outputs of LPF₁ and LPF₂.

5.3. Experimental validation

The experimental verification of this processing concept consists of measuring the phase at various points along a plane produced by a reflection of the source on a flat plate. See Figure 5-2. An antenna emits radiation directed toward the flat plate, which acts as a mirror. Reflected radiation is received by another antenna that translates along a straight line on the same plane as the source. Because of differences in traveled paths, the receiver detects a specific phase in each position. Measured and theoretical values are then compared.

For the given configuration, the mirror is located at three different heights and the detector is located at 40 different places, each separated $\frac{1}{4}$ wavelengths from the other. The first detector position, x_1 , is separated 45 mm from the source. The last detector position, x_{40} , is located at $(10 \times 3.2 + 45)$ mm = 77 mm. The detector is mounted on a platform, which is in turn mounted at the end of a linear piston actuator. The distance h has the values 407 ± 1 mm, 427 ± 1 mm, and 445 ± 1 mm. The medium where the signal is propagating is air. The digitizer is set to sample at a rate of 200 MS/sec, collecting 32768 points, with a vertical range of $2 V_{pp}$.

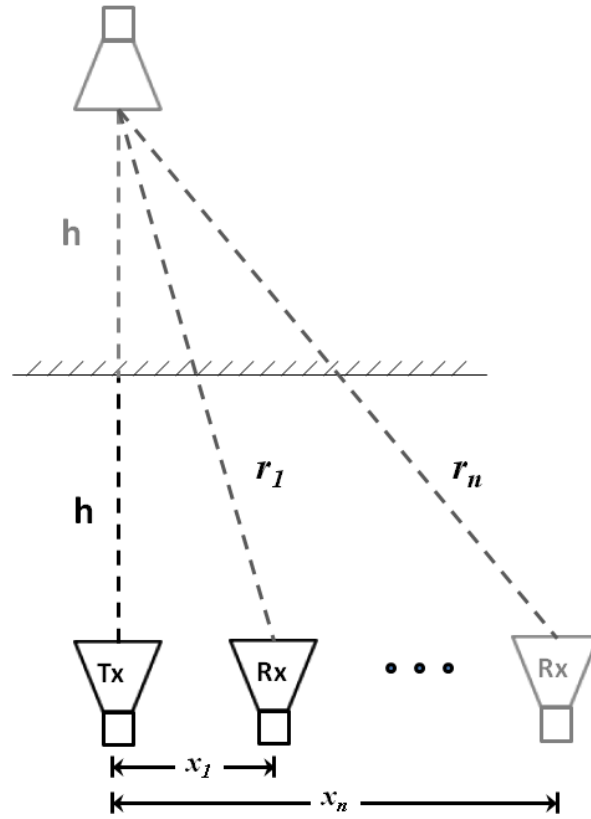


Figure 5-2. Geometry for experimental validation.

5.3.1. Results and comparison with theoretical values

To compute the theoretical values, a simple calculation of the geometric distances is performed. Because of the mirror properties of the flat plate, the setup is analogous to having a source at a distance h from the mirror. The total path is calculated using right triangle relations, as shown in Figure 5-2.

The methods described on sections 5.2.1 and 5.2.2 are applied to the same data set. The results are plotted in the same graph with the expected values. An offset with respect to the calculated value is observed due to minor frequency drifts of the 94 GHz source and minor mechanical

errors. This offset can be calibrated for proper correction during signal processing. Figure 5-3 shows the plots of the relative phase differences at three different heights.

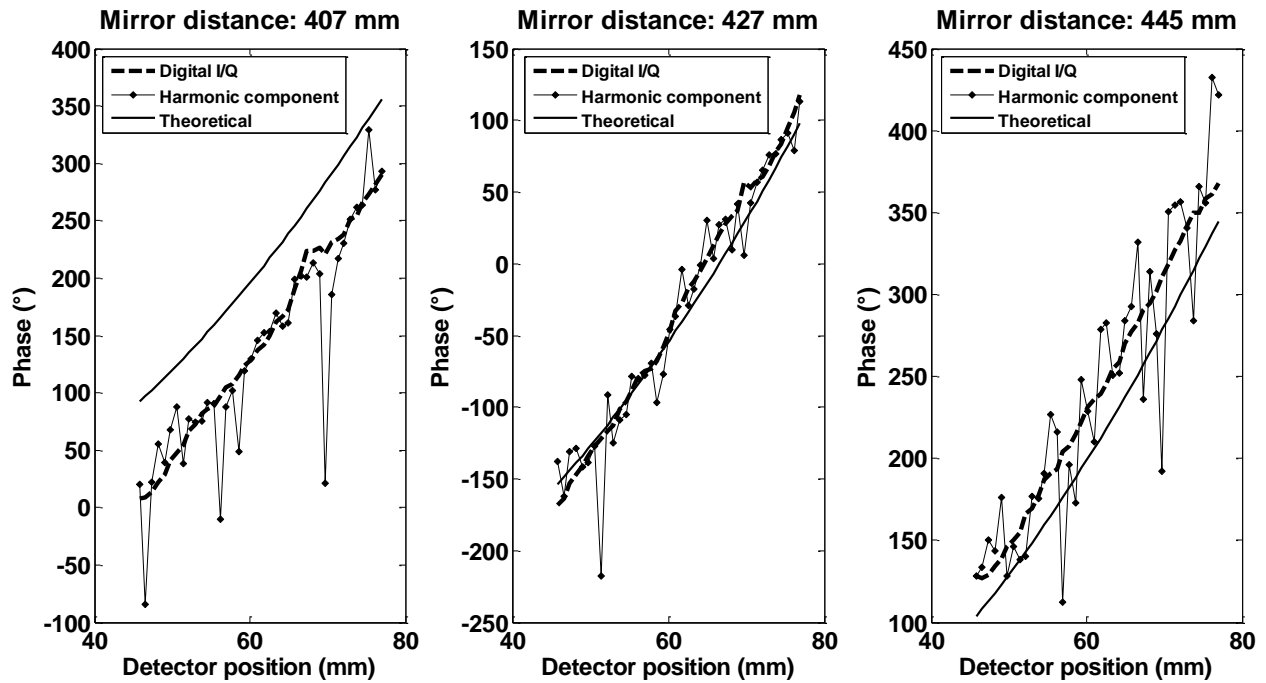


Figure 5-3. Phase difference measurements at three different values of h . The “Harmonic component” and “Digital I/Q” methods are compared to the theoretical values.

CHAPTER 6: IMAGING TESTS

In this chapter, experiments are performed for the validation of the theory explained in chapter three using the test bed described in chapter four. The experiments show the ability of the test bed and the reconstruction algorithms for imaging, using an active sparse-aperture millimeter-wave system with digital correlators. The goal of these experiments is to image targets at distances ranging from 400 – 700 mm from the test bed. A comparison of resolutions obtained using various scanning fillings is also included.

6.1. Experimental Methods

The experiments were performed with the test bed lying horizontally on a table and the targets placed above the test bed. To adjust the distance between the targets and the test bed, targets were mounted on a lift. Three 61 cm \times 61 cm convoluted foam millimeter-wave absorbers, ECCOSORB CV, were placed behind the targets to eliminate unwanted reflections.

6.1.1. Performance metrics

To make a valid comparison of the reconstructions of point sources, the peak-to-integrated-sidelobe-ratio (PISLR) is used. The PISLR is a performance metric equal to the logarithm of the ratio of the energy contained in the center lobe of the point spread function (PSF) and the energy in the sidelobes, given in decibels. The width of the center peak is determined by the Full Width at Half Maximum (FWHM). The PISLR is given by equation (6.1).

$$\text{PISLR} = 10 \log \left[\frac{\int_0^{2\pi} \int_0^{\omega_{FWHM}} \text{PSF}_{array}(\rho, \phi) \rho \cdot d\rho \cdot d\phi}{\int_0^{2\pi} \int_{\omega_{FWHM}}^{\omega_{\max}} \text{PSF}_{array}(\rho, \phi) \rho \cdot d\rho \cdot d\phi} \right] \quad (6.1)$$

In the following measurements, the PISLR is computed numerically from the reconstructed plots. The energy contained by the center peak is computed by integrating the amplitude values that are larger than half the peak (FWHM). The energy in the sidelobes is computed by integrating all remaining amplitude points that belong to a single period in the reconstruction. Equation (6.1) can be adapted for one-dimensional reconstructions by making ϕ a constant.

6.1.2. One-dimensional reconstructions

The first set of experiments is intended to measure the impulse response of the system in one dimension. A ball bearing 15.875 mm in diameter (5/8 inches), illuminated by the source, was the smallest suitable target that could be unambiguously distinguished at a distance between 300 and 900 mm. Reflections coming off the spherical surface of the ball bearing are similar to those produced by a point source. The target was located immediately above the center of the test bed. A 40 element array was simulated by displacing one detector 62.2 mm (19.5 λ). The parameters for digital sampling were chosen based on accuracy and processing speed for these experiments. These parameters are given in Table 6-1.

Table 6-1. Digitizer parameters for reconstruction experiments

Parameter	Value	Units
Sampling rate	200×10^6	Samples per second
Number of samples	32768	NA
Vertical range	200	mV _{pp}
Input Impedance	50	Ω
Vertical coupling	DC	NA

6.1.2.1. Point-sources

The ball bearing was hung 430 ± 10 mm above the center of the test bed and the remaining parameters were as described above. See Figure 6-1 for a setup schematic.

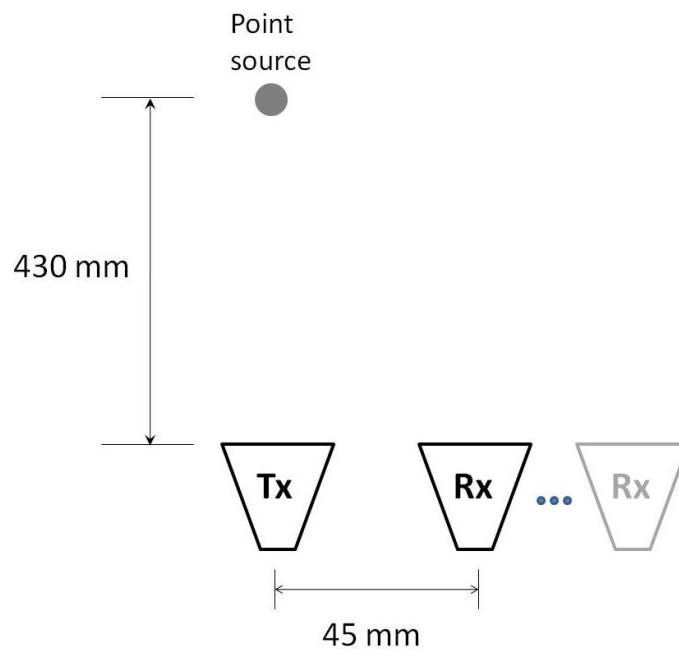


Figure 6-1. Schematic for the experimental setup.

The amplitude and phase of the calculated and measured values is shown in Figure 6-2. The upper plot shows the amplitude of the measured signal at each point. The x-axis is the distance from the center of the test bed. The center was defined as the 0 mm displacement point. The continuous line is the mean of all the amplitudes. For a point source 430 mm from the detector's plane, the calculated amplitude remains almost constant, only varying 2.5% across the measured length.

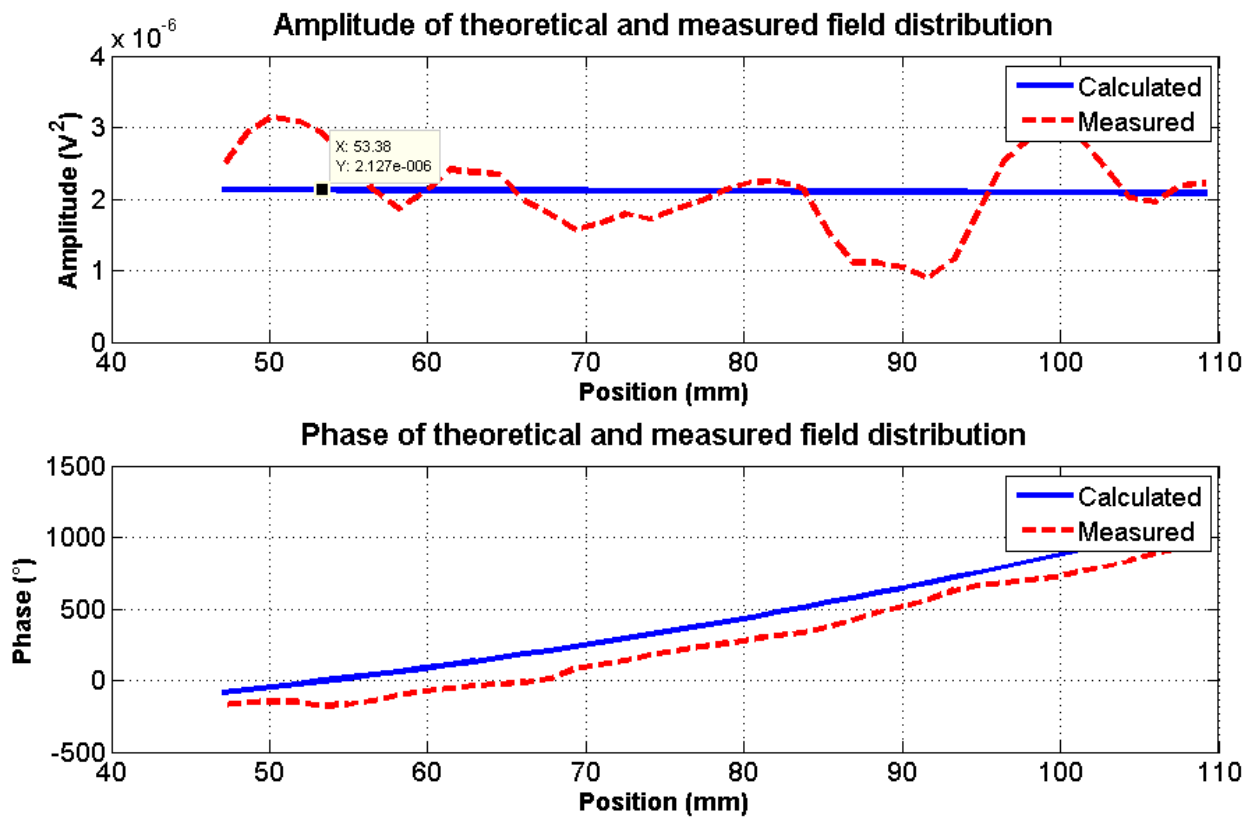


Figure 6-2. Amplitude and phase of theoretical and measured field distributions generated by a point source located 430 mm from the test bed.

The lower graph in Figure 6-2 shows the calculated and measured values of the phase, at the detectors' plane, as a function of the distance from the center. The discrepancy between the absolute values of the calculated and measured values can be disregarded, as only the relative phase difference is of interest. In other words, the relevant information is contained in the slope of the curve and not in the absolute values of every point. For this particular case, the difference between calculated and measured values is approximately 150° , with a standard deviation of 28° . This level of accuracy means that the measured data points are, on average, within $2/25$ of a wavelength of the expected values.

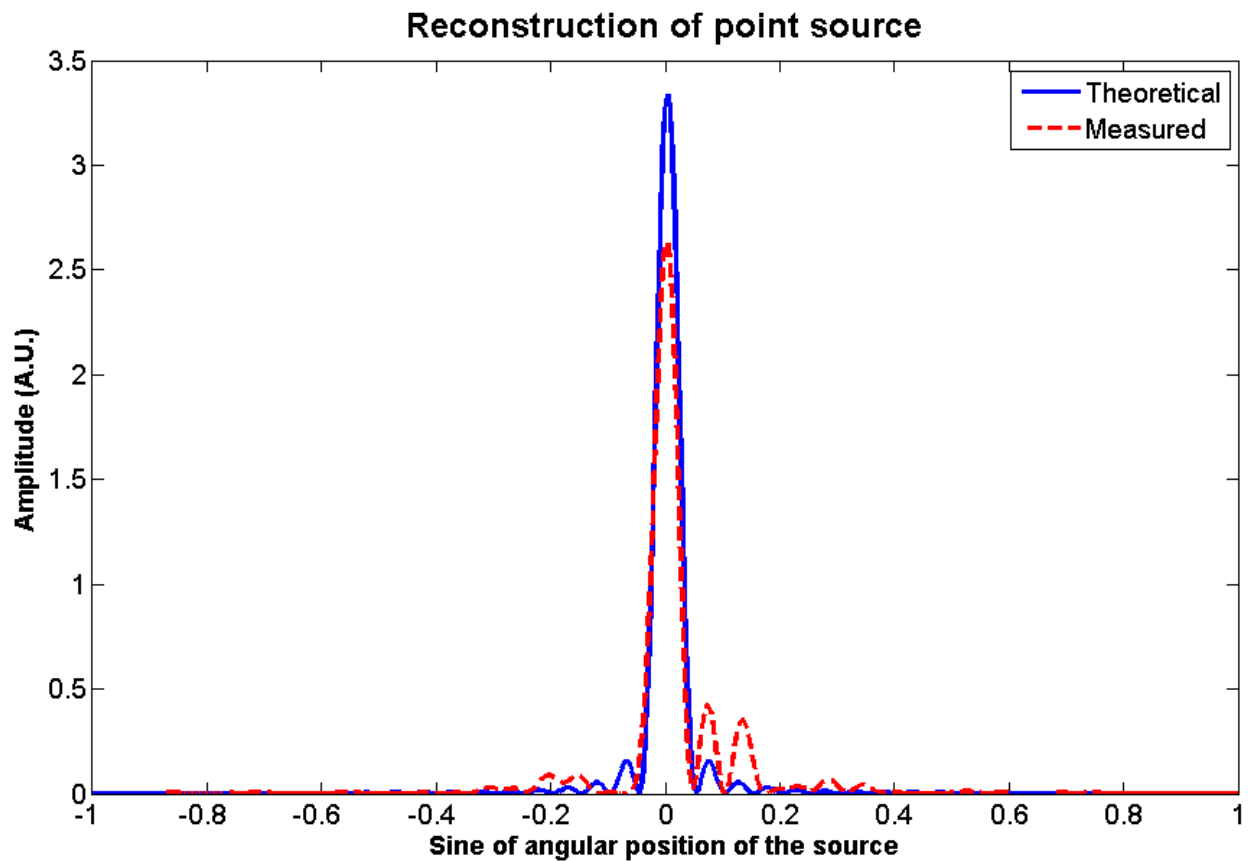


Figure 6-3. Reconstruction of point source using focusing algorithm and signal correlation.

The reconstruction of the measured point source is shown in Figure 6-3. The x-axis is the sine of the angular location of the source, with respect to the assigned reference, and the y-axis is the intensity. For this reconstruction, the data were made to focus at the location of the point source, using the phase correction algorithm described in chapter 3. As a consequence of the use of the focusing algorithm, the image appears centered in the plot. The plot was smoothed by performing an autocorrelation of the signals and by adding a pad of 100 zeros at each end of the array. The FWHM of the measured and calculated values is the same: 2.4° , and the PISLRs are 4.52 dB and 1.6 dB, for the calculated and measured values, respectively.

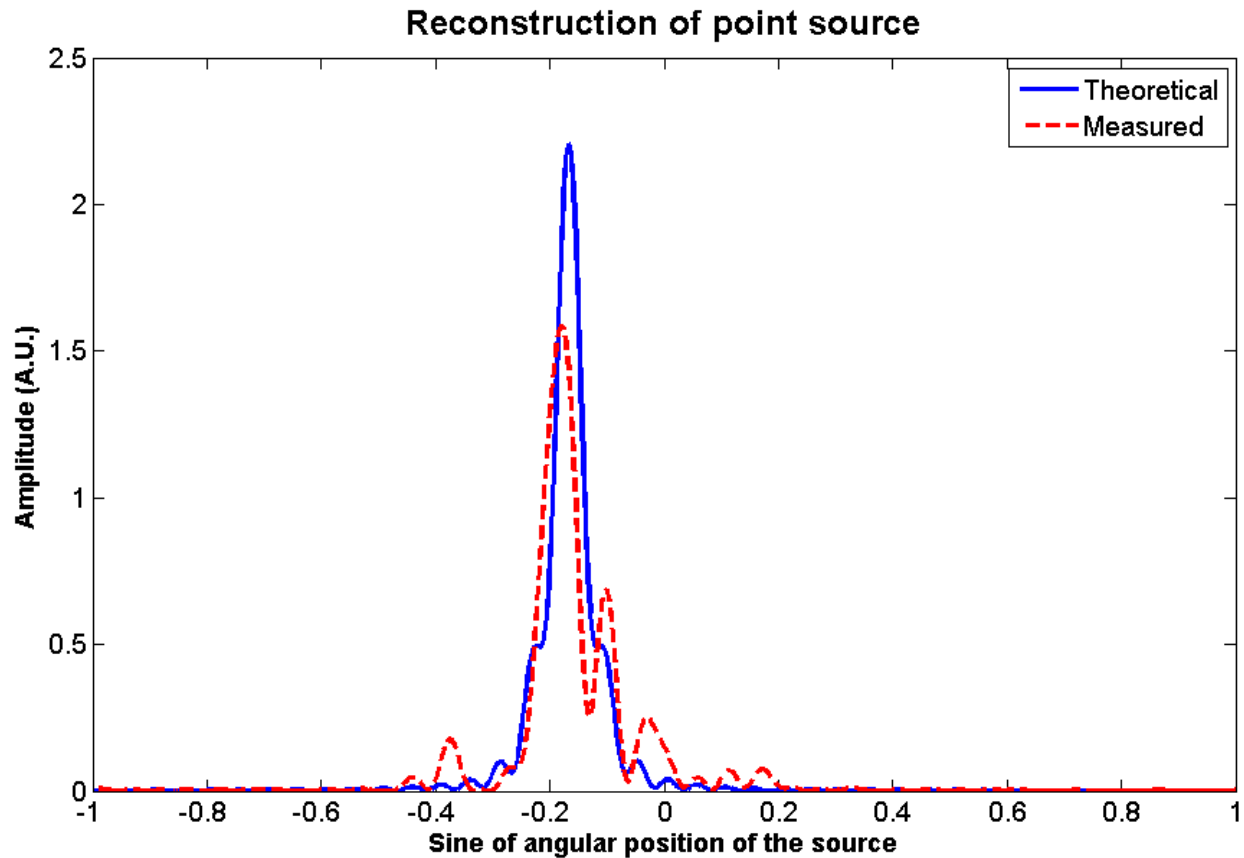


Figure 6-4. Reconstruction of point source without use of focusing algorithm.

Figure 6-4, on the other hand, shows the reconstructed point source without applying the focusing algorithm. Under these circumstances, the location of the object is shifted and the angular location is given with respect to a different reference. The angular reference for Figure 6-4 is taken with respect to the center of the simulated array. The angular reference must not be confused with the zero displacement reference. The calculated and measured values of the angular location of the point source are -9.63° and -10.36° , respectively. The relative large dimension of the simulated array, 62.2 mm, compared to the point source location, 430 mm, means that the effects of near-field reconstruction are going to be noticeable. Without focusing, the FWHMs are 2.67° and 3.4° ; whereas the PISLRs are 0.61 dB and -0.13 dB, for calculated and measured reconstructions, in that order. Also relevant is the loss in intensity for the unfocused reconstruction: it is only 66% and 61% of the focused intensity, for the calculated and measured values, correspondingly.

6.1.2.2. Extended targets

The following set of experiments is intended to apply the above-mentioned techniques to extended targets, namely a metallic ring. Figure 6-5 is a picture of said target sitting on anechoic foam, as seen by the test bed. The dimensions of this target are 126 mm, for the outer diameter, and 84 mm for the inner diameter. The distance from the test bed to the target is 660 mm and the digitizer parameters are as specified in Table 6-1. Two sets of 40 data points were taken, distributed as shown in Figure 6-6. The distance between each data point is 1.6 mm ($1/2 \lambda$) and the separation between each set of 40 points is 105 mm. The void section at the center cannot be sampled due to the test bed design.

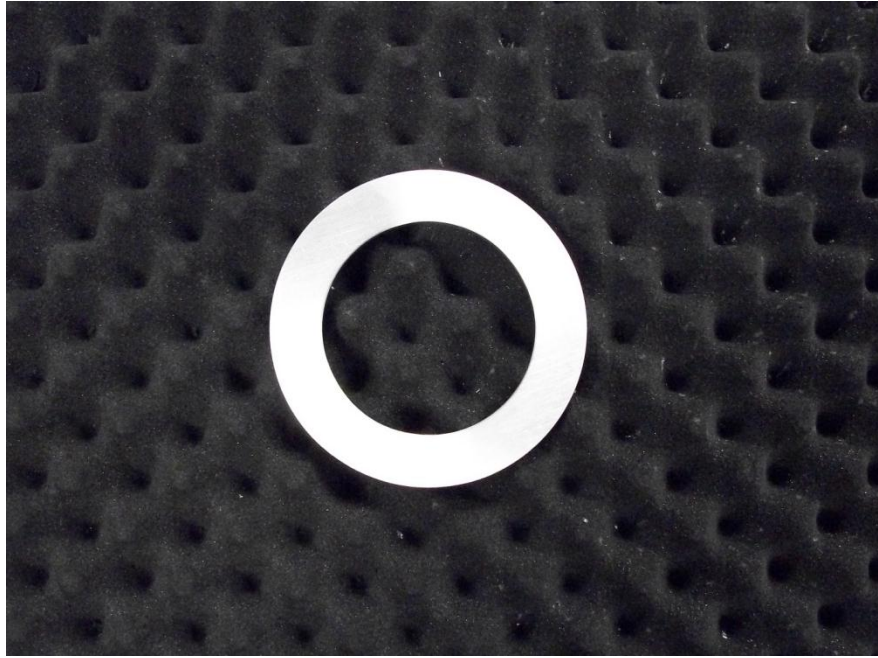


Figure 6-5. Metallic ring used for the extended target reconstructions. Outer diameter: 126 mm, inner diameter: 84 mm.

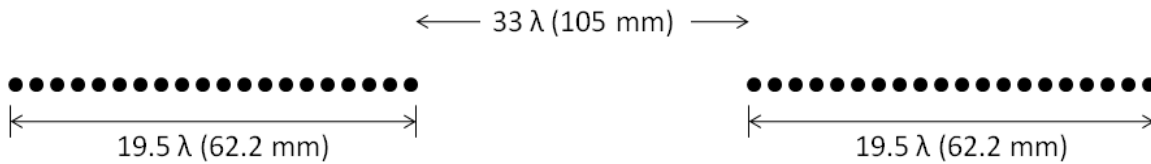


Figure 6-6. Distribution of measured points for the one-dimensional reconstruction of metallic ring target.

The reconstruction process was similar to the one used for the point source measurements. Figure 6-7 shows the one-dimensional slices obtained for arrays along the x-axis (0°) and y-axis (90°). The similar results seen in both plots of Figure 6-7 are a consequence of the symmetry of the target. The angular width of each peak agrees with what is expected to be measured for an

object of the given dimensions: each peak ranges between 1.92° and 2.12° , measured at the FWHM point, and the measured diameter of the target is between 10.8° and 12.6° . The angular dimensions for the target shown in Figure 6-5, at 660 mm, are 1.81° , for the ring width, and 10.9° , for the full diameter.

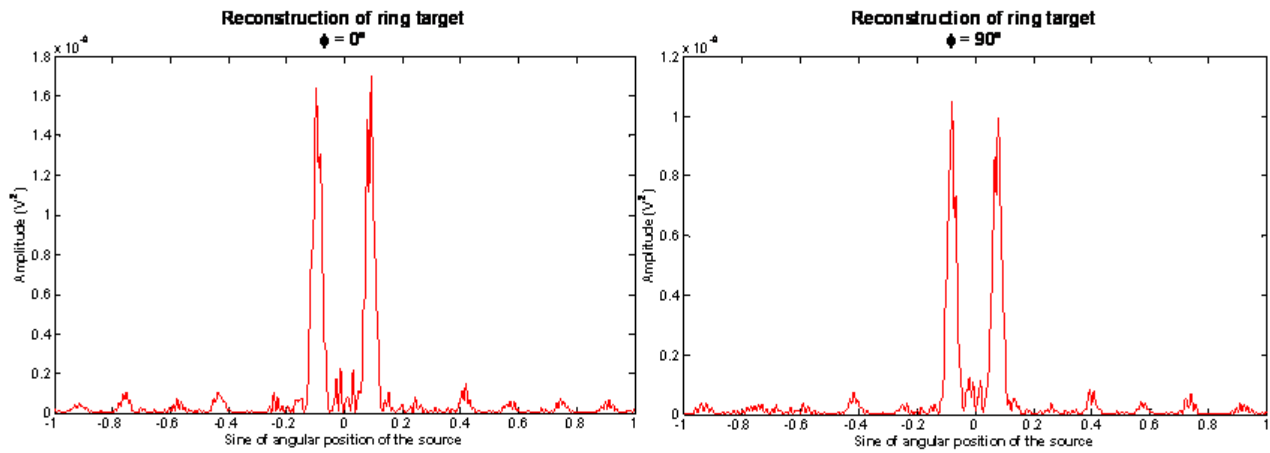


Figure 6-7. Orthogonal one-dimensional reconstructions of ring target.

6.1.3. Two-dimensional reconstructions

Measurements in two dimensions are described in this subsection. The object being imaged is the metallic ring shown in Figure 6-5, at a distance of 660 mm from the test bed. In this set of experiments, a series of one-dimensional scans were performed at different angles and combined into a single two-dimensional array. We studied the progression in image quality as the number of points is increased. The following figures show the distributions used to map the aperture plane on the left, and the two-dimensional reconstructions on the right.

6.1.3.1. Metallic ring reconstruction

Figure 6-8 shows the target reconstruction when using a four-arm configuration. Each arm represents the phase of 40 sampled points with a spacing of $\frac{1}{2} \lambda$. The plot on the right is the reconstruction obtained using the mentioned configuration. The reconstruction shows strong ringing as a consequence of the very low sampling density. Constructive and destructive interference is clearly visible, especially at the intersection of the orthogonal large intensity lines. Detection is possible, but the shape cannot be identified using this configuration.

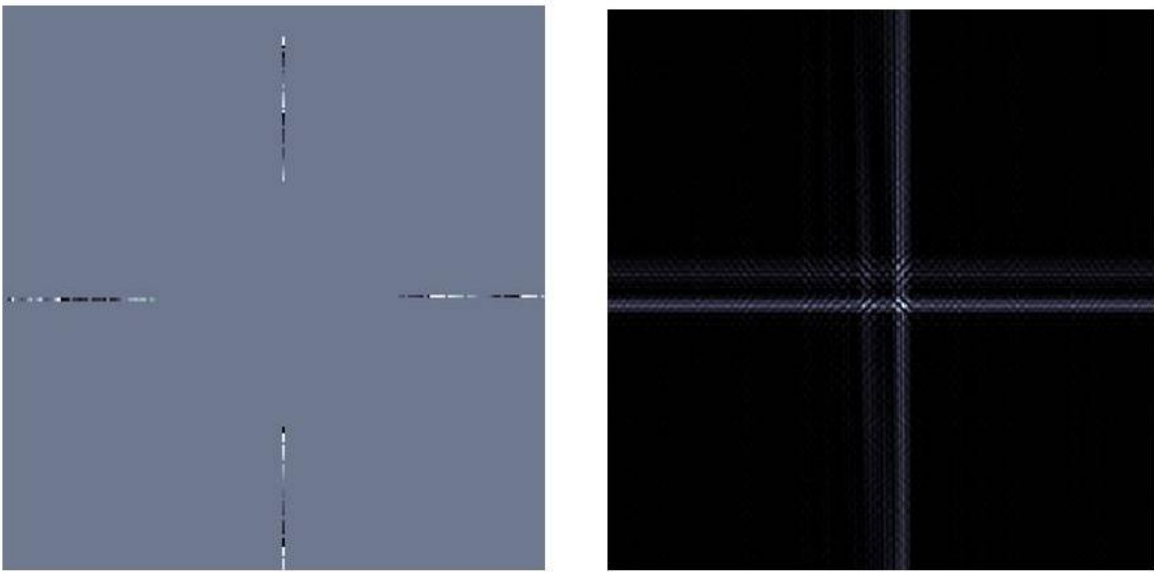


Figure 6-8. Field plot (left) and reconstruction (right) of metallic ring using a 4-arm configuration.

The use of eight arms with an angular separation of 45° generates a field plot and a reconstruction as shown in Figure 6-9. Separation between consecutive points is $\frac{1}{2} \lambda$, with 40 points per arm and a maximum span of 236 mm. We found that increasing the brightness and the

contrast by 20% and 40%, respectively, enhances image quality by making the ringing less noticeable. This sampling configuration still presents strong ringing, but the object can be clearly identified as being circular. The resolution is as expected for the given diameter, about 2° , but ringing is still very strong.

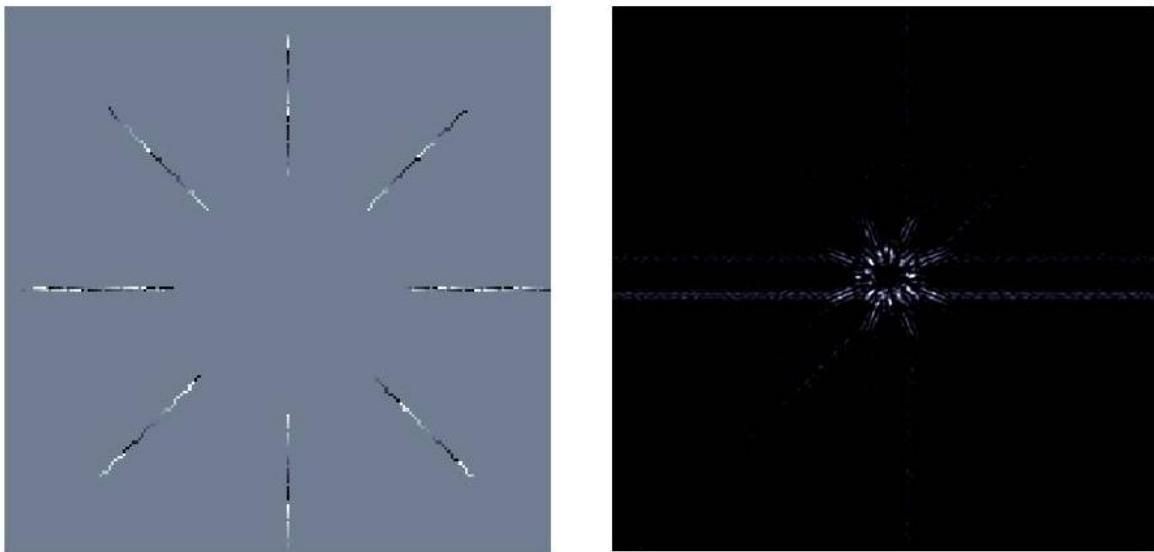


Figure 6-9. Field plot (left) and reconstruction (right) of metallic ring using an 8-arm configuration.

Figure 6-10 and Figure 6-11 are reconstructions obtained using 12- and 24- arm configurations, respectively. These reconstructions show a decrease in ringing as the number of sampled points increase. For the 24-arm configuration, a second parameter was adjusted, namely the spacing between consecutive points, which was increased from $\frac{1}{2} \lambda$ to 1λ . Two effects are visible in Figure 6-11. First, the ringing on the target decreases as a consequence of sampling across more angular values. Second, periodicity becomes notorious because of the larger separation between consecutive points. The reconstructions were enhanced by increasing the brightness 20%, in both

images, and the contrast by 30% and 40, for Figure 6-10 and Figure 6-11, respectively. The chosen zero padding was 200 and 150, in the positive and negative x- and y-directions.

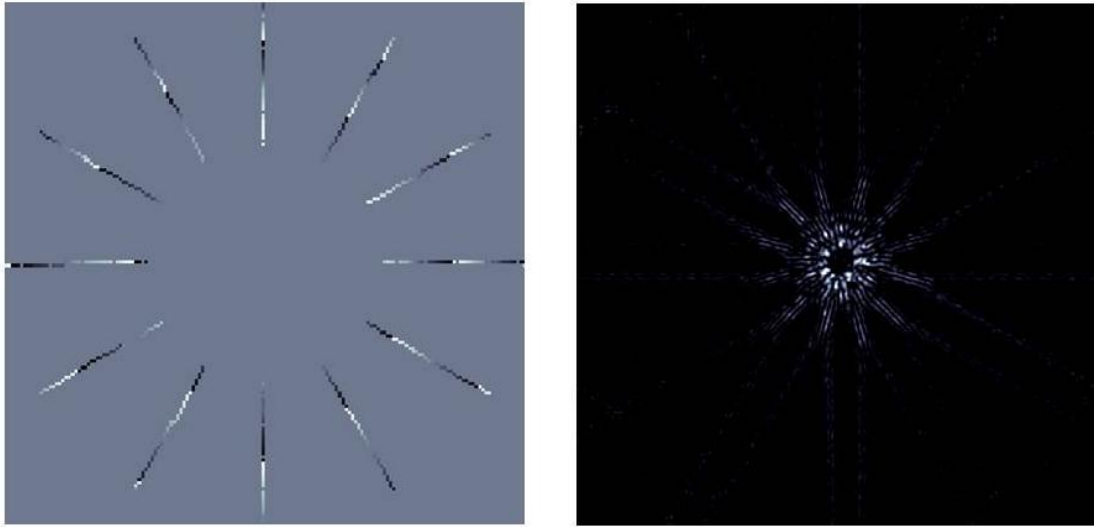


Figure 6-10. Field plot (left) and reconstruction (right) of metallic ring using a 12-arm configuration.

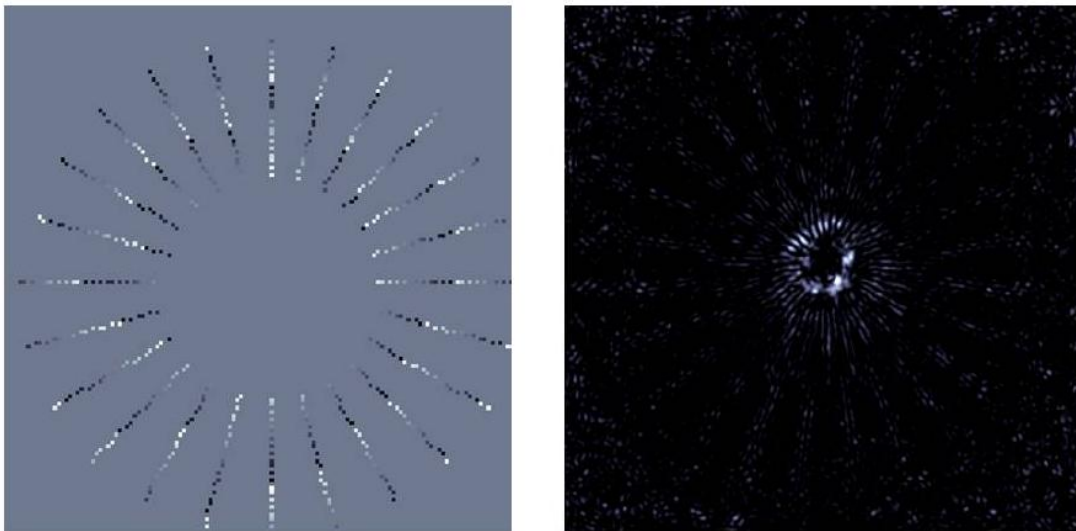


Figure 6-11. Field plot (left) and reconstruction (right) of metallic ring using a 24-arm configuration.

The field scan and the reconstruction of the last set of experiments are shown in Figure 6-12. The field map was obtained making a full scan with constant separation along the x- and y-directions. The separation was chosen to be 2λ . The outer diameter was 260 mm and the inner diameter, the section not sampled, was 105 mm. The more complete sampling of the pupil plane allows distinguishing the concentric circles of constant phase (left plot). The reconstruction does not show the ringing visible in previous figures, as there is no radial symmetry. The image was enhanced by increasing the brightness 35% and the contrast 55%. The Fourier spectrum matrix was padded with 250 zeros in the positive and negative x- and y- directions.

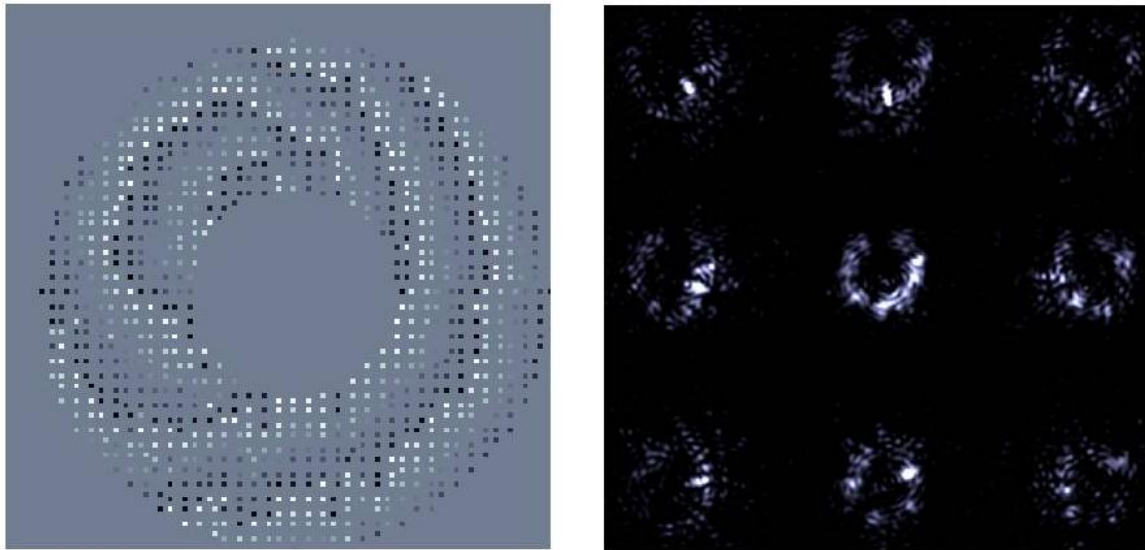


Figure 6-12. Field plot (left) and reconstruction (right) of metallic ring using a full scan.

The periodicity shows up in the form of a square grid, similar to the square grid scanning pattern. The central image presents a clearer focus than the duplicates, and this is a consequence of the phase correction applied to the field measurements.

6.1.3.2. Other targets

In this subsection, we present reconstructions of targets without circular symmetry. We chose a linear plastic element with several small features. The object and its dimensions are shown in Figure 6-13, sitting on anechoic foam, as seen by the test bed. The object was placed 660 mm from the test bed. The digitizer parameters were as given by Table 6-1.

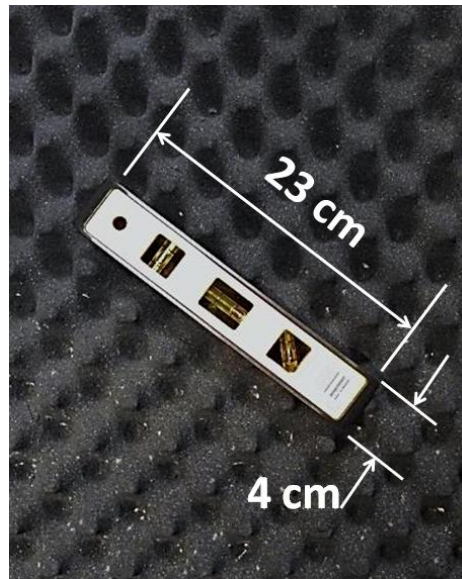


Figure 6-13. Level with plastic casing and its dimensions.

Figure 6-14 shows the field scan and reconstructed images generated in this experiment. The scanning map used was 260 mm in diameter, with an inner void 105 mm in diameter. Points were spaced following a square grid pattern with 2λ separation between points. The angular resolution for this reconstruction is approximately 2° , with minimum resolvable spot being approximately 2 cm, for a distance of 660 mm.

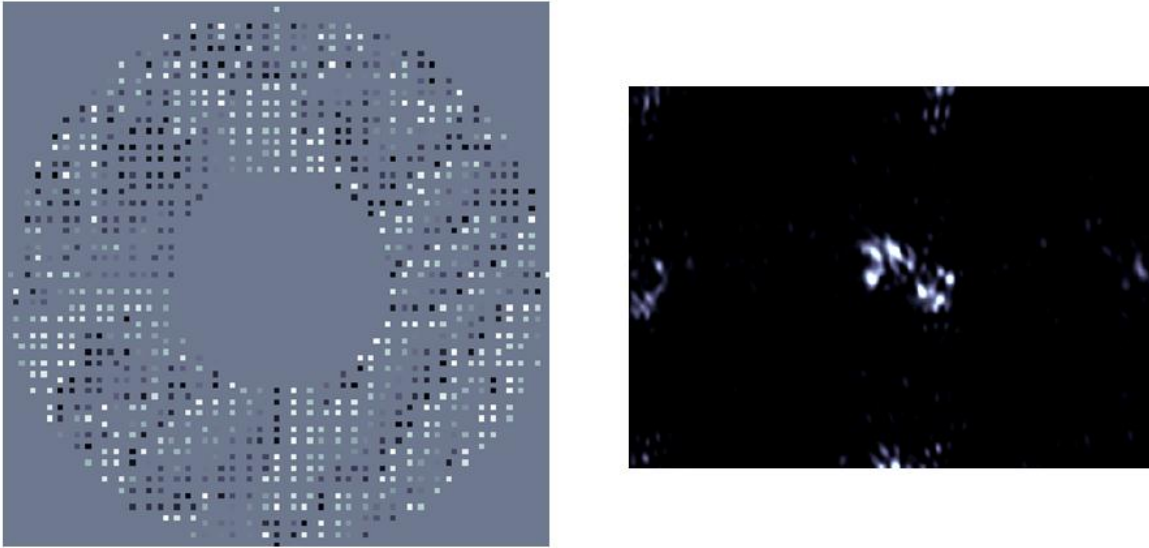


Figure 6-14. Field map (left) and reconstruction (right) using for imaging of targets without circular symmetry. See Figure 6-13.

6.1.3.3. Concealed targets imaging

In this section, we explore the system's ability to image concealed objects. A hand saw placed inside a cardboard envelope, similar to those used for mailing was scanned and imaged. The object was placed 500 mm from the test bed. The maximum separation between scanned points was 100λ (~ 320 mm), and the points were made to fall on a square grid with a separation of 2λ , for a total of 408 points.

The focusing algorithm was applied to the scanned fields. Figure 6-15 shows this algorithm applied to the scanned fields. The focus is moved from 0 mm up to what was considered the clearest image. We found the empirical focus distance to be at 460 mm.

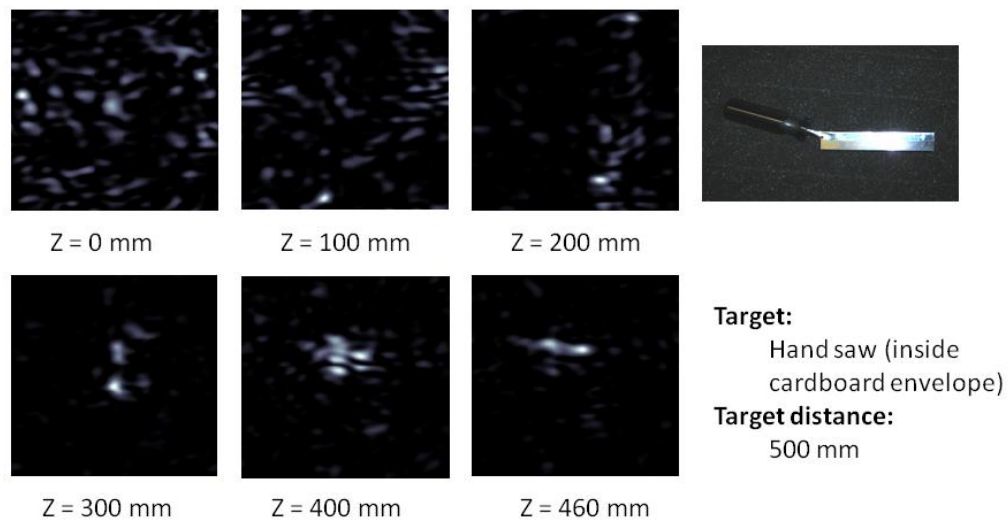


Figure 6-15. Image of a hand saw inside cardboard envelope. Focus between 0 mm and 460 mm.

Figure 6-16 shows the effects of digitally displacing the focus from 460 mm up to 900 mm. The image quality progressively deteriorates as we focus at points located farther away.

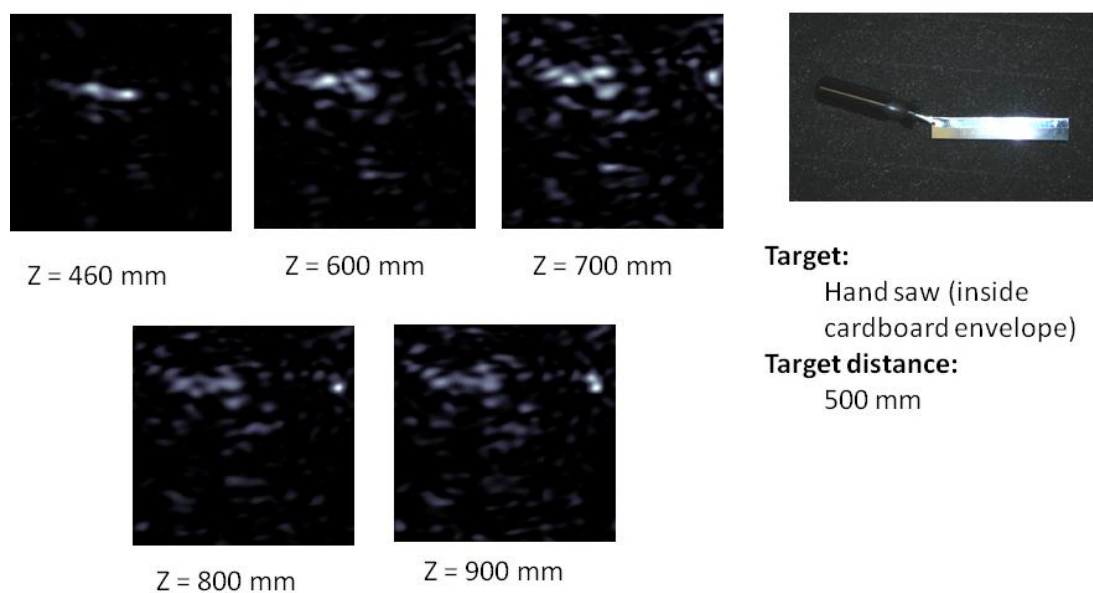


Figure 6-16. Image of a hand saw inside a cardboard envelope. Focus between 460 mm and 900 mm.

6.2. Discussion and conclusions

An active, sparse-aperture millimeter-wave imaging system operating at 94 GHz was tested and assessed. One-dimensional and two-dimensional reconstructions of metallic and non-metallic targets were obtained. The system can resolve targets at distances between 430 mm and 660 mm. The resolution of the reconstructed images is consistent with expected performance. For apertures between 74 and 81 wavelengths, resolution was approximately 2° . This resolution is consistent for plastic and metallic targets.

Sampling patterns have a profound effect on the image quality. The angular resolution is independent of the sampling and depends strongly on the longest baseline, as seen in Figure 6-8 through Figure 6-12. However, large ringing is more visible if not enough points are sampled. Depending on the target, this ringing can deteriorate the picture to a point where reconstructions are not recognizable. Square grid distributions show minimized ringing, as there is not a single direction with higher point concentration. Figure 6-12 has the highest quality in image reconstruction, but still some effects are visible, such as discontinuity in the ring.

The digital focusing algorithm can detect the location of the target in space. Using this algorithm is necessary as the aperture sizes, 74 - 81 wavelengths, are of the same order of magnitude as the standoff distance, between 135 and 210 wavelengths.

Finally, and most importantly, we were able to achieve imaging of concealed items. A metallic hand saw hidden inside a cardboard envelope was visible while standing 500 mm away from the

test bed. This ability to image hidden objects using an active and lensless imaging system are, to the best of our knowledge, unique to the system. The approach used for image generation has the potential to be scaled down to smaller, self-contained systems that could be deployed in the field, or used as an aid in high human and cargo traffic situations.

CHAPTER 7: STUDIES ON MINIMALLY REDUNDANT ARRAYS

To sample the largest amount of points of the visibility function, an array must have a correlator for every pair of detectors. The amount of detector pairs of an array grows with the square of the number of detectors [27]. The growth in detector pairs is both an advantage and a disadvantage. The advantage lies in a significant increase of the sampled points of the visibility function, but also implies growth in the number of correlators, thus making the system larger and bulkier. Several approaches have been used to generate imagery using interferometric techniques. These approaches have successfully generated images, but undergo several limitations because of their lack of customization. These limitations are usually imposed on passive systems. The spatial incoherence of passive sources requires that all detectors are measured at the same time. This impossibility of time multiplexing means that virtual arrays cannot be created by displacing the detectors in a single scan. A system with detectors in a circular array is described in [28] and a one-dimensional array with minimum redundancy is described in [29]. A coherent-illumination active imaging system can take advantage of time sliced scans, as described in [30]. However, the latter system requires the target to be displaced in two dimensions to obtain the images. The test bed used for this research provides a configurable array of coherent detectors used to scan backscattered radiation from targets located in the cone of the power pattern of the illuminating source. This test bed can create a virtual array by displacing the detectors instead of the targets. Having the ability of rearranging the receiving array allows direct measurement and comparison of commonly used configurations.

Reconstruction algorithms based on Fourier inversion assume reception of plane waves, that is, the sources are in the far field. Sources closer than the far field can be optically located at infinity by use of a lens, either real or simulated using phase correction, as explained in chapter 3. Sources in the far field imply that the information about the spatial frequency content is not included in the exact location of the detectors, but on the vector separation of the baseline. Therefore, redundant information is collected if two or more pairs of detectors share the same baseline. Configurations with non-redundant autocorrelations were first introduced by Moffet [31], when he presented his study for one-dimensional arrays that could be used for interferometric imaging. Two-dimensional configurations having compact, non-redundant autocorrelations were later presented by Golay [32] and Cornwell [33].

In this chapter, point sources are imaged using known two-dimensional array distributions. These distributions are used to arrange the detectors of the configurable, active, millimeter-wave test bed, operating at 94 GHz and using digital correlators. The performance of a Golay-9 distribution is compared to that of circular, cross, and star configurations.

7.1. Effects of redundancy in the selected configurations

As a consequence of the direct relation between the baseline and the sampled spatial frequency, if two or more apertures share the same baseline along the same direction, then the same point in the (u,v) plane will be sampled. This redundancy of sampled points is not a completely negative situation, as it does not diminish image quality by itself, and multiple sampling of the same point increases the signal-to-noise ratio (SNR) of that particular point. However, minimally-redundant

configurations are preferred as they provide the same image quality of larger arrays with the fewest components.

The spatial frequencies sampled by a sparse or diluted array are directly linked to its shape; therefore, when choosing a configuration, the design needs to consider what frequencies are to be sampled. The baselines are vectorial quantities, meaning that the sampled point in the (u,v) plane depends not only on the absolute separation of the detectors, but also on their orientation.

The modulation transfer function (MTF) of a system is the modulus of the autocorrelation of the sampling array. However, the autocorrelation is not an invertible function and, as such, an array that yields a desired MTF cannot be calculated analytically. Numerical optimizations can be used to calculate the arrays, but are computationally expensive [34].

Two-dimensional arrays having compact, non-redundant autocorrelations were introduced by Golay in 1971 [32]. Golay arrived at these configurations using algorithms based on random guessing and by limiting those solutions to various grid patterns [34]. These configurations can be applied to arrays that have different fill factors and have been applied to imaging systems having individual apertures of varying sizes [35]. Cornwell developed algorithms with non-redundant autocorrelations, but his arrays had the limitation that the detectors need to lay on a circle. In this study, out of all the available non-redundant configurations, the Golay-9 array was preferred for its compactness and homogeneous distribution of its autocorrelation.

7.2. Spatial frequency distribution of known array configurations

Four array configurations were selected to image a point source. Circular, cross, star, and Golay-9 distributions are used to generate scanning maps all consisting of 9 points. To emulate a nine-element array with a single detector, scans were taken in time multiplex. Figures Figure 7-1 through Figure 7-4 show the chosen detector distributions and their autocorrelations. The column labeled “Auto-correlation amplitude” is the side view of the autocorrelation. The coordinates of the detector distribution maps for the Golay-9, star, circular, and cross arrays are given in Table 7-1 through Table 7-4 and are normalized to fit a square of side equal to 1, expanding from -0.5 to 0.5 in the x and y directions.

Table 7-1. Normalized coordinates for Golay-9 configuration.

Golay-9	(-0.07143,0.04124)	(0.07143,0.04124)	(0,0.08248)
	(0.5,-0.04124)	(0.21428,0.20620)	(-0.21428,0.4536)
	(-0.2857,0.08248)	(-0.2857,-0.4124)	(0.07143,-0.2887)

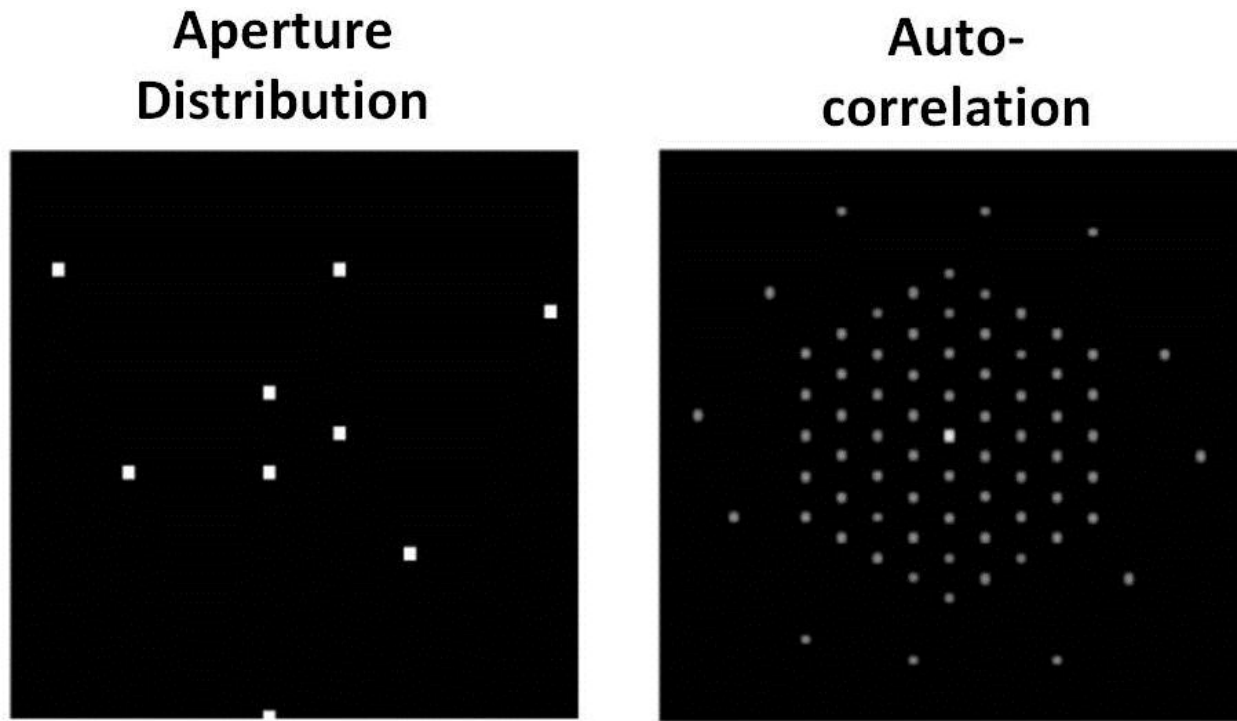


Figure 7-1. Golay-9 distribution and its autocorrelation.

The Golay configuration consists of three sets of points with the points in each set equidistant to the center and it shows a very compact and non-redundant autocorrelation. Only twelve points are not adjacent to the center hexagon. Although the largest number of baselines available for an array with n detectors is equal to $n(n - 1)/2$, twice as many points can be obtained because of the hermitian nature of the (u,v) plane [6]. Therefore, the maximum number of points from a 9-element array is 72, shown in the autocorrelation map of the Golay-9 array.

Table 7-2. Normalized coordinates for star configuration.

	(0,0.4950)	(0.0.3293)	(0,0.1637)
Star	(-0.1417,-0.08184)	(-0.2834,-0.1637)	(-0.4251,-0.2455)
	(0.1417,-0.0818)	(0.2834,-0.1636)	(0.4251,-0.2455)

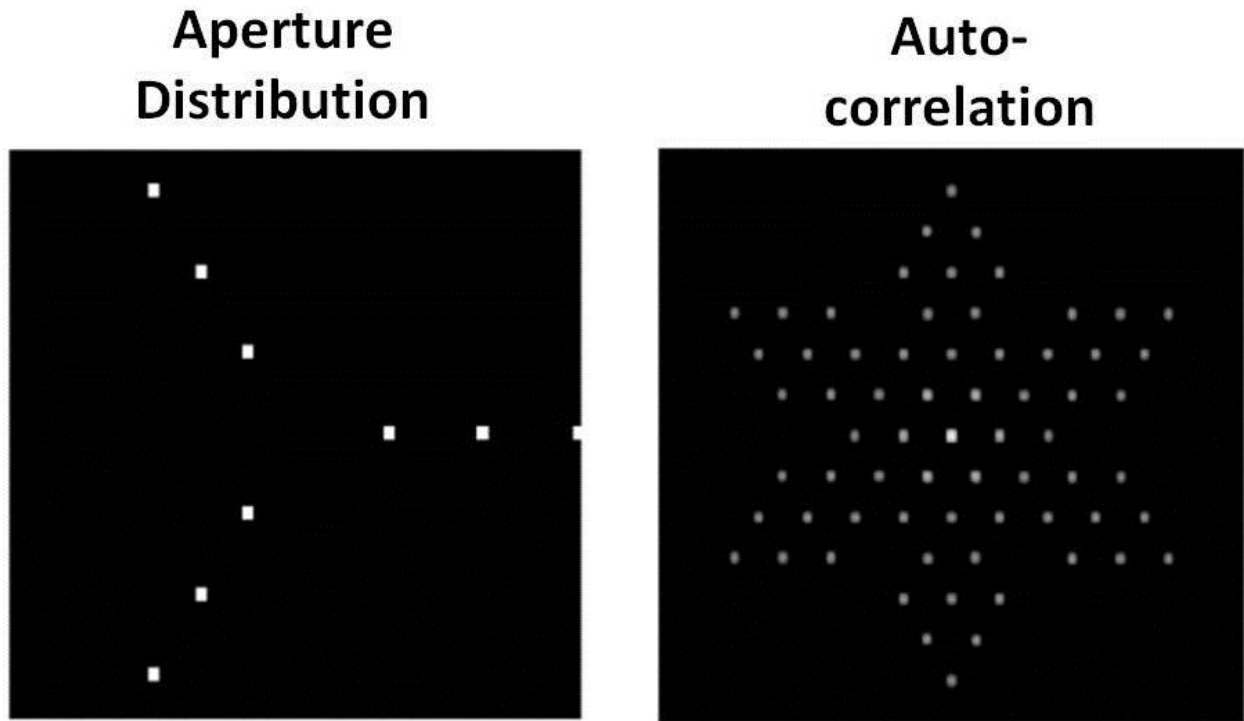


Figure 7-2. Star configuration and its autocorrelation.

The star configuration was selected for its low redundancy, as its autocorrelation is only 6 points smaller than that of the Golay-9. The autocorrelation map is not as compact as the Golay-9, but has the advantage of a simpler design.

Table 7-3. Normalized coordinates for circular configuration.

Circular	(0.5,0)	(0.3830,0.3214)	(0.0868,0.4924)
	(-0.25,0.4330)	(-0.4698,0.1710)	(-0.4698,-0.1710)
	(-0.25,-0.4330)	(0.0868,-0.4924)	(0.3830,-0.3214)

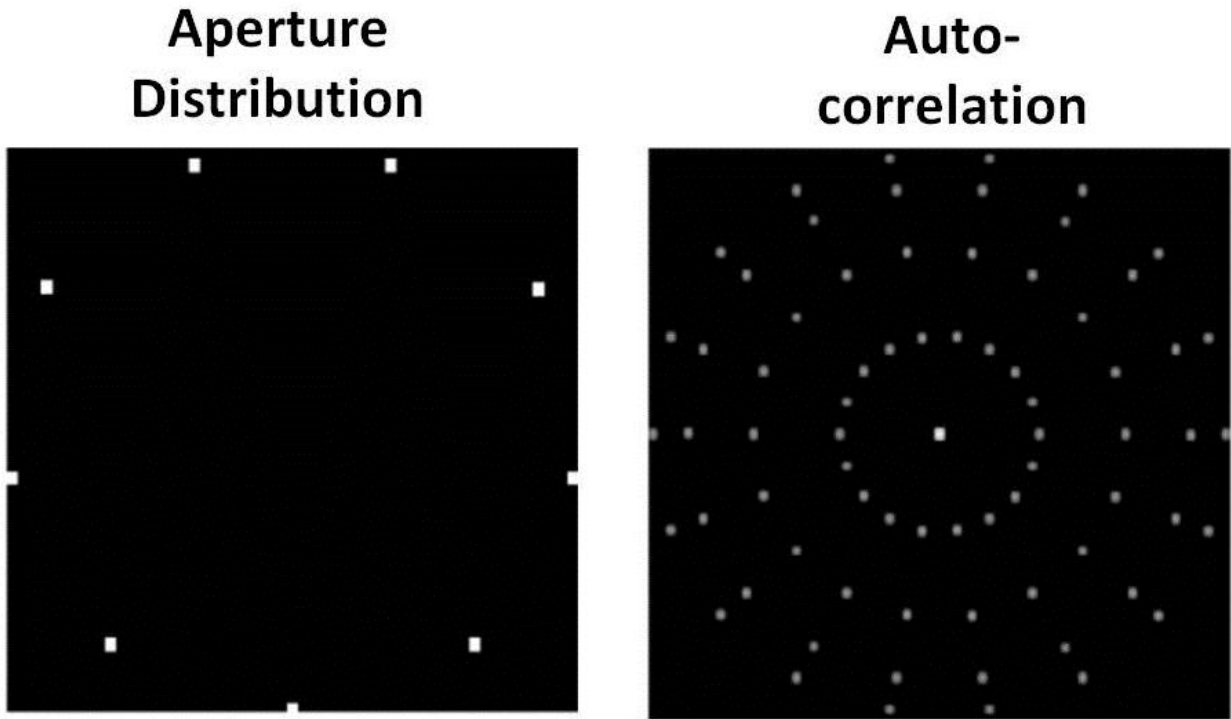


Figure 7-3. Circular configuration and its autocorrelation.

The circular array is another type of non-redundant configuration and with a simple design. However, it lacks the compactness of the Golay distributions. The chosen circular array has constant angular separation among all detectors making it different from the arrangement obtained with Cornwell's algorithm.

Table 7-4. Normalized coordinates of cross configuration.

Cross	$(-0.4880, 0.004)$	$(-0.248, 0.004)$	$(0.004, 0.004)$
	$(0.252, 0.004)$	$(0.492, 0.004)$	$(0.004, -0.4888)$
	$(0.004, -0.248)$	$(0.004, 0.252)$,	$(0.004, 0.492)$

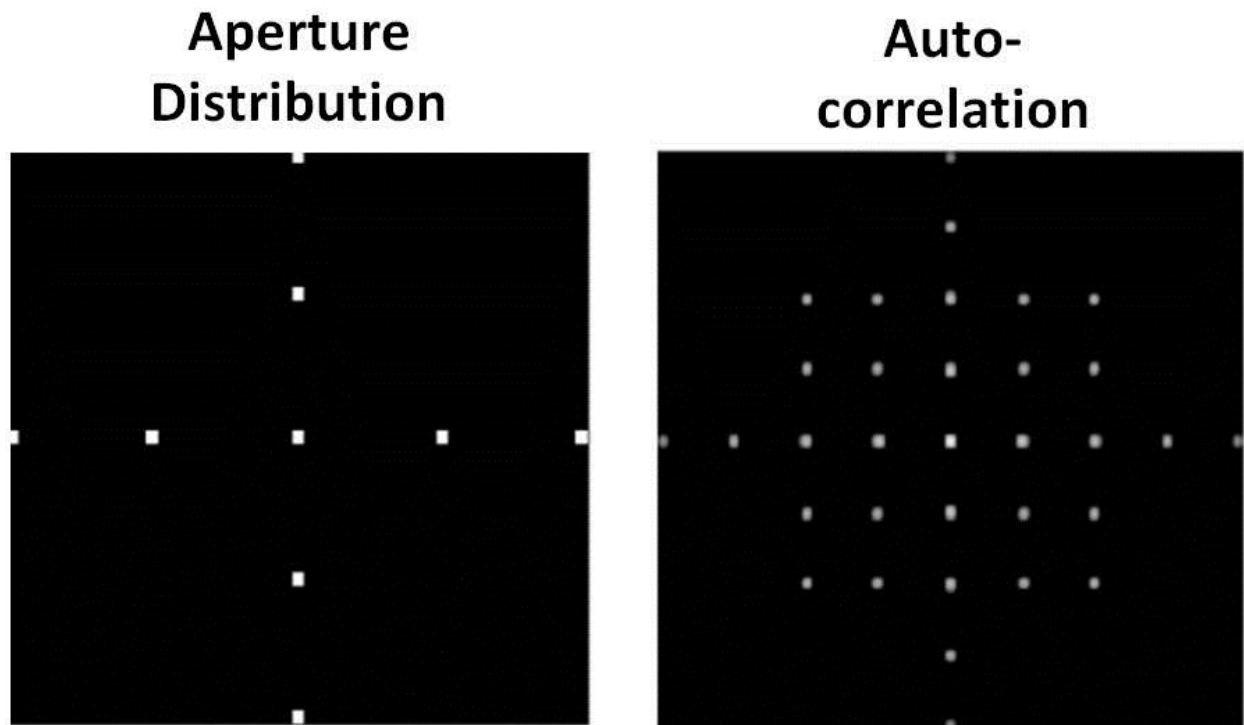


Figure 7-4. Cross configuration and its autocorrelation.

Finally, the last distribution studied is the cross configuration, the most redundant one. It is included for its ubiquity in scanning arrays, and the redundancy is partially compensated by the simplicity of its design. The autocorrelation presents a uniform pattern and the spatial

frequencies are harmonics of the fundamental frequency dictated by the separation of adjacent detectors.

7.3. Simulations and experimental validation

This section describes the experimental setup used to observe the effects of the array distributions in the imaging of a point source using the test bed described in chapter 5. To simulate a point source, a metallic ball bearing having a 15.88 mm (5/8 inches) diameter was located 430 mm immediately above the center of the test bed, where the illuminating antenna is positioned. Because the illuminating source of the test bed is at its center, the detectors cannot sample an inner area 50 mm in diameter. For this reason, the test maps were displaced 50 mm in the positive direction of the x-axis, with respect to the center of the test bed. The physical setup for the measurements was similar to that described in Figure 6-1. The dimensions for the measurements were selected so each array could be circumscribed by a circle 19.4 mm in diameter. This value was selected based on the minimum separation of the Golay-9 array: with this diameter, the minimum separation between the detectors is ½ wavelengths.

The calculated values were obtained by computing the complex fields generated by a spherical point source, with radiation propagating in free space, and measured at the detectors' locations. The propagation of spherical waves in free space is given by:

$$\vec{E}(r) = \frac{1}{|\vec{r}|} \cdot e^{-j\vec{k} \cdot \vec{r}} \quad (6.1)$$

The reconstruction was obtained by performing the Fourier transform of the autocorrelation of the signals. The resulting image obtained with Fourier reconstruction was squared to better help distinguish the main lobe against the side lobes. A focusing algorithm was used to correct the phase and place the source in the far field.

The calculated and measured reconstructions of the point source are plotted next to each other for comparison. The plot following each two-dimensional reconstruction is the normalized cross-section of the slice with the maximum value. This plot is included to compare how close the reconstruction resembles the calculated values. The periodicity observed in the images is a result of subsampling and is a common artifact seen in Fourier inversion reconstructions. Only the largest peak and the first repetition to the left and to the right are plotted. The Fourier reconstructions were smoothed by padding the array with 200 zeros in the positive and negative x and y directions.

Because the gray scale used in the plots does not provide a way to tell subtle differences between the calculated and measured reconstructions, a cross-section plot of the peaks, normalized to the theoretical maximum, is included for more accurate comparison. The performance metrics of the arrays are measured using the PISLR introduced in chapter 6.

7.3.1. Nine-element circular configuration

Figure 7-5 shows the calculated and measured reconstruction of a point source using a 9-element circular array. For this configuration, a narrow center lobe can be obtained, a consequence of

sampling high frequency points. However, many points are still missing from the complete (u,v) plane and, therefore, a large amount of energy is contained in the sidelobes.

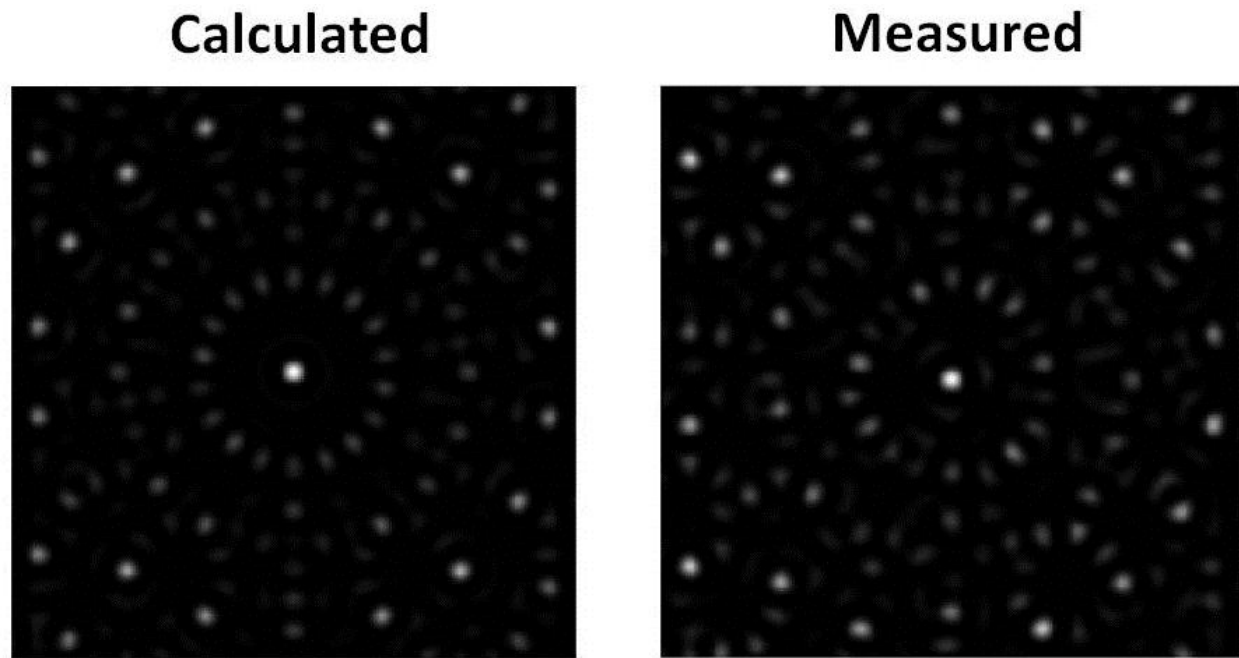


Figure 7-5. Calculated and measured reconstructions of a point source using a 9-element circular configuration.

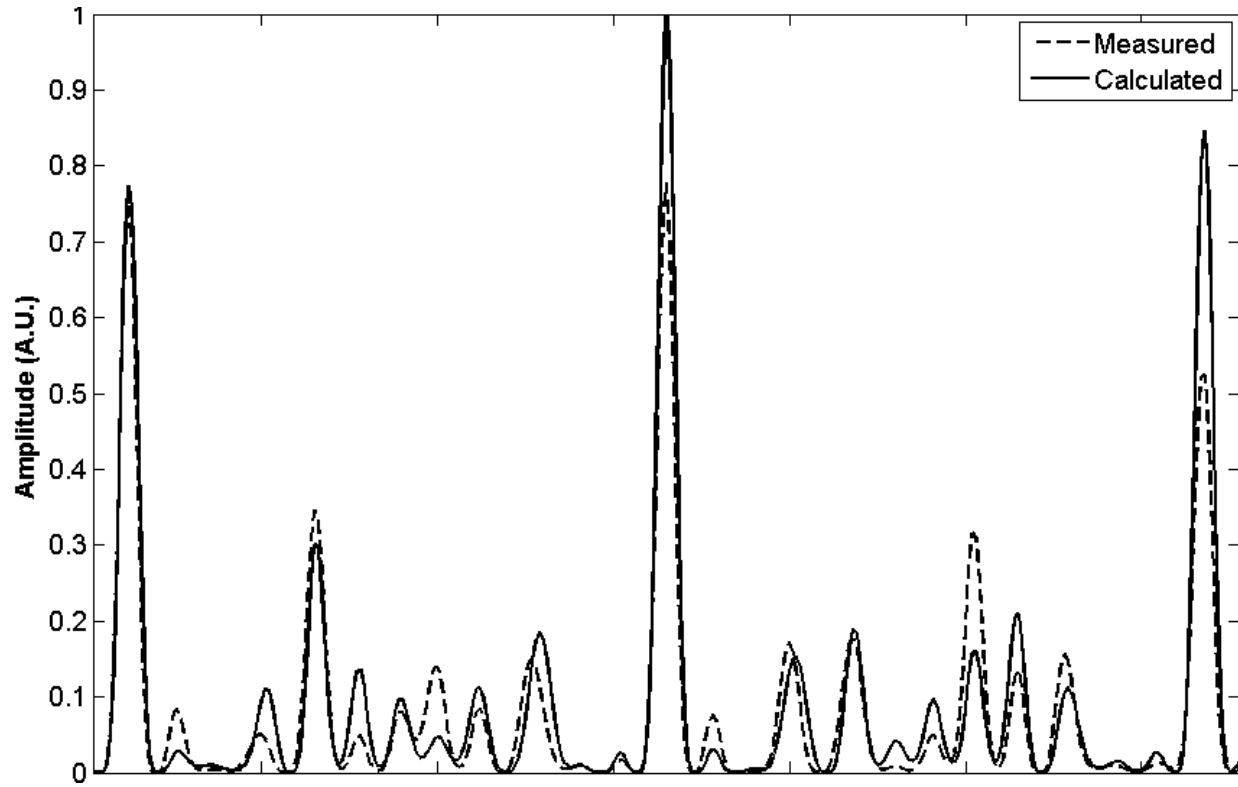


Figure 7-6. Measured and calculated cross-sections of squared amplitude. Reconstruction of a point source using a 9-element circular configuration.

The cross-section of the mainlobes of the reconstructions is plotted in Figure 7-6. This figure shows the calculated and measured values are in good agreement. The ratio of the squared amplitudes of the measured and the calculated values is approximately 0.77, or, what is equivalent, 87.7% of the linear amplitude. The PISLR for the 9-element circular array is -14.8 dB and -16.14 dB for the calculated and measured values, respectively.

7.3.2. Nine-element cross configuration

The calculated and measured reconstructions of a point source, sampled using a 9-element cross configuration, is shown in Figure 7-7. The cross pattern generates a wide center lobe, a product

of the lack of sampling of high frequencies. On the other hand, the compactness of the frequency sampling means that the number of side lobes is small, although they contain a significant amount of the collected energy.

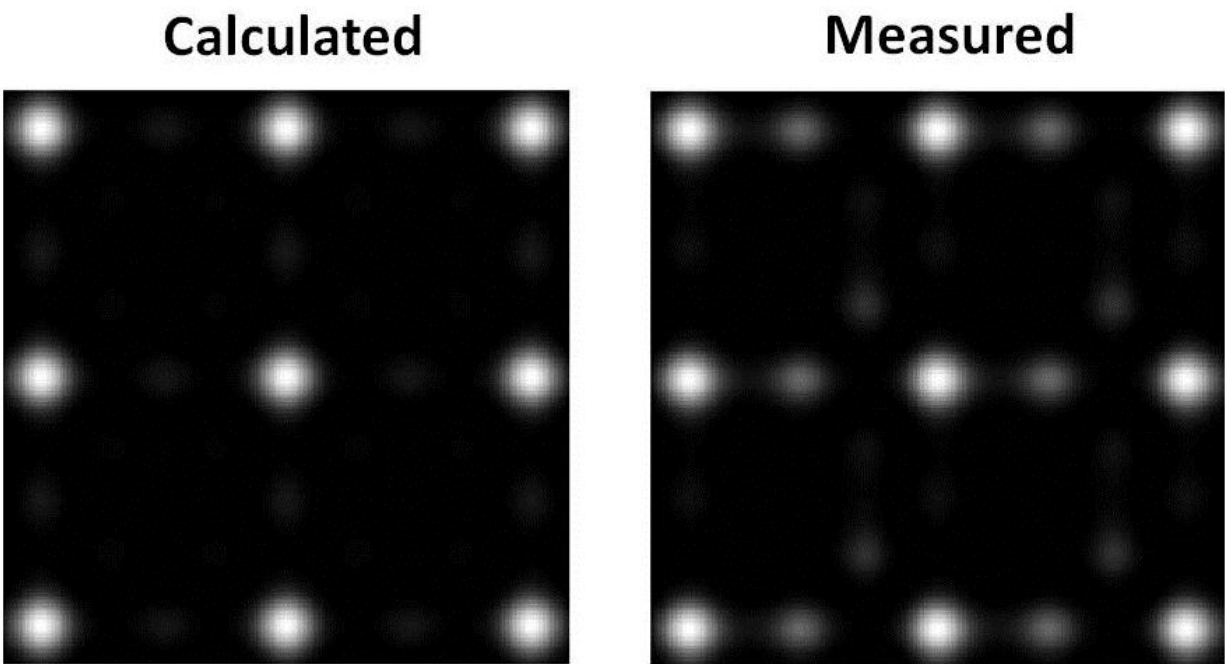


Figure 7-7. Calculated and measured reconstructions of a point source using a 9-element cross configuration.

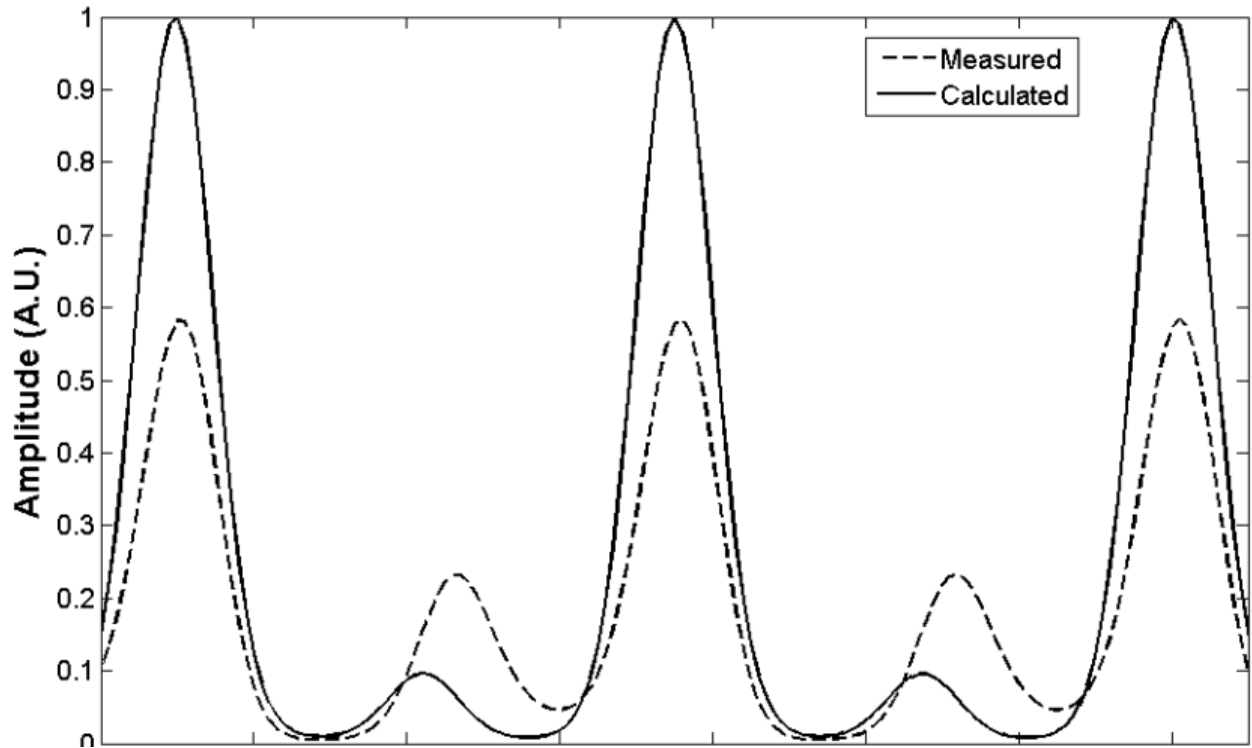


Figure 7-8. Measured and calculated cross-sections of squared amplitude. Reconstruction of a point source using a 9-element cross configuration.

Figure 7-8 is the cross-section plot of the center peaks of the calculated and measured reconstructions shown in Figure 7-7. The ratio of the squared amplitudes of the measured and calculated plots is approximately 0.6, therefore, the linear ratio is approximately 77%. The computed PISLRs are -3.6 dB and -5.7 dB, for the calculated and measured values, respectively.

7.3.3. Golay-9 configuration

Calculated and measured reconstructions of a point source using the Golay-9 configuration are shown in Figure 7-9. The reconstructions obtained using this configuration present a slightly wider center lobe, compared to the circular distribution, but have the advantage of having very small side lobes. Also, the side lobe pattern is irregular, making it easier to distinguish the signal from the noise. The Golay-9 provides the most accurate reconstruction of the four shown in this study.

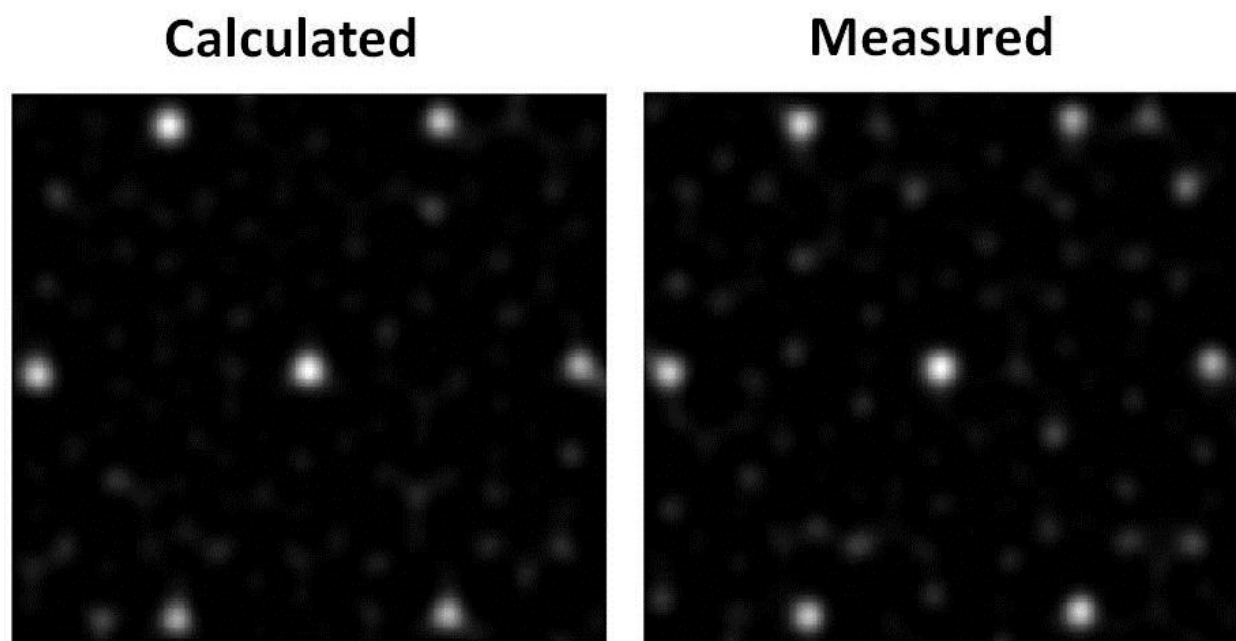


Figure 7-9. Calculated and measured reconstructions of a point source using a Golay-9 configuration.

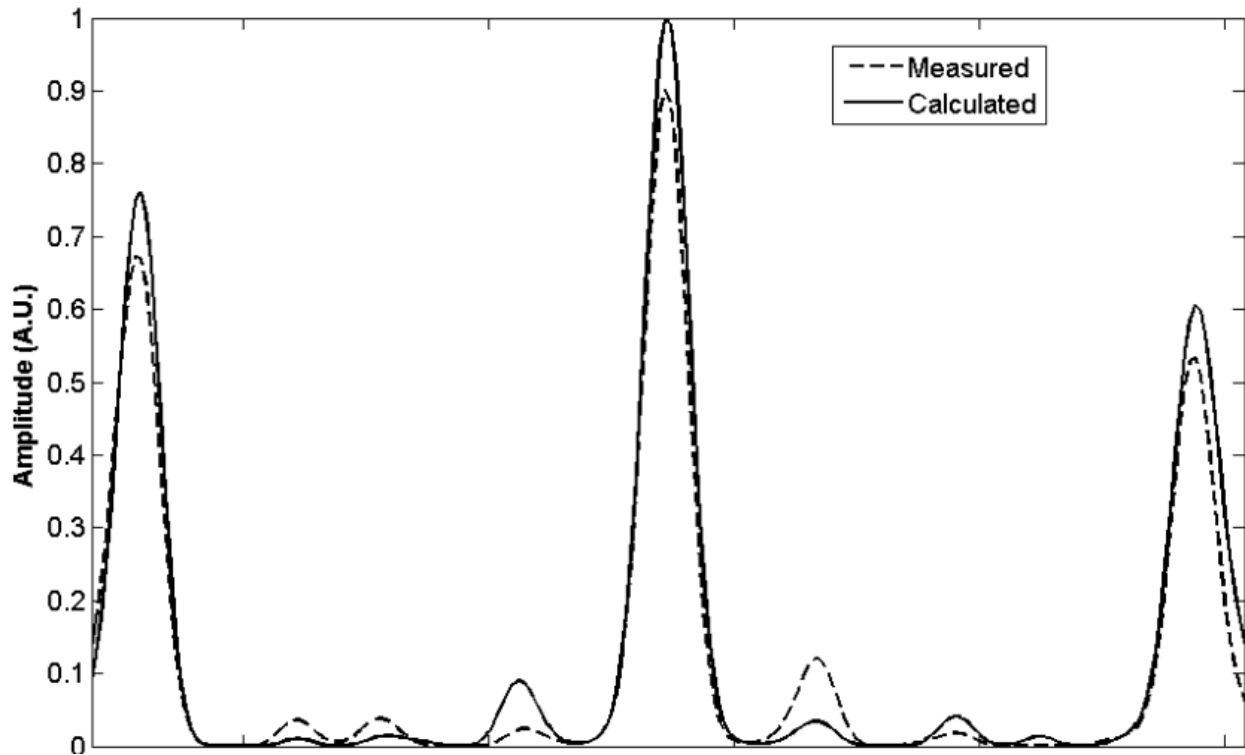


Figure 7-10. Measured and calculated cross-sections of squared amplitude. Reconstruction of a point source using a Golay-9 configuration.

A qualitative analysis of the cross-sections plotted in Figure 7-10 shows the good excellent agreement between the measured and calculated values. The ratio of the squared amplitudes is approximately 0.9, equivalent to 95% of the linear amplitudes. The computed PISLRs are -9.27 dB and -9.46 dB, for the calculated and measured values, respectively.

7.3.4. Nine-element star configuration

The reconstructions obtained using the 9-element star configuration are shown in Figure 7-11. These results are similar to those obtained with the Golay-9 array, but with larger side lobes. Just as the case for the circular configuration, these larger sidelobes are the effect of missing frequency components in the (u,v) plane.

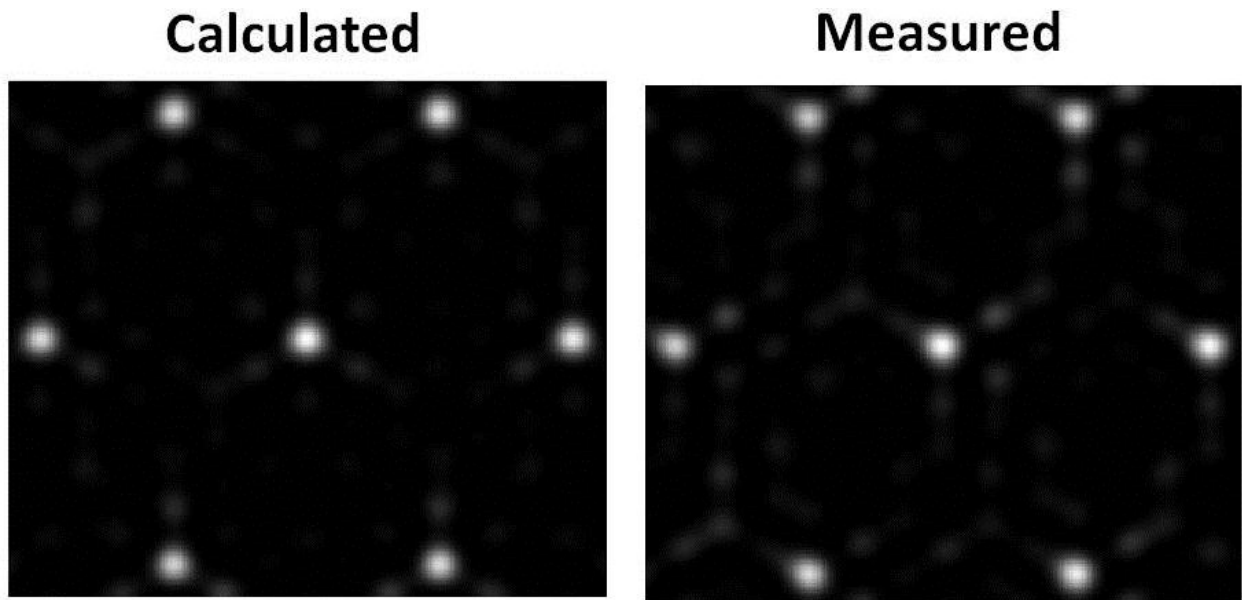


Figure 7-11. Calculated and measured reconstructions of a point source using a 9-element star configuration.

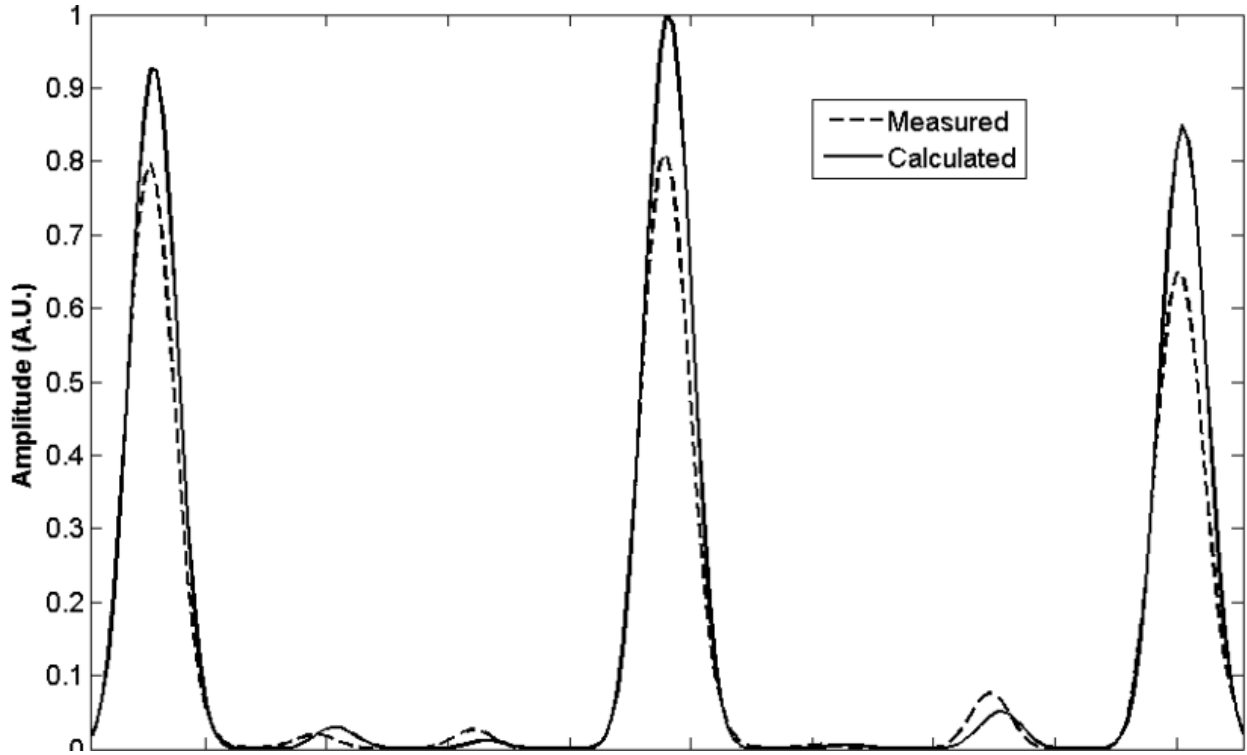


Figure 7-12. Measured and calculated cross-sections of squared amplitude. Reconstruction of a point source using a 9-element star configuration.

The cross-sections of the squared amplitudes of the reconstructions are plotted in Figure 7-12. The ratio of the measured and calculated values is approximately 0.8, or 89% of the linear amplitudes. The computed PISLRs are -8.64 dB and -8.83 dB for the calculated and measured values, respectively.

7.4. Conclusions from the study

Four sampling patterns were studied for aperture sampling, chosen based on their ubiquity. The effects of their distributions in the sampled points of the spatial frequency distribution and in the

resulting image, was analyzed. Each configuration presents advantages and disadvantages that can make them useful in different situations.

A circular array with constant angular separation is excellent for sampling high frequency points. This makes higher resolution images, but may come at the expense of diminished contrast or higher noise levels. One application could be astronomical observations of bright stars or other celestial bodies with very narrow angular width. The cross configuration, despite its low resolution, could still have potential applications where detection is important, but identification is less relevant. The simplicity of its shape makes it useful where the detectors could be mounted on existing structures. This way, monitoring and counting of targets passing through a point could be achieved, just to mention an example.

The Golay configuration is the one showing the highest effectiveness, in terms of concentration of the collected energy in the desired spot. Compactness of the frequency plane makes this arrangement ideal for detection and identification. Also, larger arrays have been designed, with the corresponding increase in frequency sampling. The gain in resolution comes at the expense of a more complicated distribution, as adding elements, while still keeping compactness and non-redundancy, is a complicated task. However, the Golay configurations can be applied to larger apertures, therefore, increasing the resolution without having to create a larger Golay array. One other possibility is using the Golay arrays recurrently: sample small apertures with Golay arrays and then using these apertures to sample a larger one, also distributed as a Golay array. The last arrangement analyzed, the star configuration is simple and effective, having only small side

lobes as a drawback. This configuration could be useful in portable imaging devices intended for detection and identification, where large apertures are needed, but also where a monolithic one would hinder the portability.

CHAPTER 8: CONCLUSIONS AND FUTURE WORK

8.1. Conclusions

The potential applications of millimeter-wave imaging systems have driven the interest in research in this technology. Increasing the resolution of such systems by sampling the pupil plane with sparsely populated detectors is a technique that shows great promise. Reconstruction algorithms similar to those used in passive imagers can also be applied to active imagers. Although results and equations are similar to those obtained for incoherent systems, there are still some differences between them. We highlight two major differences between active and passive systems. Active, coherent imaging has the disadvantage of the presence of speckle in the reconstructions, as seen in Figure 6-8 through Figure 6-11, produced by constructive and destructive interference of monochromatic signals with strong correlation. However, the advantages, in our opinion, outweigh the disadvantages. The possibility of indoor imaging and the ability to sample the signals in time multiplex provide significant benefits. Time multiplex sampling is what makes offline digital processing possible, and all the advantages entailed by it. As shown in chapter 5.

Advances in electronics have made the implementation of digital schemes for millimeter-wave processing possible. We developed, for this research, a novel technique that takes advantage of offline processing to increase the SNR of measured signals. Accurate measurement of magnitude and phase of millimeter-waves can be achieved using this approach.

Later, in chapter 6, we describe experiments used to validate the theory and the built test bed. The system performed as expected, according to the preliminary studies. We show one-dimensional and two-dimensional reconstructions of various targets. Successful imaging of extended targets is solid evidence of the feasibility of using an active, sparse-aperture millimeter-wave imaging system. The ability of imaging objects at distances between 400 and 700 mm, combined with digital correlators and high customizability, make it a unique and useful system for exploration of imaging concepts. In this chapter, we also presented imaging of concealed objects, which prove the potentials of the technology for military and civilian applications.

Finally, in chapter 7, we took advantage of the above-mentioned customizability and performed experiments to compare the performance of several common detector configurations. The four 9-element configurations explored, circular, cross, star, and Golay; show the characteristic impulse response of these arrays. At this point we note that, although the Golay-9 configuration provides the highest accuracy of the four arrays, other configurations may be more suitable for specific situations.

8.2. Future Work

During the length of this research, we found several techniques that could be used to improve the performance of the system. Component simplification, miniaturization and hardware improvements, and software and signal processing are areas where future research can enhance the performance and capabilities of the system.

8.2.1. Component simplification

The down-conversion process could be simplified to a single stage. The main advantage of this step is to eliminate one component altogether, making the system less cluttered. To achieve this goal, we must obtain a stable component that oscillates only a few MHz from the 94 GHz source. We recall that the intermediate frequency needs to be high enough that the effects of $1/f$ noise can be eliminated, but not too high that it requires a high end digitizer to be sampled. Having a high end digitizer is not a disadvantage, but makes the system more expensive. The frequency of the LO need not be specific, but we observed that frequencies 3 MHz and above are good values. If the 3 MHz IF is desired, the source and local oscillator will only be 0.0032% from each other. Obtaining oscillators with center frequencies this close could be challenging and its cost must be weighed before a correct assessment can be made.

Since the replacement of the LO's is expensive, as they are a maximum of six, it could be more cost-effective to substitute the source and the mmW high-power amplifier, instead of the LO's. The new frequency for the source would be lowered to approximately 91.2 GHz. The effect in performance should not vary greatly, as the wavelength would only change less than 3%, and the atmospheric attenuation is not significantly different, as shown in Figure 1-1.

8.2.2. Miniaturization and hardware improvements

The electrical components can be further miniaturized by using monolithic microwave integrated circuits (MMIC). The receiver elements, antenna, amplifier, and mixer can be integrated in a single element reducing the physical dimensions, and noise of the system. Although a quadrature

detector can be implemented in the MMIC, we advise against it, as some of the advantages of digital correlation would be sacrificed. Miniaturization using MMICs represents a significant cost as these components are not available off-the-shelf and must be custom made.

Successful miniaturization of the electrical components would provide a boost to the efforts of obtaining a man-portable system. MMIC's are typically small in size, between 1 mm^2 and 10 mm^2 , and can be mass produced. All this would make a portable sparse-aperture millimeter-wave imaging system a feasible product.

The general purpose computer can be replaced by an embedded system. A combination of a digital signal processor (DSP) and a microcontroller can provide the motion control as well as the signal processing. The use of custom made programs and electronics saves volume and weight as any unnecessary components or processes typical in a general purpose computer can be eliminated.

8.2.3. Other studies

The high customizability of the system can be used for tests designed for specific targets, that is, determining optimum configurations for objects of a given size, distance, and minimum acceptable resolution. Recurrent minimally redundant configurations can also be performed, as described in section 7.4. Finally, speckle reduction techniques can be applied to minimize the ringing observed in the reconstructed images.

**APPENDIX A:
TEST BED USER'S MANUAL**

This section is dedicated to the specific steps needed to operate the Sparse-Aperture Millimeter-Wave imaging system.

A.1. Motion control and Data Acquisition

1. Turn on computer.
2. Turn on power supplies for devices:
 - a. Rotary stage controller only needs to be plugged into the electrical outlet.
 - b. Turn on power supplies for oscillators, phase reference, channel selector, interface box, and frequency synthesizer.
 - c. Turn on power supply for 94 GHz Gunn diode. First turn on 15 V_{DC} power supply and later regulated 10 V_{DC} power supply.
3. Initialize LabVIEW
4. Connect control cable to frequency synthesizer.
5. Open script named “freq_synth.vi”. Select 2.7 GHz frequency in the front panel.
 - a. Run (to run in LabVIEW just click the arrow pointing to the right in the toolbar).
Once the program has run, the LED labeled “LD” (locked) should turn on.
 - b. It is recommended that the cable be removed before fully operating the test bed, to prevent pulling.
6. Initialize port for communication with rotary stage.
 - a. Open the program named “**CME**” (Copley Motion Explorer).
 - b. Click OK on the dialog box.
 - c. The rotary stage will shake and make three sudden, short movements, meaning communication has been established.

- d. The program can now be closed. Click “No” in the dialog box.
 - e. Note: LabVIEW can communicate with the test bed, but is not capable of initializing the serial port (RS-232). The port must be initialized using the manufacturer’s interface software. Initialization only has to be done once after the computer starts running.
7. Open file named “Motion control and data capture.vi”. Input the requested parameters:
- a. *Save stage position to*: the script saves the position of the rotary stage for each measurement in this text file.
 - b. *Map file*: this is a text file (.txt) that contains the desired positions of the rotary stage and the extension of the arms. It consists of 3 columns: the first one contains the angular displacement of the stage, and the following two columns contain the extension of each arm.
 - c. *Folder name*: folder where the data is going to be stored.
 - d. *Velocity*: translation velocity of the arms. 12000 steps/sec is the default.
 - e. *# of points*: The total number of points is equal to twice this number (one measurement for each arm).

Digitizer inputs:

- f. *Rate*: digitizer sampling rate. Set to 200 MS/sec
- g. *Samples*: number of samples performed by the digitizer in each measurement.
- h. *Channels*: fixed parameter. Do not change. Indicates that both channels in the digitizer are going to be used.

- i. *Vertical range*: Set to 200 mV_{pp}. Do not change this parameter. This is the vertical resolution of the digitizer. It ranges between 200 mV_{pp} to 20 V_{pp}.
- j. *Input impedance*: Input impedance of the digitizer. Set to 50 Ω.
- k. *Vert coupling*: Digitizer coupling. It can be either AC, DC, or ground. If DC coupling is selected, the input impedance must be 50 Ω. If AC coupling is selected, input impedance must be 1 MΩ. Otherwise, program will give an error message.

Monitor outputs:

- 1. *Point # and Actuator*: these are indicators signaling how many measurement points have been completed and what the extension of the arm is in the current measurement point.
8. Run the program. It stops automatically.

A.2. Signal Processing

This section uses the scripts written in MATLAB

- 1. Initialize Matlab
- 2. Select the folder where the data is recorded.
- 3. Open desired script.
- 4. Run desired program.

APPENDIX B: SOFTWARE SCRIPTS

Measurement automation and digital signal processing scripts were written for the test bed. LabVIEW® was used for measurement automation and digital sampling. Signal processing was handled using MATLAB scripts. For the proper functioning of the scripts certain add-ons for LabVIEW and MATLAB must also be installed.

B.1. LabVIEW scripts

1. “Motion control and data capture.vi”: this is the main program. It controls the motion of the rotary stage and linear actuators, captures data using the digitizer, and saves the data to disk. This script calls a separate MATLAB window for proper functioning.
2. “Freq_synth.vi”: Sets the frequency of the frequency synthesizer.
3. “Move simultaneously.vi”: moves the linear actuators simultaneously to the specified position. It requires the motion controller card to be initialized. If it’s not initialized, it will send an error message.
4. “rev_lim.vi”: Initializes the motion control cards and zeroes the selected linear actuator.
5. “rotary_stage.vi”: controls the rotary stage. This requires the communication port to be initialized by running the “Copley Motion Explorer” program. See step 6 of the [motion control and data acquisition](#) section.
6. “Switch.vi”: activates and deactivates the desired channel in the channel selector.
7. “Phase detection - digital mixing2.vi”: plots the signal and the power spectrum continuously. It also shows the amplitude of the signal and the phase relative to the reference.

Needed Add-ons (LabVIEW):

These scripts require the “NI Motion” and “Motion Assistant” add-ons for linear actuator control, as well as the “Signal Express” add-on for digitizer control.

MATLAB Scripts

Main scripts:

1. “SAID_reconst_010.m”: this script takes the raw data from the measurements and translates the coordinates given in rotary stage and linear actuator positions to a two-dimensional matrix. It calls the following sub-scripts:
 - a. “mag_phase.m”: converts the raw data to a complex number equivalent to the magnitude and phase of the detected signal.
 - b. “matrix.m”: converts the rotary stage and linear actuator information to a two-dimensional matrix.
 - c. “phase_front_cor.m”: corrects the phase front from a spherical wave to a plane wave.
2. “one_dimension.m”: plots the theoretical and measured fields for a source located at a distance z from the test bed. It is valid for one-dimensional measurements only.
“One_dimension.m” also calls the “mag_phase.m” subscript described above.

Needed Add-ons (MATLAB):

The following components that are not part of the default installation of MATLAB are needed for proper functioning:

- a) *Signal Processing Toolbox.*

The Signal Processing Toolbox is needed for the correct function of the digital filters and Hilbert transforms.

b) Image Processing Toolbox

The Image Processing Toolbox is needed for analysis of two-dimensional images: filters, histogram equalizations, and other basic image enhancement.

REFERENCES

- [1] F. T. Ulaby, R. K. Moore, and A. K. Fung, *Microwave remote sensing: active and passive*. Reading, Mass.: Addison-Wesley Pub. Co., Advanced Book Program/World Science Division, ARTECH HOUSE, 1981.
- [2] Committee on Assessment of Security Technologies for Transportation, and National Materials Advisory Board, *Assessment of Millimeter-Wave and Terahertz Technology for Detection and Identification of Concealed Explosives and Weapons*. Washington, D.C.: National Academies Press, 2007.
- [3] L. Yujiri, M. Shoucri, and P. Moffa, "Passive millimeter wave imaging," *Microwave Magazine, IEEE*, vol. 4, pp. 39-50, 2003.
- [4] J. M. Lopez-Alonso, J. Alda, and E. Bernabeu, "Principal-component characterization of noise for infrared images," *Applied Optics*, vol. 41, pp. 320-331, Jan 10 2002.
- [5] S. S. Young, *Signal processing and performance analysis for imaging systems*. Boston :: Artech House, 2008.
- [6] M. Peichl, H. Suess, M. Suess, and S. Kern, "Microwave imaging of the brightness temperature distribution of extended areas in the near and far field using two-dimensional aperture synthesis with high spatial resolution," *Radio Science*, vol. 33, pp. 781-801, May-Jun 1998.
- [7] E. Hecht, *Optics*, 4th ed. Reading, Mass.: Addison-Wesley, 2002.

- [8] A. Thompson, J. Moran, and G. Swenson, *Interferometry and Synthesis in Radio Astronomy*: John Wiley & Sons, 2001.
- [9] P. M. Blanchard, A. H. Greenaway, A. R. Harvey, and K. Webster, "Coherent optical beam forming with passive millimeter-wave arrays," *Lightwave Technology, Journal of*, vol. 17, pp. 418-425, 1999.
- [10] C. A. Schuetz, R. D. Martin, I. Biswas, M. S. Mirotznik, S. Shi, G. J. Schneider, J. Murakowski, and D. W. Prather, "Sparse aperture millimeter-wave imaging using optical detection and correlation techniques," 2007, p. 65480B.
- [11] J. MacDonald and J. R. Lockwood, *Alternatives for landmine detection*. Santa Monica, CA: RAND, 2003.
- [12] T. Du Bosq, "Far-infrared/millimeter wave source and component development for imaging and spectroscopy," Orlando, Fla.: University of Central Florida, 2007, pp. xix, 124 p.
- [13] T. W. Du Bosq, J. M. Lopez-Alonso, and G. D. Boreman, "Millimeter wave imaging system for land mine detection," *Applied Optics*, vol. 45, pp. 5686-5692, Aug 1 2006.
- [14] K. M. Yemelyanov, N. Engheta, A. Hoorfar, and J. A. McVay, "Adaptive Polarization Contrast Techniques for Through-Wall Microwave Imaging Applications," *Geoscience and Remote Sensing, IEEE Transactions on*, vol. 47, pp. 1362-1374, 2009.
- [15] G. W. Swenson, Jr. and N. C. Mathur, "The interferometer in radio astronomy," *Proceedings of the IEEE*, vol. 56, pp. 2114-2130, 1968.

- [16] R. MacPhie, "On the mapping by a cross-correlation antenna system of partially coherent radio sources," *Antennas and Propagation, IEEE Transactions on*, vol. 12, pp. 118-124, 1964.
- [17] G. B. Parrent, "Studies in the Theory of Partial Coherence," *Optica Acta: International Journal of Optics*, vol. 6, pp. 285 - 296, 1959.
- [18] C. A. Balanis, *Antenna theory : analysis and design*, 2nd ed. New York: Wiley, 1997.
- [19] J. W. Goodman, *Introduction to Fourier optics*, 3rd ed. Englewood, Colo.: Roberts & Co., 2005.
- [20] C. M. Rader, "A Simple Method for Sampling In-Phase and Quadrature Components," *IEEE Transactions on Aerospace and Electronic Systems*, vol. 48, 1984.
- [21] G. Zhang, D. Al-Khalili, R. J. Inkol, and R. Saper, "A Novel Approach to the Design of I/Q Demodulation Filters," in *IEEE Pacific Rim Conf. on Communications, Computers, and Signal Processing*. vol. 1 Victoria, BC, Canada, 1993, pp. 72 – 76.
- [22] C. Ziomek and P. Corredoura, "Digital I/Q Demodulator," *Proceedings of the 1995 Particle Accelerator Conference*, vol. 4, pp. 2663 - 2665, 1 - 5 May 1995.
- [23] R. Xue, Q. Xu, K. F. Chang, and K. W. Tam, "A New Method of an IF I/Q Demodulator for Narrowband Signals," *IEEE International Symposium on Circuits and Systems*, 23 - 26 May 2005.
- [24] T. S. Rathore and L. S. Mombasawala, "An Accurate Digital Phase Measurement Scheme," *Proc. of the IEEE*, vol. 72, 1984.
- [25] S. M. Mahmud, "High Precision Phase Measurement Using Adaptive Sampling," *IEEE Transactions on Instrumentation and Measurement*, vol. 38, Oct 1989.

- [26] J. M. Blackledge, *Quantitative Coherent Imaging*. San Diego: Academic Press Inc, 1989.
- [27] A. R. Harvey and R. Appleby, "Passive mm-wave imaging from UAVs using aperture synthesis," *The Aeronautical Journal*, vol. 107, 2003.
- [28] Y. Xue, J. Miao, G. Wan, A. Hu, and F. Zhao, "Development of the Disk Antenna Array Aperture Synthesis Millimeter Wave Radiometer," in *Millimeter Waves, 2008. GSMM 2008. Global Symposium on*, 2008, pp. 1-4.
- [29] L. Qingxia, C. Ke, G. Wei, L. Liang, H. Fangmin, and C. Liangbing, "An aperture synthesis radiometer at millimeter wave band," in *Microwave and Millimeter Wave Technology, 2008. ICMMT 2008. International Conference on*, 2008, pp. 1699-1701.
- [30] L. Zhang, Y. Hao, C. G. Parini, and J. Dupuy, "An experimental millimetre wave imaging system," in *Antennas and Propagation Conference, 2008. LAPC 2008. Loughborough*, 2008, pp. 229-232.
- [31] A. Moffet, "Minimum-redundancy linear arrays," *Antennas and Propagation, IEEE Transactions on*, vol. 16, pp. 172-175, 1968.
- [32] M. J. E. Golay, "Point Arrays Having Compact, Nonredundant Autocorrelations," *Journal of the Optical Society of America*, vol. 61, pp. 272-&, 1971.
- [33] T. J. Cornwell, "A novel principle for optimization of the instantaneous Fourier plane coverage of correction arrays," *Antennas and Propagation, IEEE Transactions on*, vol. 36, pp. 1165-1167, 1988.
- [34] N. J. Miller, M. P. Dierking, and B. D. Duncan, "Optical sparse aperture imaging," *Applied Optics*, vol. 46, pp. 5933-5943, Aug 10 2007.

- [35] A. J. Stokes, B. D. Duncan, and M. P. Dierking, "Improving mid-frequency contrast in sparse aperture optical imaging systems based upon the Golay-9 array," *Optics Express*, vol. 18, pp. 4417-4427, Mar 1 2010.